Search for Decaying Neutralinos at HERA
and
Clustering Optimisation for the ZEUS Micro Vertex Detector

Dissertation
zur Erlangung des Doktorgrades
des Departement Physik
der Universität Hamburg

vorgelegt von
Christian Blohm
aus Stade

Hamburg
2009

Gutachterin/Gutachter der Dissertation:	Prof. Dr. P. Schleper Prof. Dr. J. Haller
Gutachterin/Gutachter der Disputation:	Prof. Dr. R. Klanner Prof. Dr. P. Schleper
Datum der Disputation:	3. März 2010
Vorsitzender des Prüfungsausschusses:	Dr. G. Steinbrück
Vorsitzender des Promotionsausschusses:	Prof. Dr. R. Klanner
Dekan der MIN-Fakultät:	Prof. Dr. Heinrich H. Graener

Abstract

A search for gravitinos produced in supersymmetric events in electron proton collisions has been performed with data recorded with the ZEUS detector at HERA in the years 2003 to 2007. In R-parity violating supersymmetric models a neutralino can be produced by t-channel exchange of a selectron between the incoming electron and a quark of the proton. In the Gauge Mediated Supersymmetry Breaking model (GMSB), where the gravitino is the lightest supersymmetric particle, the neutralino in large regions of the parameter space dominantly decays into a gravitino and a photon, leading to events with an isolated high energetic photon and large missing transverse momentum. To separate signal and background, a multi-variate discriminant method was used. No evidence for supersymmetry was found, and limits were derived for the R-parity violating coupling strength and the masses of the selectron and the lightest neutralino.

Moreover, the cluster position reconstruction system of the ZEUS experiment was improved by modifying and implementing an algorithm which uses estimated track angle and impact position from the pattern recognition phase of the tracking system to yield a better position resolution.

Kurzfassung

Eine Suche nach Gravitinos aus supersymmetrischen Ereignissen in Elektron-Proton-Kollisionen wurde mit Daten des ZEUS-Detektors bei HERA aus den Jahren 2003 bis 2007 durchgeführt. In R-Paritäts-verletzenden supersymmetrischen Modellen kann ein Neutralino durch t-Kanal-Austausch eines Selektrons zwischen dem einlaufenden Elektron und einem Quark des Protons erzeugt werden. Im Gauge Mediated Supersymmetry Breaking Model (GMSB), wo das Gravitino das leichteste supersymmetrische Teilchen ist, zerfällt das Neutralino in großen Bereichen des Parameter-Raums dominant in Gravitino und Photon. Dies führt zu Ereignissen mit einem isolierten, hochenergetischen Photon und großem fehlenden Transversalimpuls. Um Signal und Untergrund zu trennen, wurde eine multivariate Diskriminanten-Methode genutzt. Kein Anzeichen von Supersymmetrie wurde gefunden. Es wurden Grenzen für die R-Paritäts-verletzende Kopplungsstärke und die Massen von Selektron und leichtestem Neutralino gesetzt.

Darüber hinaus wurde das Orts-Rekonstruktionssystem des ZEUS-Experiments durch Anpassung und Einsatz eines Algorithmus verbessert, welcher den aus der Mustererkennungsphase abgeschätzten Einfallswinkel und die Eintreff-Position der Spur benutzt, um eine bessere Ortsauflösung zu erhalten.

Contents

Chapter 1

Introduction

In the last centuries science was quite successful in giving answers to questions regarding the fundamental laws and structures of our universe. Today's best answers are provided by the theory of General Relativity, together with the astro-physical model of our universe, and Quantum Field theory in its manifestation as the Standard Model of particle physics.

However, it is clear that these two theories cannot be final. The most striking evidence is the failure to unify them: Quantum Field Theory works only well on a flat space-time, and it seems to be impossible to quantise gravity consistently. Apart from that, there are already within the Standard Model aspects that hint to the existence of a more fundamental theory.

A guiding principle in the search for such a theory is the concept of symmetry. Symmetry was an essential part of many successful ideas in the realm of physics, especially in the last century. The perhaps most prominent examples are Einstein's theory of Relativity (which assumes the invariance under Poincaré transformations, leading to space-time symmetries) and gauge symmetry (the invariance of the Lagrangian under gauge transformations, encoded as Lorentz-invariant generators of a compact Lie group (the gauge group)). Both symmetries can be formalised as Lie algebras, and according to a theorem by Coleman and Mandula [1], the direct product of these algebras is already the most general Lie algebra containing the Poincaré algebra. The irreducible multiplets of this algebra, spanning the representation space of this algebra, therefore have same masses and same spins.

The efforts by Haag, Lopuszanski and Sohnius [2] to find a loop-hole in this no-go theorem led to the development of Supersymmetry (SUSY, [3]). They considered not only Lie-Algebras and thus bosonic symmetries (formulated with the help of commutators $[A, B] = AB - BA$), but also fermionic symmetries (formulated with the help of anti-commutators $\{A, B\} = AB + BA$). The so established general algebra is called the graded Lie-algebra or super-algebra. The extensions of the Poincaré algebra generated by this class are called supersymmetries. For four space-time dimensions and one[1] supersymmetry operator Q SUSY is unique.

Now particles of spin difference 1/2 can sit in one multiplet, transformed into each other by the SUSY operator. This unification of matter (made up of fermions, for which the Pauli exclusion principle prohibits unlimited stacking) and interactions (communicated by bosons with their tendency to collect in coherent states) has many favourable consequences, the most important being the solution to the Hierarchy problem.

[1] For $N > 1$ supersymmetry operators SUSY has to be broken to $N = 1$ in realistic models.

Nevertheless, a quick look into nature tells us that SUSY has to be broken. This breaking destroys the uniqueness of pure SUSY and leads to unambiguities. The general minimal supersymmetric extension of the Standard Model (MSSM) has 124 free parameters. Therefore different scenarios assuming a realistic symmetry breaking model (usually spontaneous breaking in some hidden sector) with substantially less free parameters have been developed. One appealing scenario is the Gauge Mediated SUSY Breaking (GMSB). Parts of the GMSB parameter space allow for certain SUSY processes to be detectable in electron proton scattering at very high energies. For one of them, gravitino production in the presence of R-parity violation, a search was performed, based on previous work by Horn [4] and Nguyen [5].

A search for the GMSB process $ep \to \tilde{\chi}_1^0 X \to \tilde{G}\gamma X$ with the ZEUS detector at the HERA electron proton collider is presented in the first part of this thesis, which is organised as follows: After an introduction to the theoretical framework and the experimental setup the reconstruction of physical quantities from the detector response and the Monte Carlo simulation of the physical processes and the detector response is described. In the following the details of the analysis (event selection, discrimination of signal and background, and limit calculation), are presented.

The second big part of the thesis deals with technical work for the ZEUS tracking group. With the HERA luminosity upgrade in 2000/2001 the Micro Vertex Detector (MVD) [6] was integrated in the ZEUS detector close to the beam pipe. It is a silicon strip detector aimed to improve efficiency, acceptance, and resolution of the tracking system and to tag heavy quarks by identifying displaced vertices. The hit resolution of the MVD is crucial for the quality of the tracking. An intent of this work was to improve the hit resolution. On this account, several algorithms for reconstructing the hit position of a given cluster of signal strips have been tested. An improved version of the MVD clustering for tracks of near to perpendicular impact was finally implemented, consisting of an adaption of the η algorithm [7]. This improves the new clustering that is part of the pattern recognition system and has a better performance for shallow impact tracks.

The thesis ends with a summary and discussion the of main results.

Chapter 2

Theoretical Framework

2.1 The Standard Model

2.1.1 Basic Properties

Everything we think we know today about high energy physics – besides gravity – is formulated in the Standard Model of particle physics. Gravity stands outside this framework, because the theory of General Relativity describing it lacks a coherent quantum theoretical description. Moreover, its effects in the microscopic world are experimentally inaccessible at the moment and in the foreseeable future. Only at the Planck scale ($M_{\mathrm{Pl}} = \sqrt{\frac{\hbar c}{G_N}} \simeq 10^{19}\,\mathrm{GeV}$, where G_N is Newton's constant[1]) gravity becomes important in particle interactions.

All other known interactions between particles are contained in the Standard Model: The electroweak force [8] (spontaneously broken into electromagnetism and weak interaction by the Higgs mechanism [9]) and the strong force. These forces determine the dynamics of the fundamental fermions, which come in two classes: leptons and quarks. Both classes come in three generations of two flavours (see Table 2.1).

	Generation 1	Generation 2	Generation 3
Quarks	$\begin{pmatrix} u \\ d \end{pmatrix}_L$	$\begin{pmatrix} c \\ s \end{pmatrix}_L$	$\begin{pmatrix} t \\ b \end{pmatrix}_L$
	u_R	c_R	t_R
	d_R	s_R	b_R
Leptons	$\begin{pmatrix} \nu_e \\ e \end{pmatrix}_L$	$\begin{pmatrix} \nu_\mu \\ \mu \end{pmatrix}_L$	$\begin{pmatrix} \nu_\tau \\ \tau \end{pmatrix}_L$
	e_R	μ_R	τ_R

Table 2.1: The fundamental fermions of the Standard Model. The left-handed fields (index L) transform as doublets under SU(2), The right handed fields are SU(2) singlets.

The mathematical framework to describe these forces is relativistic quantum field theory. The properties of the Standard Model are encoded in the Lagrangian $\mathcal{L}$, where the particles enter as fields and the forces become manifest in coupling

[1] c (the speed of light) and $\hbar$ (Planck's constant) are equal to 1 in the natural units used in this thesis

constants and symmetries of the Lagrangian under actions of Lie groups, called local gauge groups. To enforce these symmetries of the Lagrangian, gauge fields belonging to the gauge transformations have to be part of it. Their quanta can be interpreted as gauge particles.

Being a relativistic quantum field theory, the Lagrangian of the Standard Model is also invariant under Poincaré transformations. As a consequence, its fields are representations of the Lorentz group with different spins. The mass fields, describing the leptons and quarks, are fields of spin $\frac{1}{2}$. The gauge bosons have spin 1, the Higgs boson coming from the electroweak symmetry breaking has spin 0, and the quanta of the gravitational field, the gravitons, would have spin 2. Particles with integer spin are called bosons, particles of half-integer spin are fermions.

The gauge group of the Standard Model is $\mathrm{SU}(3) \times \mathrm{SU}(2) \times \mathrm{U}(1)$, a product of Lie groups for the different interactions mentioned above.

SU(3) is the gauge group of quantum chromodynamics, responsible for the strong interactions of coloured quarks. Its gauge bosons are the gluons g, which, due to the non-abelian nature of SU(3), are also coloured and thus itself subject of strong interactions. To fit into the SU(3) structure there have to be eight gluons, differing in their colour charges.

$\mathrm{SU}(2) \times \mathrm{U}(1)$ is the gauge group of electroweak interactions. At low masses it is via the Higgs mechanism spontaneously broken into U(1) for electromagnetic interactions with the photon γ as a gauge boson, and SU(2) for weak interactions with the $W^{\pm}$ and Z^0 bosons. The W and Z acquire a mass in this symmetry breaking, while all other gauge bosons remain massless. The photon couples to all electrically charged particles, while the W and Z bosons couple to all fermions of the Standard Model. Thus the neutrinos, which are neutral and colourless, interact only weakly. Also, the W and Z bosons couple only to particles with left-handed chirality, so that right handed neutrinos do not interact at all with the Standard Model and are considered as non-existent.

2.1.2 Shortcomings

The Standard Model is surprisingly successful: Despite many efforts, no significant deviations from its predictions have been found yet. Nevertheless, it is generally believed that the Standard Model is only a low-energy approximation of some more fundamental theory. The reason for this belief is the following list of shortcomings of the Standard Model:

- Aesthetically unpleasant is the existence of many free parameters: the speed of light c, Planck's constant $\hbar$, the 12 fundamental fermion masses, the CKM mixing angles, the CP violating phase, the three gauge coupling constants, the QCD vacuum angle, the Higgs quadratic coupling and the Higgs self-coupling strength. Historically, science was successful in describing more and more phenomena with less and less basic constants. Therefore it is expected that some of the Standard Model parameters are not really fundamental. Nevertheless, there is no rigorous argument about the number of free parameters a fundamental theory should be allowed to have.

- After the unification of electricity and magnetism into electromagnetism by Maxwell and the unification of electromagnetism and the weak force into the electroweak interaction, there is reason to believe that the electroweak force and the strong force unify at some high energy scale. A naive extrapolation of

the running coupling constants under the assumptions of the Standard Model exhibits only a near miss at a scale around 10^{15} GeV (see Figure 2.7) [10].

- In the Standard Model the question arises why the mass of the Higgs boson is so low compared to the scale at which the effective field theory description breaks down and new physics come into play (i.e. the Planck scale), and why it is not corrected by quadratically divergent terms to the order of the Planck mass. This is called the hierarchy problem [11], and any attempt to solve it within the Standard Model would require an incredible amount of fine tuning.

- There is now convincing evidence that the known visible matter in the universe makes up only about five percent of the whole energy [12]. A much larger fraction, 23%, seems to consist of something that behaves like matter with no electro-magnetic or strong interactions, called dark matter. To be in accordance with the structure formation in the universe [13], most dark matter should be non-relativistic at the beginning of galaxy formation. The Standard Model offers no explanation for the nature of these "cold dark matter" (CDM) particles, although massive neutrinos [14] contribute to some extent to hot dark matter.

- The remaining missing 73% of the total energy of the universe are usually named dark energy. Dark energy can simply be added as a small, positive cosmological constant to the field equations of general relativity, but a particle physics understanding of the nature of this energy density of empty space is still needed. Naive explanations based on dimensional analysis and effective quantum field theory exist, but result in a cosmological constant that is many orders of magnitude too large. So one could as well ask why the cosmological constant is that small [15].

- Still not solved is the question why there is much more matter than antimatter in the visible universe. One condition for such a situation is CP violation [16]. The CP violation of the Standard Model in the CKM matrix [17] is not able to account for the magnitude of the observed asymmetry [18].

- Eventually, a final theory of everything should also include gravity, which is not part of the Standard Model, and is difficult to incorporate into it [19].

Some of these shortcomings are successfully addressed by Supersymmetry (see Section 2.3).

2.2 Deep Inelastic Scattering

When a positron or an electron collides with a proton (as at HERA) and large momentum is transferred, what happens typically is called deep inelastic scattering (DIS) [20]. Figure 2.1 illustrates this in a Feynman diagram. In this interaction a gauge boson is exchanged and interacts with one quark of the proton (*deep* scattering), which tends to disrupt the proton (*inelastic* scattering). Depending on the charge of the exchanged boson the process is called charged current (CC) for a $W^{\pm}$ boson, or neutral current (NC) for a photon or Z^0 boson. In CC the final state lepton is a neutrino, else it is a $e^{\pm}$.

Given the momentum four-vectors k and k' of the incoming and outgoing lepton, the four-momentum of the incoming proton P and the four-momentum of the

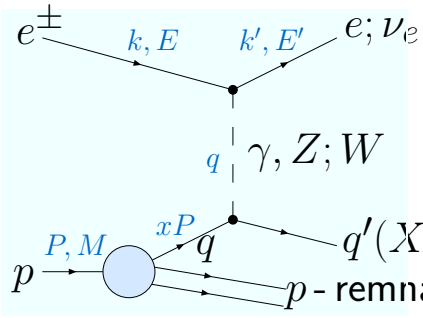

Figure 2.1: Feynman diagram for dominant processes in deep inelastic scattering: Neutral current (NC) with γ or Z^0 exchange and an $e^{\pm}$ in the final state; charged current (CC) with $W^{\pm}$ exchange and a neutrino in the final state.

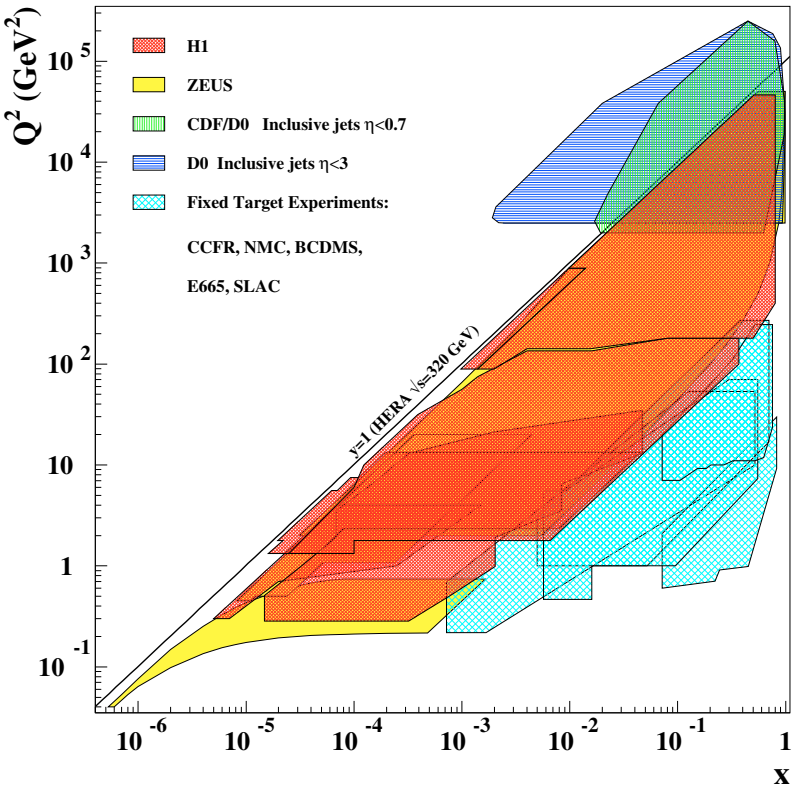

Figure 2.2: (Q^2, x)-plane covered by HERA and other experiments.

exchanged boson q, the kinematics of such processes are usually described by the following variables:

$$s = (k + P)^2, \tag{2.1a}$$

$$Q^2 = -q^2 = (k - k')^2, \tag{2.1b}$$

$$x = \frac{Q^2}{2Pq}, \tag{2.1c}$$

$$y = \frac{qP}{kP}, \tag{2.1d}$$

where s is the squared centre of mass energy of the lepton-proton system. It de-

termines the total available energy. Q^2 is the negative four-momentum squared. It determines the hardness of the collision. In DIS, Q^2 is much greater than $1\,\mathrm{GeV}^2$ (further it is required that the invariant mass of the hadronic system is much larger than the proton mass ($M_X \gg M_p$)). HERA covers a Q^2 region up to $40\,000\,\mathrm{GeV}^2$. The complete kinematic (Q^2, x)-plane is shown in Figure 2.2. The dimensionless variable y is an inelasticity parameter of the interaction. In the proton rest frame it is a measure of the energy fraction the electron transfers to the hadronic system. x is the dimensionless Bjorken scaling variable which indicates the fraction of the proton momentum carried by the struck quark. For vanishing lepton and quark masses the variables are due to momentum conservation related to each other through

$$Q^2 = xys, \tag{2.2}$$

where x and y are by definition in the range $[0, 1]$.

The measured cross section for DIS processes at HERA are shown in Figure 2.3.

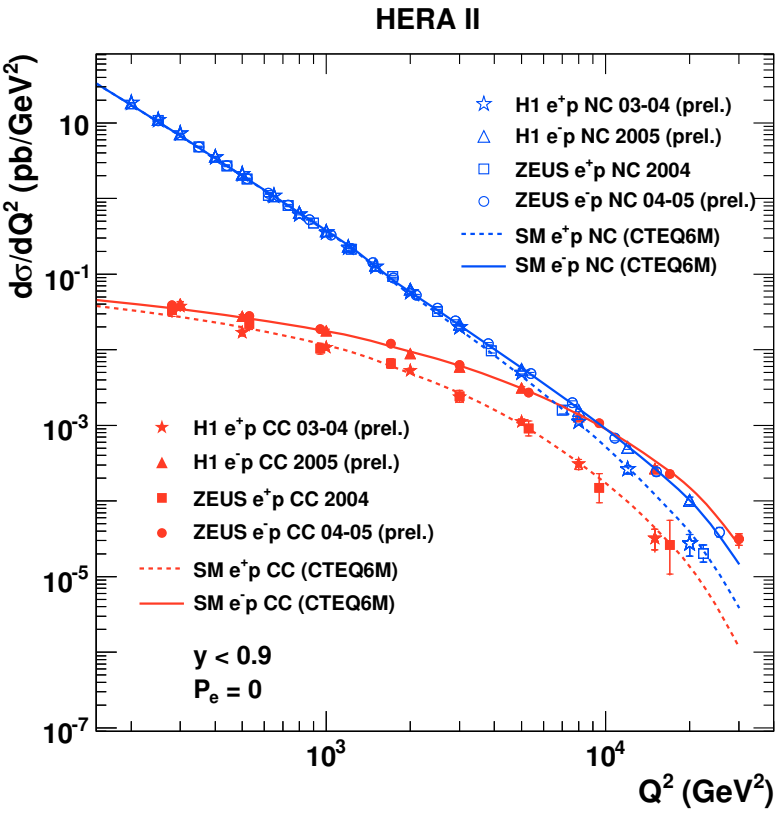

Figure 2.3: Differential cross section for NC and CC DIS as a function of Q^2 measured by H1 and ZEUS.

At low Q^2, the CC processes are suppressed compared to the NC processes, because of the massive propagator term:

$$\sigma^{CC}(\text{low } Q^2) \propto x \frac{1}{(Q^2 + M_W^2)^2}, \tag{2.3}$$

$$\sigma^{NC}(\text{low } Q^2) \propto x \frac{1}{Q^4}. \tag{2.4}$$

At high Q^2, for NC the γ-Z^0 interference kicks in, so that the cross section curves align.

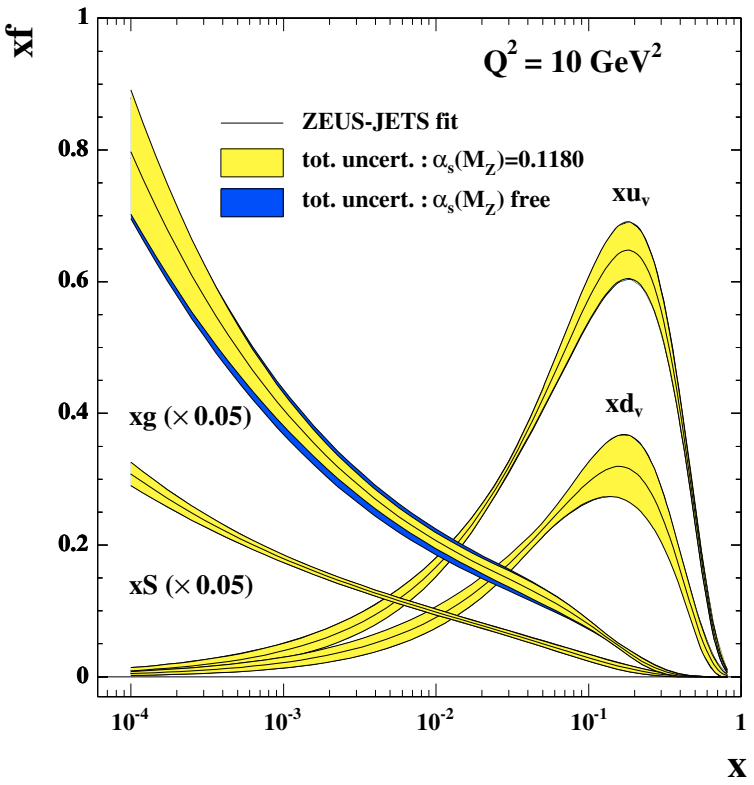

Figure 2.4: Parton density functions as functions of x at $Q^2 = 10\,\mathrm{GeV}$ from ZEUS for valence quarks ($\mathrm{xu_v}, \mathrm{xd_v}$), sea quarks (xS) and gluons (xg).

Also, differences between e^+p and e^-p processes are observed. The reason for this is the different distribution for u and d quarks in the proton (cf. Figure 2.4). This difference is washed out at low Q^2 by the u-d symmetric distribution of sea quarks.

Due to the chiral structure of the weak interaction the cross sections depend also on the longitudinal polarisation

$$P_e = \frac{N_R - N_L}{N_R + N_L} \tag{2.5}$$

of the electrons beam. $N_{R/L}$ are the numbers of right/left handed electrons.

For CC the cross section dependence is simply linear as shown in Figure 2.5.

2.3 Supersymmetry

In four space-time dimensions it is, according to the Coleman-Mandula theorem [1], not compatible with the principles of quantum field theory to extend the Poincaré algebra as a Lie algebra other than as a direct product with a compact Lie algebra (which usually encodes the Standard Model). Haag, Lopuszanski and Sohnius [2]

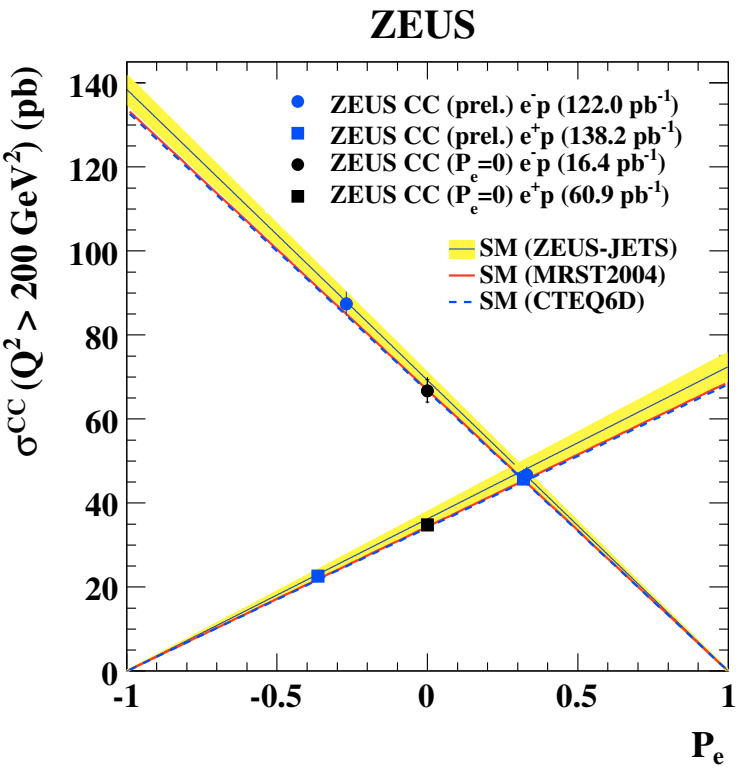

Figure 2.5: Charged current cross section as a function of the lepton beam longitudinal polarisation.

found a unique way to extend the Poincaré algebra as a graded Lie algebra. This approach requires the existence of supersymmetry generators. For only one supersymmetry operator Q the theory is called $N = 1$ supersymmetry (SUSY). Q transforms bosons into fermions and vice versa:

$$Q|\text{boson}\rangle \propto |\text{fermion}\rangle \qquad \text{and} \qquad Q|\text{fermion}\rangle \propto |\text{boson}\rangle. \tag{2.6}$$

The SUSY algebra can be written as:

$$\begin{aligned} \{Q, Q^\dagger\} &= 2\sigma^m P_m, & [Q, M^{mn}] &= \frac{1}{2}\sigma^{mn} Q, \\ \{QQ\} &= \{Q^\dagger, Q^\dagger\} = 0, & [Q^\dagger, M^{mn}] &= \frac{1}{2}\bar{\sigma}^{mn} Q^\dagger, \\ [P_m, Q] &= [P_m, Q^\dagger] = [P_m, P_n] = 0, \end{aligned} \tag{2.7}$$

where M_{mn} are the components of the generators of the Lorentz group and P_m the components of the four-momentum operator $(m, n = 0, 1, 2, 3)$.

The first equation in (2.7) shows that the SUSY generators act in some sense like a "square-root" of the four-momentum operators. From the fact that the SUSY generators commute with the momentum operators it follows that the superpartners in a super-multiplet have the same mass. Since the Q also commute with the gauge group, the superpartners furthermore share electric charge, weak isospin and colour.

For this reason a simple unbroken realisation of SUSY is not realistic: if superpartners would differ only by spin, we would long ago have discovered a scalar partner of the electron, with same charges and mass. This is obviously not the case.

Furthermore, even a spontaneous SUSY breaking of the Standard Model with its superpartners would not be enough to account for the observed particle spectrum, since by systematic construction of supersymmetric Lagrangians (e.g. by the concept of superspace [21]) one finds sum rules that do not allow the entire superpartner spectrum to be more massive than the known spectrum.

2.3.1 SUSY breaking

It is desirable to have soft (i.e. with no quadratic divergences) SUSY breaking, otherwise the hierarchy problem would be re-introduced. The most general way to have the minimal supersymmetric extension of the Standard Model broken softly is formulated in the MSSM (Minimal Supersymmetric Standard Model). The SUSY breaking in the MSSM is explicit: No assumptions regarding the origin of the breaking terms are made. This leads to a total of 124 free parameters, 105 of them being genuinely new [22].

In order to come up with a more physical motivation of the origin of the breaking and to drastically reduce the number of free parameters at the same time, different SUSY breaking scenarios have been developed. Usually the basic idea of these scenarios is the introduction of a hidden sector, which interacts only lightly by non-renormalisable interactions (e.g. by gravitation (e.g. in the mSUGRA model) or indirectly via a messenger sector (e.g. in the Gauge Mediated SUSY Breaking (GMSB) model)) with the usual visible sector. If SUSY is broken spontaneously in the hidden sector, the breaking can be communicated to the visible sector. In an effective low-energy theory for the visible sector the breaking will then become manifest in the form of explicit breaking terms.

One such scenario, the GMSB, which is also the theoretical framework for this analysis, is presented in Section 2.3.4.

2.3.2 Minimal Supersymmetric Standard Model (MSSM)

The MSSM is the minimal supersymmetric extension of the Standard Model. It consists of supermultiplets for each SM particle which contain its superpartner. The only exception is the Higgs sector: Here two doublets are needed to give mass to down-type as well as to up-type quarks. The SM particles differ in spin 1/2 to their superpartners, which are denoted by a tilde over their symbol. The names of scalar partners of SM fermions are built by prefixing the fermions with an "s" (e.g. "selectron" $\tilde{e}$ as the superpartner of the electron e); fermionic partner names of SM bosons are constructed by adding "ino" to the name (e.g. "gluino" $\tilde{g}$ as the superpartner of the gluon g).

An overview of the supermultiplets of the MSSM is presented in Table 2.2. Note, that in the gauge sector there is no unique mass eigenstate partner for example to the photon. The symmetry breaks at a scale above the electroweak breaking scale, so that the binos, winos and higgsinos with same charge mix and combine to gauginos – neutralinos $\tilde{\chi}_i^0$ and charginos $\tilde{\chi}_j^\pm$ respectively.

2.3.3 Properties

There are some reasons to consider Supersymmetry, which – though being of purely conceptual nature – were the driving force for looking into this concept in the first place:

- SUSY is a unique extension of the Poincaré algebra.

Chiral Supermultiplet	Spinor (spin 1/2)	Scalar (spin 0)
Q	(u_L, d_L)	$(\tilde{u}_L, \tilde{d}_L)$
$\bar{U}$	$u_R^\dagger$	$\tilde{u}_R^*$
$\bar{D}$	$d_R^\dagger$	$\tilde{d}_R^*$
L	(ν_L, e_L)	$(\tilde{\nu}_L, \tilde{e}_L)$
$\bar{E}$	$e_R^\dagger$	$\tilde{e}_R^*$
H_u	$(\tilde{H}_u^+, \tilde{H}_u^0)$	(H_u^+, H_u^0)
H_d	$(\tilde{H}_d^0, \tilde{H}_d^-)$	(H_d^0, H_d^-)

Gauge Supermultiplet	Vector (spin 1)	Spinor (spin 1/2)
B	B^0	$\tilde{B}^0$
W	$W^\pm$, W^0	$\tilde{W}^\pm$, $\tilde{W}^0$
g	g	$\tilde{g}$

Table 2.2: Supermultiplets of the MSSM.

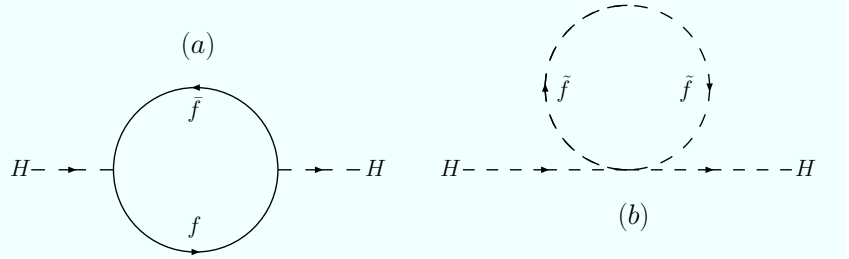

Figure 2.6: Cancellation of first order corrections to the Higgs mass between a fermionic loop (a) and a "sfermionic" tadpole (b) Feynman diagram.

- It unifies matter (made up of fermions subject to the Pauli exclusion principle) and forces (made up of bosons) in one consistent and symmetric framework.
- History proved that it is often wise to replace a global symmetry by a local symmetry. Making the parameters generating SUSY transformation local directly leads to local Poincaré symmetry, which is the foundation of General Relativity and thus gravity. Local SUSY is called Supergravity (SUGRA).
- SUSY seems to be a necessary ingredient of Superstring theory [23], which is one of the most promising candidates for a theory unifying gravity and quantum theory.

Apart from these rather theoretical or aesthetic arguments, there are a number of more solid – or at least practical – arguments in favour for Supersymmetry:

- The hierarchy problem described in Section 2.1.2 is solved by Supersymmetry. For every fermionic quadratically divergent contribution to the Higgs mass there is now a bosonic one with same coupling but opposite sign, which cancels the fermionic contribution, as illustrated in Figure 2.6, and vice versa. This mechanism works to all orders in perturbation theory, but is only exact in

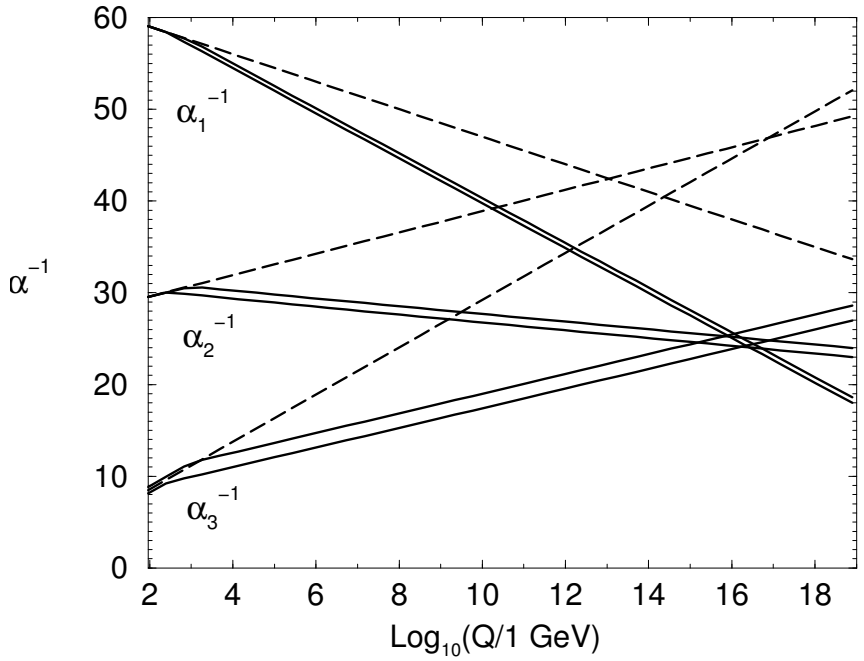

Figure 2.7: Running of the gauge couplings, as described by the renormalisation group equations, with SUSY (continuous lines) and without SUSY (dashed lines).

unbroken SUSY (which is unrealistic). In the case of broken SUSY the Higgs mass is subject to quadratic corrections proportional to the SUSY breaking scale. In order to still solve the Hierarchy problem the SUSY breaking scale should not be much higher than 1 TeV.

- Figure 2.7 shows that in SUSY all three gauge couplings can unify at a scale $Q \approx 10^{16}\,\text{GeV}$, which is known as the GUT (grand unification theory) scale. This is not the case in the Standard Model. The addition of new particles changes the renormalisation group equation, which determine the slope of the running of the gauge couplings, in such a way that unification is possible. Again, this works only for a SUSY breaking scale of the order of 1 TeV [24].

- Some supersymmetric theories provide a good dark matter candidate. It is the lightest supersymmetric particle (LSP), which is in many models neutral. In theories with conserved R-parity (see Section 2.3.5), the LSP may not decay and is stable. Even in some theories with violated R-parity a particle like the gravitino (the supersymmetric partner of the graviton) might be stable enough to provide a candidate for dark matter [25].

- Some low-energy observations seem to be more consistent with some parts of the SUSY parameter space than the Standard Model. One example is the value of muon anomalous moment $(g-2)_\mu$, which deviates from the observed value by 3σ [26]. Another example is the inclusive decay rate for $b \to s\gamma$, where a slight discrepancy between the Standard Model and the experiment is observed [27], which is predicted by some regions of the MSSM parameter space [28].

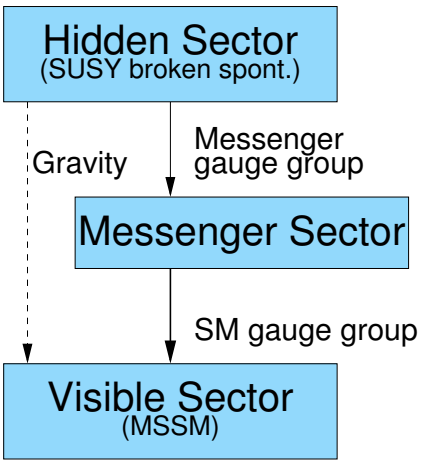

Figure 2.8: Concept of how the spontaneously broken Supersymmetry in a hidden sector is communicated via a messenger sector to the visible sector. In the absence of a messenger sector, the SUSY breaking is communicated via gravity to the visible sector, which is the basis of the mSUGRA model.

2.3.4 Gauge Mediated Supersymmetry Breaking

In the GMSB [29] there is a hidden sector where SUSY is spontaneously broken at an energy scale $\sqrt{F}$ (see Figure 2.8). The hidden sector interacts with a messenger sector at a scale M_{mess} via a messenger gauge group. This messenger sector communicates the SUSY breaking via Standard Model gauge interactions to the visible sector at a scale Λ (there is also direct gravitational interaction between the hidden sector and the visible sector, but this effect is small compared with the strength of gauge interactions in the GMSB). Λ determines all low-energy scalar and gaugino masses through loop effects. It has to be of the order of 100 TeV for sparticle masses of the order of 1 TeV.

The scale of SUSY breaking in the hidden sector also determines the gravitino mass

$$m_{\tilde{G}} = \frac{F}{\sqrt{3}M_{\text{Pl}}} \simeq \left(\frac{\sqrt{F}}{100\,\text{TeV}}\right)^2 \text{eV}, \tag{2.8}$$

which is usually quite low in the GMSB, so that the gravitino is the lightest supersymmetric particle (LSP). The gravitino emerges in the GMSB from the Super-Higgs mechanism and thus interacts not only gravitationally. For instance, it couples also to the photon. The next-to lightest supersymmetric particle (NLSP) decays into its Standard Model partner and a gravitino, and shapes the phenomenology of the GMSB.

In the minimal GMSB model the messenger sector is assumed to be as simple as possible, i.e. a representation of SU(5). Consequently, the maximal number of messenger fields is

$$N \leq 5. \tag{2.9}$$

The two remaining parameters of the GMSB arise from the radiative electroweak symmetry breaking: $\tan\beta$ and $\text{sgn}\,\mu$. $\tan\beta$ is the ratio of the vacuum expectation values of the two Higgs doublets. It should have a value between 2 and around

Parameter	Meaning
$\sqrt{F}$	Spontaneous SUSY breaking term (hidden sector)
M_{mess}	Mass scale of the messenger particles
N	Number of messenger multiplets
Λ	Soft SUSY breaking scale
$\tan\beta$	Ratio of the vacuum expectation values of the two Higgs doublets
$\operatorname{sgn}\mu$	Sign of the bi-linear Higgs term in the superpotential

Table 2.3: Free parameters of the GMSB model.

50 [30]. μ is the coefficient for the bi-linear Higgs term in the superpotential[2]. In the GMSB only the sign of μ is relevant. All free GMSB parameters are summarised in Table 2.3.

There are different scenarios for the NLSP:

Neutralino NLSP The lightest neutralino $\tilde{\chi}_1^0$ is the NLSP. This is the case for small N, large M_{mess} and small $\tan\beta$.

Stau NLSP The lightest stau $\tilde{\tau}_1$ (there are two $\tilde{\tau}$ because of the mixing between the superpartners of the right handed and left handed $\tau_{R/L}$) is the NLSP. This happens for large N, small M_{mess} and large $\tan\beta$.

Slepton co-NLSP All charged sleptons are almost mass degenerate and decay only into the LSP and their SM partner. Precondition is that $\tan\beta$ is small, while N and M_{mess} are medium.

Neutralino-slepton co-NLSP All above discussed candidates have almost the same mass and decay only into the LSP and their SM partner. $\tan\beta$ has to be large, while N and M_{mess} are medium.

Depending on the NLSP mass and the hidden sector SUSY breaking scale, the lifetime τ of the NLSP can be considerable. In the case of a neutralino NLSP it is given by

$$c\tau_{\tilde{\chi}_1^0} \simeq= \frac{1}{100}\left(\frac{\sqrt{F}}{100\,\text{TeV}}\right)^4\left(\frac{m_{\tilde{\chi}_1^0}}{100\,\text{GeV}}\right)^{-5}. \tag{2.10}$$

The corresponding decay length $L = \gamma\beta c\tau$ can be large enough to allow a decay outside the detector. The signature would be just missing energy.

If the neutralino decays inside the detector the signature is missing energy (from the gravitino) and an isolated photon. If a stable slepton is the NLSP, the signature can be an unknown charged particle if it is long-lived; else one observes an isolated lepton and missing energy.

2.3.5 *R*-Parity

R-parity (R_p) [31] is a discrete multiplicative quantum number defined by

$$R_P = (-1)^{3B+L+2S} \tag{2.11}$$

for a given particle. B is the baryon number, L the lepton number and S the spin. All SM particles have $R_p = +1$, so conservation of R-parity is a trivial symmetry of

[2] The superpotential is one element in the SUSY Lagrangian.

the SM. When R-parity is conserved, the LSP has to be absolutely stable. Because the LSP is the lightest neutralino in most scenarios, R-parity conservation (RPC) provides often a natural dark matter candidate. Another consequence of RPC is, that SUSY particles can only be produced in pairs.

If R-parity is allowed to be violated (RPV), additional terms appear in the superpotential:

$$W_{\mathrm{RPV}} = \lambda_{ijk} L_i L_j \bar{E}_k + \lambda'_{ijk} L_i Q_j \bar{D}_k + \lambda''_{ijk} \bar{U}_i \bar{D}_j \bar{D}_k + \mu'_i L_i H_u, \tag{2.12}$$

where λ_{ijk}, λ'_{ijk} and λ''_{ijk} are Yukawa coupling constants, and i, j, k are family indices. The λ'' term violates baryon number conservation, the other terms violate lepton number conservation.

From low energy observations there are different limits on the R-parity violating couplings:

- Lower limits on the proton lifetime impose limits on the product of different Yukawa coupling terms. Single non-vanishing RPV terms are not affected. Therefore it is assumed in this thesis that not more than one coupling constant has a non-vanishing value.

- The non-observation of the neutrinoless double β-decay ($0\nu2\beta$) can be used to restrict λ'_{111} as a function of the squark and gluino masses [32]:

$$|\lambda'_{111}| < 10^{-4} \left(\frac{m_{\tilde{q}}}{100\,\mathrm{GeV}}\right)^2 \left(\frac{m_{\tilde{g}}}{100\,\mathrm{GeV}}\right)^{\frac{1}{2}}. \tag{2.13}$$

  Since the process under investigation in this thesis does not incorporate any squarks, we can safely assume a squark mass $m_{\tilde{g}}$ high enough to not constrain λ'_{111}.

Chapter 3

Experimental Setup

3.1 The HERA Collider

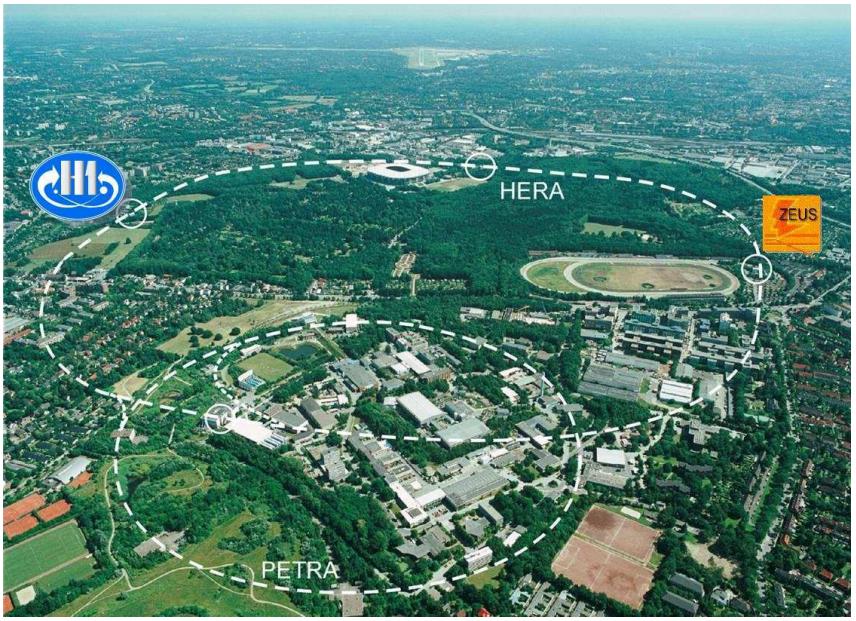

Figure 3.1: An aerial view of DESY. The main campus is the area encircled by HERA's pre-accelerator PETRA (smaller dashed circle), the HERA collider (bigger dashed shape) extends beneath the Altonaer Volkspark and the Stadium. The HERA south hall with the ZEUS detector is off the main DESY ground, next to the Trabrennbahn.

HERA (*Hadron-Electron-Ring-Anlage*) [33] was a particle collider located at DESY Hamburg in Germany (see aerial view in Figure 3.1). Between 1984 and 1990 it was built in a 6.3 km long tunnel, on average 20 m underground. HERA started operation in 1992. In the first years electrons or positrons with an energy of $E_e = 27.5\,\text{GeV}$ were brought to collision with protons of $E_p = 820\,\text{GeV}$. In 1998 the proton energy was raised to $E_p = 920\,\text{GeV}$, resulting in a centre of mass energy of

$$\sqrt{s} = \sqrt{4E_pE_e} \approx 318\,\text{GeV}.$$

A bigger shutdown occurred in 2000 for a luminosity upgrade and the option to have the lepton beam longitudinally polarised by spin rotators [34].[1] The following

[1] In contrast, transversal polarisation (which does not affect the physics of the collisions) is

running phase is often labelled the HERA II running period. In 2007 HERA stopped operation, ending with a period of runs with lower proton energies.

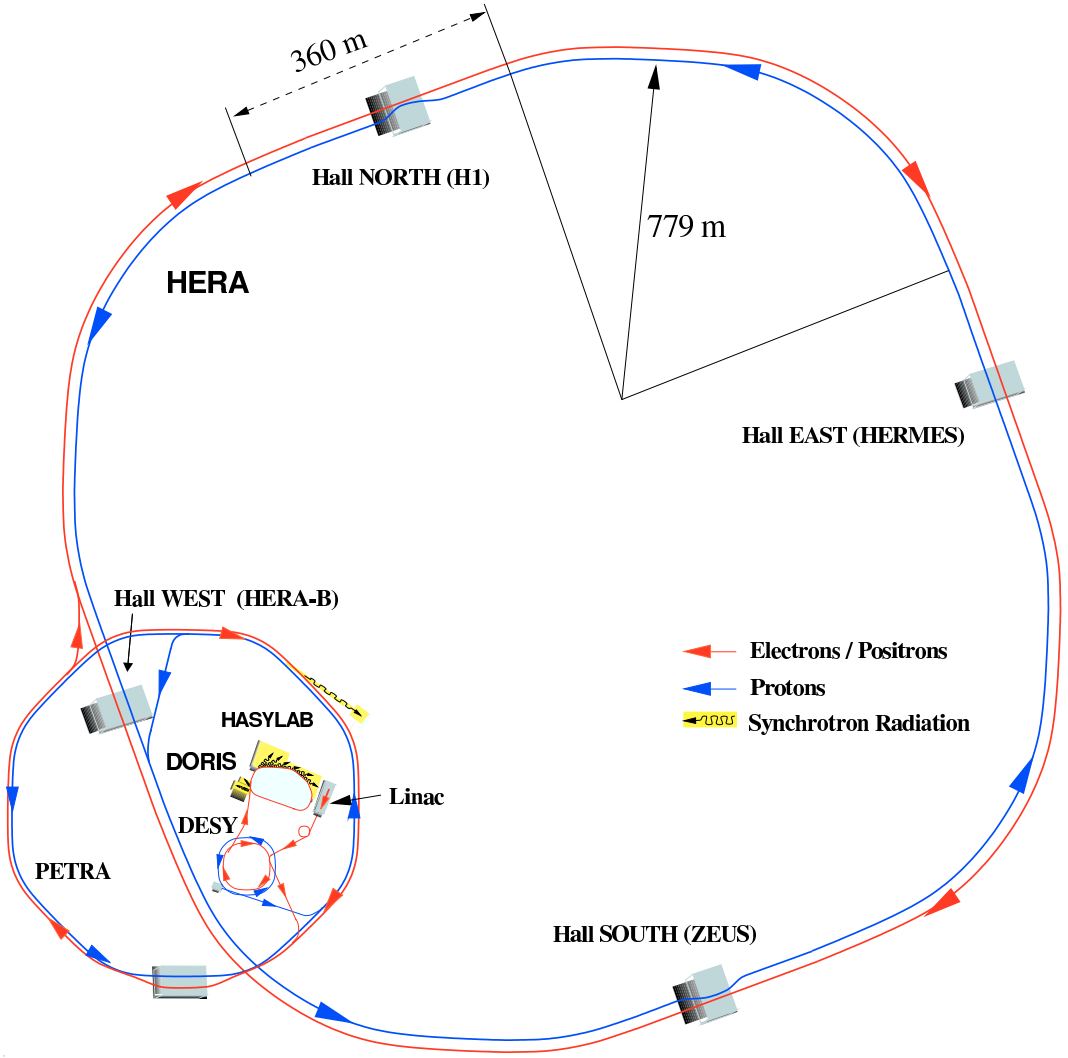

Figure 3.2: Schematic view of the HERA rings and the pre-accelerators.

The ring tunnel consists of four circular and four straight sections (Figure 3.2). The leptons and the protons were stored in two separate rings. The lepton beam was accelerated by normally and super-conducting cavities to compensate for the energy loss due to synchrotron radiation (which scales with $E^4 m^{-4} r^{-1}$ and is very high for low mass particles like electrons), while the magnets guiding the beam were normal conducting with a field strength of 0.165 T. In contrast, the protons were accelerated by normal-conducting cavities and guided by superconducting magnets with a field strength up to 4.65 T.

At two points the beams crossed, providing collisions for the experiments H1 and ZEUS (two fixed target experiments, HERMES and HERA-B used only the electron beam and the proton beam, respectively).

The design maximum luminosity was $\mathcal{L} = 1.6 \cdot 10^{31} \mathrm{cm}^{-2} \mathrm{s}^{-1}$. Figure 3.3 plots the integrated luminosity per experiment delivered by HERA as a function of running

achieved by self-polarisation via synchrotron radiation [35].

time.

In this analysis only HERA II data are used.

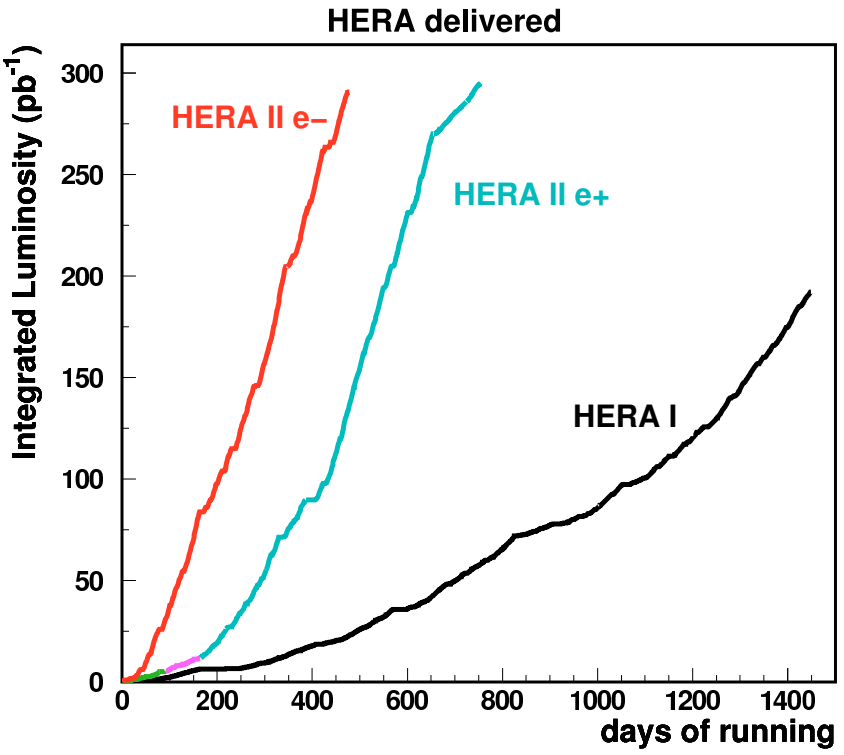

Figure 3.3: Integrated luminosity delivered by HERA as a function of running days, separated into HERA I (mostly e^+p runs), HERA II e^-p and HERA II e^+p runs.

3.1.1 Polarisation Measurement

By emission of synchrotron radiation the electrons in the HERA ring got a transverse polarisation P_T via the Sokolov-Ternov effect [35]:

$$P_T(t) = -P_{\max}(1 - e^{-t/\tau}), \tag{3.1}$$

where the build up time τ for the lepton beam at HERA was $\tau \sim 40\,\text{min}$ and $P_{\max}$ on average 35%.

With the help of spin rotators [34] before and after the interaction points the transverse polarisation was converted into a longitudinal polarisation by transverse magnetic fields.

The transverse and longitudinal polarisation was measured by TPOL and LPOL, respectively, with circular polarised laser beams, taking advantage of the polarisation dependence of Compton scattering. LPOL measured the energy asymmetry of backscattered photons form left- and right-handed polarised laser beams, TPOL measured the angular asymmetry. Both could measure single bunches and thus were able to deal with the polarisation dependence between colliding and non-colliding bunches. The relative uncertainty is 4.2% in the TPOL measurement and 3.6% in the LPOL measurement.

3.2 The ZEUS Detector

The ZEUS detector was designed as a multi-purpose detector with nearly hermetic coverage [36]. A cross sectional view along the beam pipe is shown in Figure 3.4, a view perpendicular to the beam pipe is shown in Figure 3.5. Note that these figures show the original design, before the upgrade.

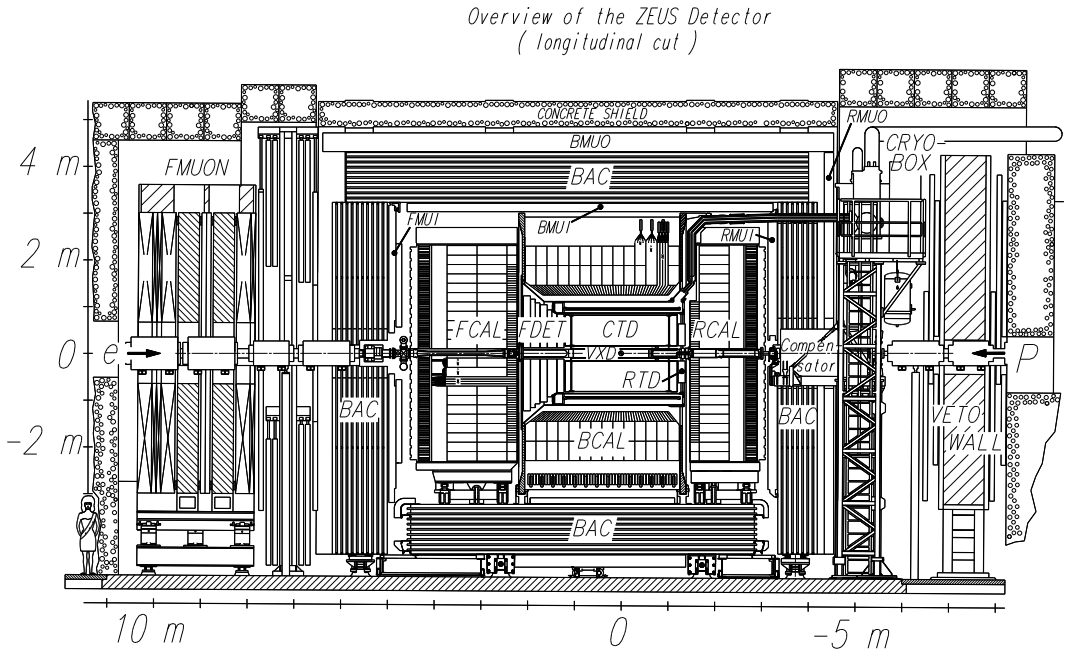

Figure 3.4: Cross sectional view of the original ZEUS detector (before modifications and upgrades) along the beam pipe.

Closest to the beam pipe is the Micro Vertex Detector (MVD, see Section 3.2.1), a silicon strip detector which improved the reconstruction of primary and secondary vertices of the interaction. The MVD was installed in 2001; until 1995/1996 a different vertex detector (VXD) was in use.

For the identification and measurement of tracks of charged particles the central tracking detector (CTD, see Section 3.2.2), a drift chamber, was in use for the central region, complemented by the straw tube tracker (STT) for the forward region (before the 2001 upgrade a different setup was in use: a forward detector (FDET) and a rear tracking detector (RTD) complemented the CTD). To determine charge and momentum the tracking system was surrounded by a superconducting solenoid providing a magnetic field of 1.8 T.

In order to measure the energy, an uranium-scintillator calorimeter system enclosed the CTD. It was divided into a barrel (BCAL), a forward (FCAL) and a rear (RCAL) part and was surrounded by a backing calorimeter (BAC), which measured late showering particles. Additionally, it operated as a magnetic yoke.

The muon detector system was in parts located inside (FMUI, BMUI and RMUI), and in part located outside (FMUON, BMUON, RMUON) the yoke.

Forward in these contexts means in the direction of the proton beam (in which the centre of mass system of the interaction is boosted), chosen as the z axis of the right-handed Cartesian coordinate system of ZEUS (see Figure 3.6). The y axis

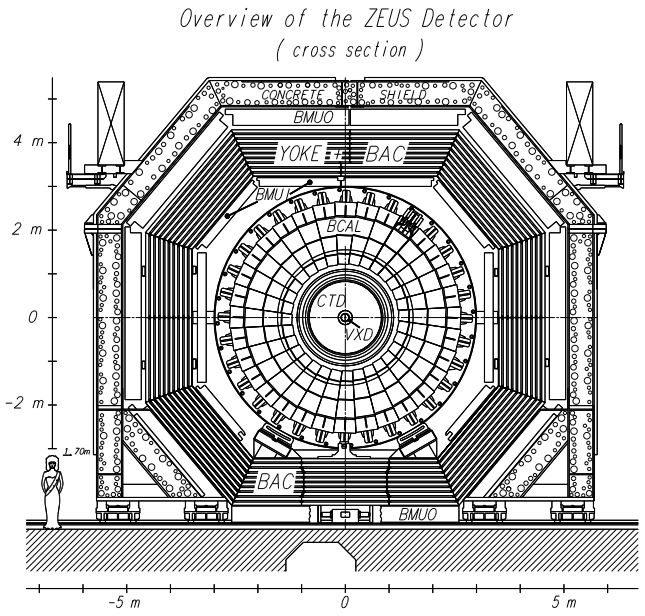

Figure 3.5: Cross sectional view of the original ZEUS detector (before modifications and upgrades) perpendicular to the beam pipe.

points upwards, the x axis to the centre of HERA, the origin is at the nominal interaction point.

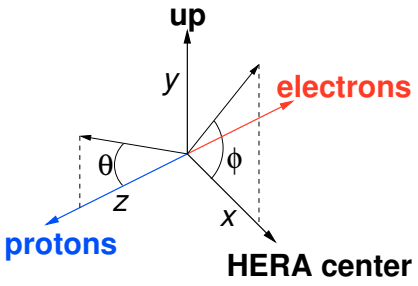

Figure 3.6: The ZEUS reference coordinate system.

3.2.1 Micro Vertex Detector

The Micro Vertex Detector (MVD) [6] was installed in 2001 to extend the tracking acceptance, efficiency and resolution and improve vertex reconstruction. It was a silicon strip detector with a readout strip pitch of 120 µm. It consisted of a barrel (BMVD) and a forward (FMVD) part.

The BMVD was a 63 cm long cylinder with silicon sensors arranged in three concentric layers (numbered outwards cylinder 0, 1 and 2) around the elliptical beam pipe to give ideally three spatial measurements per track. Due to geometrical restrictions the innermost layer did not cover the whole polar range (see Figure 3.7). The sensors were 64.2 mm × 64.2 mm in size, with a thickness of 300 µm, and had 512 readout channels. They were installed in the form of modules, in which a sensor with strips in z direction was mounted on top of a sensor with strips in $r\phi$ direction, to have three coordinates for each hit (after the pattern recognition phase of the

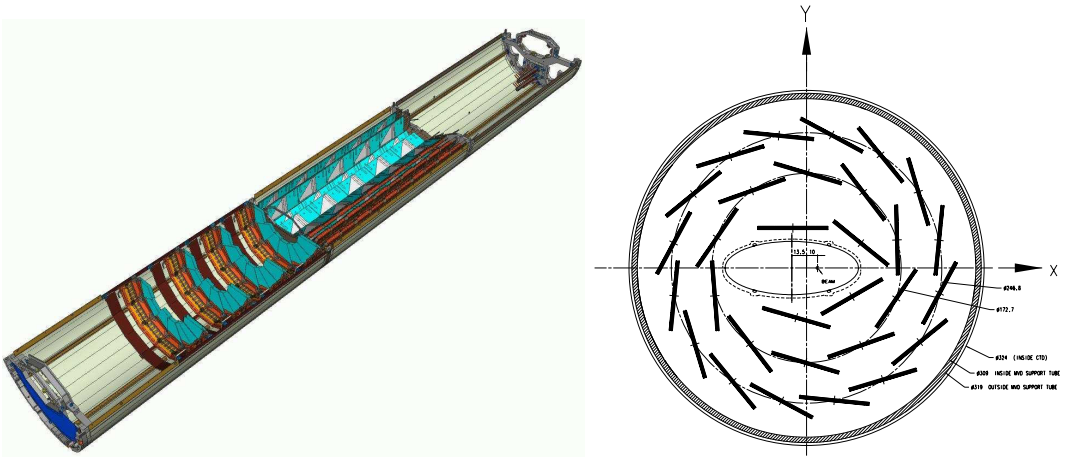

Figure 3.7: Left: Layout of bottom part of the MVD. Right: Cross section of the barrel MVD.

event reconstruction system eliminated ghost hits, which result from ganging of the sensor readout channels in the modules).

The FMVD consisted of four vertical planes (called wheels, numbered 0 to 3 in forward direction) extending the angular coverage down to 7° from the beam line. The FMVD sensors were wedge shaped and with 480 readout channels. Apart from these geometric properties they were identical to the BMVD sensors. The two layers in each wheel were tilted to provide two coordinates for a traversing particle in each wheel.

3.2.2 Central Tracking Detector

The central tracking detector (CTD) [37] was a cylindrical wire chamber used to measure direction and momentum of charged tracks and estimate the energy loss dE/dx to help particle identification.

The CTD was divided into nine super-layers, each consisting of eight sense wire layers. Figure 3.8 shows a cross sectional view of a CTD segment.

The active radius was 18.9–79.4 cm, the active length was 204 cm. Taking into account that a measured track was required to cross at least two super-layers, the polar angle coverage was 15°–165°. Each of the 576 basic cells was made up of eight sense wires surrounded by 34 drift wires. The drift chamber was filled in an 85 : 5 : 1 proportion with a gas mixture of argon (Ar), carbon dioxide (CO_2) and ethane (C_2H_6) bubbled through ethanol (C_2H_6O) at atmospheric pressure. Charged particles traversing the CTD ionised the gas along their trajectories. The produced electrons drifted to the sense wires and generated additional electron-ion-pairs in the high field close to the sense wires, which led to an avalanche and a multiplication of the signal of typically 10^4–10^5.

Due to the magnetic field the drifting electrons were affected by a Lorentz force, which caused their path to be tilted by an Lorentz angle of 45° with respect to the radial direction. To ensure an optimal drift path and minimise the drift time (which is ~ 500 ns at a maximum), the wire planes were oriented at the same angle. The wires of the five odd numbered super-layers were parallel to the chamber axis, while those of the four even numbered super-layers were tilted by stereo angles of about ±5° with respect to the beam line, to get a z coordinate resolution $\sigma_z = 2$ mm.

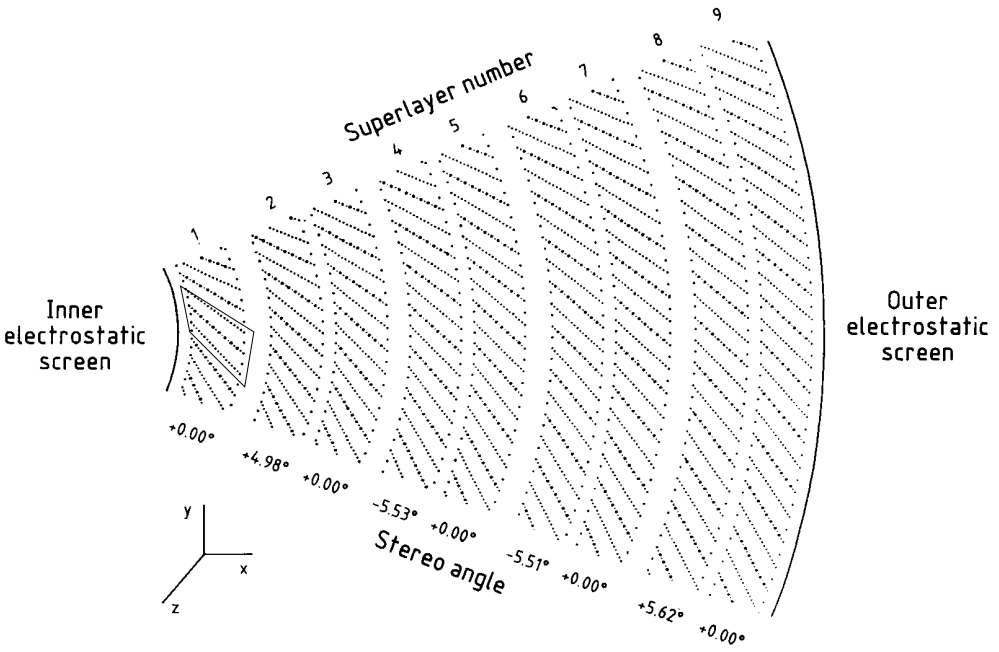

Figure 3.8: Cross sectional view of a CTD segment. Shown are the nine super-layers with their different stereo angles. They are numbered from one to nine from the innermost to the outermost.

The $r\phi$ resolution was θ-dependent about $\sigma_{r\phi} = 200\,\mu\text{m}$. For trigger purposes the z coordinate reconstruction via the stereo angle was too slow. Consequently three super-layers had been equipped to provide timing measurements. The z position was obtained by measuring the difference of the propagation times of the signal to the opposite ends of a wire. However, the resolution of this method is only $\sigma_z = 4\,\text{cm}$.

By extrapolating the reconstructed tracks to the beam axis, the primary vertex can be calculated with a resolution of the order 0.4 cm in z direction and 0.1 cm in transverse direction.

In order to get momentum information the CTD was inside a magnetic field of 1.43 T provided by the superconducting solenoid. The resolution for high transverse momentum (p_T) was in the HERA I running period

$$\frac{\sigma(p_T)}{p_T} = \underbrace{0.0058 \cdot p_T[\text{GeV}]}_{\text{hit position resolution}} \oplus \underbrace{0.0065}_{\text{multiple scattering in the CTD}} \oplus \underbrace{0.0014/p_T[\text{GeV}]}_{\text{multiple scattering before the CTD}}$$

at $\theta = 90°$.

With the installation of the MVD in 2001 additional material was introduced before the CTD, whereas the MVD hit information improved the hit resolution. The relative transverse momentum resolution was then

$$\frac{\sigma(p_T)}{p_T} = 0.0026 \cdot p_T[\text{GeV}] \oplus 0.0104 \oplus 0.0019/p_T[\text{GeV}].$$

3.2.3 Uranium-Scintillator Calorimeter

The uranium-scintillator calorimeter (CAL) [38] used in the ZEUS detector was designed to have high resolution for both hadronic and electromagnetic energies. It

consisted of three parts, as depicted in Figure 3.9, that completely surrounded the tracking devices: The forward calorimeter (FCAL), the barrel calorimeter (BCAL) and the rear calorimeter (RCAL). Furthermore, the CAL was divided into an electromagnetic layer (EMC) and a hadronic layer, consisting of two hadronic segments (HAC1, HAC2) in the FCAL and BCAL and one segment (HAC1) in the RCAL.

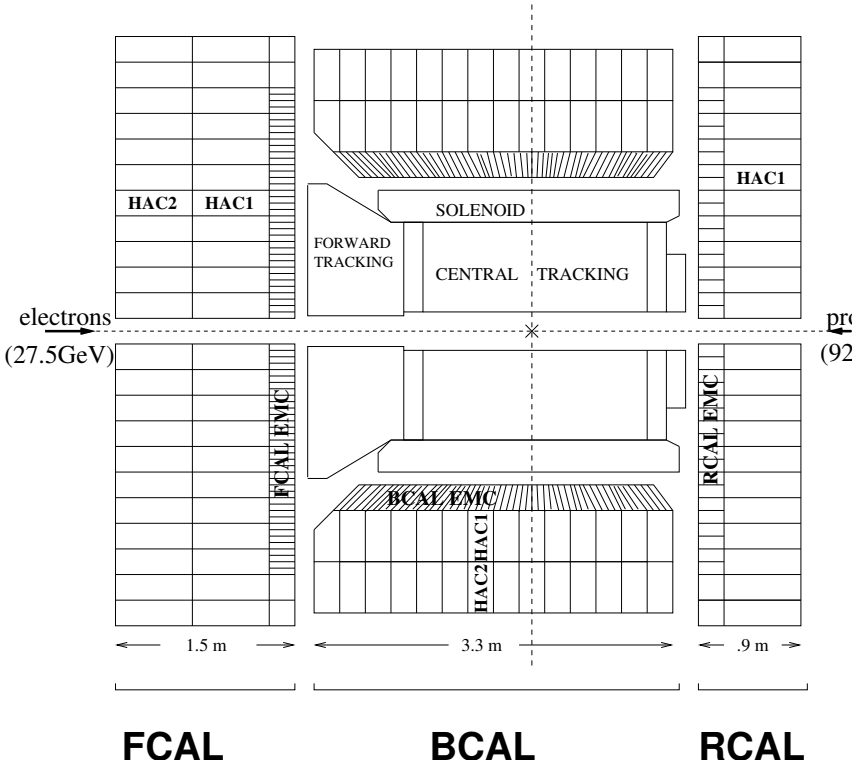

Figure 3.9: Cross sectional view of the ZEUS calorimeter.

The FCAL was thicker (7λ; λ is the hadronic absorption length) than BCAL (5λ) or RCAL (4λ), because most particles produced in the lepton-proton interaction were boosted in the forward (proton) direction. In terms of electromagnetic radiation length X_0 the section had a thickness of $26X_0$ for FCAL and RCAL, and $21X_0$ for the BCAL. As a result at least 90% of the jets with the kinematically allowed maximum energy deposited at least 95% of their energy in the CAL.

FCAL and RCAL were subdivided into 23 rectangular modules (see Figure 3.10 for an FCAL module), the BCAL was subdivided into 32 wedge shaped modules (covering an azimuthal angle of 11.25°). Each module consisted of towers, which were subdivided into electromagnetic and hadronic sections. The sections were made up of cells, as shown in Figure 3.10.

The active part of the CAL consisted of alternating layers of absorbers and scintillators. The absorbers were 3.3 mm thick depleted uranium plates (98.1% U^{238}, 1.7% Nb, 0.2% U^{235}), in which traversing particles lost energy and produced showers. The shower particles excited fluorescence molecules in the organic scintillator (SCSN-38 polystyrene), which emitted photons when passing to lower energy bands. Wave-length shifter plates (WLS) were attached on both sides of the modules to the scintillator plates to catch the scintillator light. Light from the WLS was transferred via light guides to photomultiplier tubes mounted behind the modules. The photo-multipliers converted the photon signal to an electrical signal. The thickness

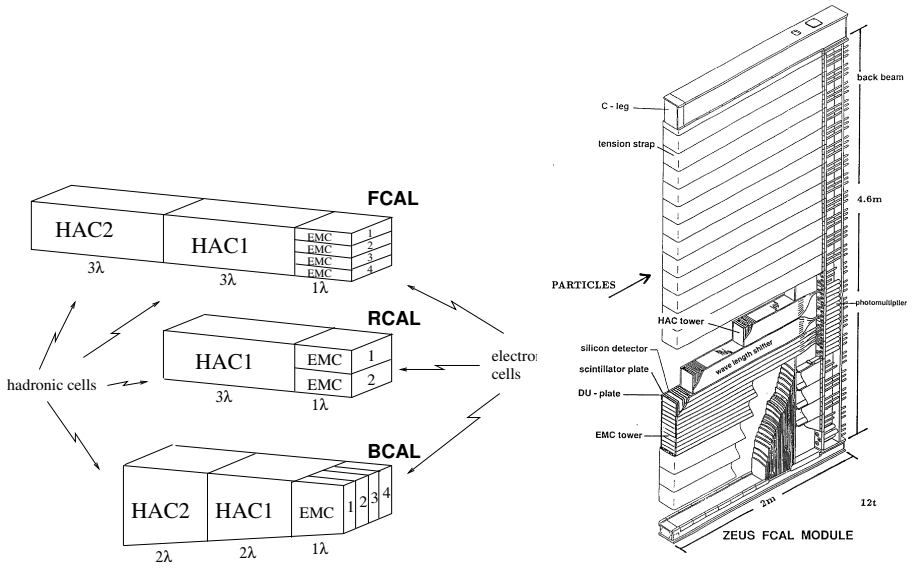

Figure 3.10: Schematic view of CAL towers (left) and FCAL modules (right).

of absorber and scintillator was balanced in order to give the same response for an electron and a hadron of the same energy ($e/h = 1.00 \pm 0.02$). This mechanism is called compensation and allows for good resolution of hadronic energy:

$$\frac{\sigma_{\mathrm{em}}(E)}{E} = \frac{18\%}{\sqrt{E[\mathrm{GeV}]}} \oplus 1\% \qquad \text{and} \qquad \frac{\sigma_{\mathrm{had}}(E)}{E} = \frac{35\%}{\sqrt{E[\mathrm{GeV}]}} \oplus 2\%,$$

as determined in test beam measurements.

The CAL was calibrated on a daily basis using the natural radioactivity of U^{238}, which produced a constant signal in the photomultiplier tubes. Additionally, laser, LED and test pulses were used for the calibration. The achieved accuracy was better than 1%.

Besides, the CAL had a good time resolution $\sigma_t < 1\,\mathrm{ns}$ for energy deposits $E > 4.5\,\mathrm{GeV}$. Thus, the timing information can be used to reject non-ep background.

3.2.4 Trigger and Data Acquisition System

The HERA bunch crossing time was 96 ns. With 150 kB per event the resulting data stream would have been much too large to store, if for every bunch crossing the detector had been read out. Moreover, it would have contained mostly practically empty events and to a large degree ($\sim 10\,\mathrm{kHz}$) events coming from non-ep interactions: Proton beam gas interactions and proton beam halo events or muons (either of cosmical origin or from decaying hadrons that were produced when protons from the beam halo hit collimators) crossing the detector. Highest rates for useful ep physics events (assuming an instantaneous luminosity of $2 \cdot 10^{31}\,\mathrm{cm^{-2}s^{-1}}$) occurred for soft photoproduction events ($\sim 250\,\mathrm{Hz}$). NC DIS events with $Q^2 > 100\,\mathrm{GeV}^2$ happened at less than 0.1 Hz and CC DIS events at the order of 1 mHz.

The task of the ZEUS trigger system [39] was to reduce the data rate to manageable capacities and keep the interesting events. This was achieved in three levels of increasing sophistication. The three levels (shown in Figure 3.11) were:

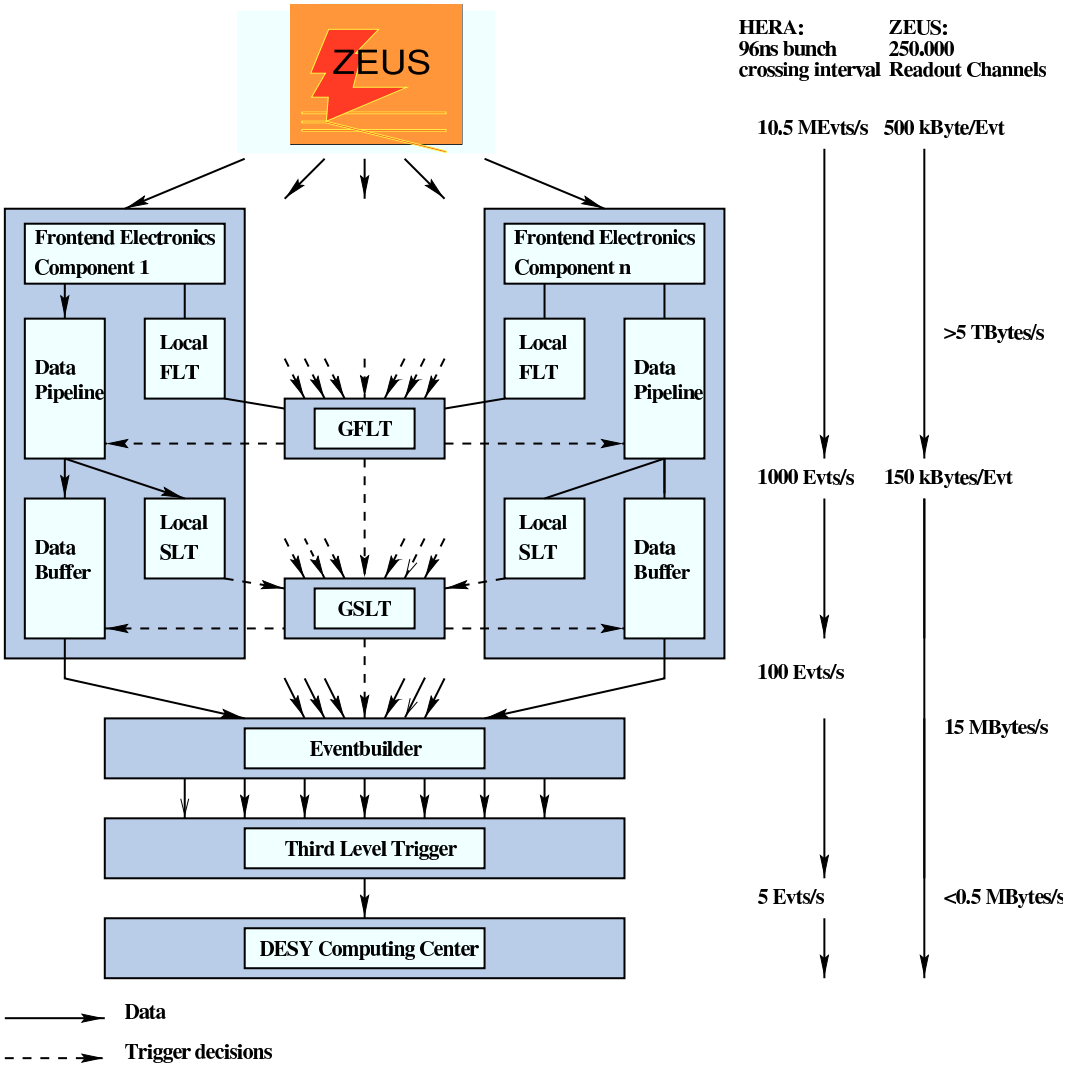

Figure 3.11: Schematic diagram of the ZEUS trigger and data acquisition system.

First Level Trigger (FLT): The FLT was made up of hard-wired logical circuits for each component separately, based on fast computable variables like energy sums and timing information. The global first level trigger (GFLT) collected the information from the different trigger slots. Until it came to a decision (which happened within 46 bunch crossings) the components buffered the event information in a pipeline clocked by the HERA bunch crossing rate. The accepted events were passed to the second level trigger with an output rate of 1 kHz.

Second Level Trigger (SLT) The SLT was implemented in a transputer network. At this trigger level more information and correlations between different detector components could be taken into account more accurately (track momenta, vertex position, electron and jet finding, CAL timing information). The information from all SLT branches was combined into the global second level trigger (GSLT), which reduced the event rate to about 50–100 Hz.

Third Level Trigger (TLT) For the events accepted by the GSLT the informa-

tion from all the detector components was sent to the event builder, which combined the event information and stored it in an ADAMO [40] database record. The third level trigger used a computer farm and had access to this ADAMO database and the reconstruction code to select events according to specific physics requirements. It reduced the output rate to 5–10 Hz and stored the accepted events to tape at the DESY computing centre. During this, a pseudo fourth level trigger was introduced by assigning DST (data summary tapes) bits, which indicate whether an event fulfils certain requirements and ensure later fast access to given classes of events.

3.2.5 Luminosity Measurement

The luminosity at ZEUS was measured with the bremsstrahlung process $ep \to ep\gamma$. This QED process is theoretically well understood and provides due to its high cross section ($\sigma_{\text{brems}} = \mathcal{O}(20\,\text{mb})$) a fast and continuous monitoring of the event rate.

To this effect the rate and energy of the bremsstrahlung photons was measured with the luminosity monitoring system [41], schematically illustrated in Figure 3.12. It consisted mainly of a photon calorimeter (LUMIG) situated at $z = -106\,\text{m}$ and a lepton calorimeter (LUMIE) at $z = -35\,\text{m}$. The detected photons left the beam pipe at $z = -92.5\,\text{m}$ through a $\text{Cu} - \text{Be}$ window. To protect the photon calorimeter it was shielded against synchrotron radiation by a carbon-lead filter.

With the rate $\dot{N}_{\text{brems}}$ of detected photons above a fixed energy threshold, the luminosity is calculated as

$$\mathcal{L} = \frac{\dot{N}_{\text{brems}}}{\sigma'_{\text{brems}}}, \tag{3.2}$$

where the cross section σ'_{brems} is corrected for the detector acceptance.

To estimate background events from bremsstrahlung of leptons on the residual gas, pilot bunches where the proton bunch is empty are used.

Due to the large rate of recorded Bethe-Heitler events the statistical uncertainties are negligible. Systematic uncertainties come from background subtraction, pile-up effects, energy calibration and the acceptance of the lead-scintillator photon calorimeter (about 98%).

During the upgrade of the HERA collider, a new spectrometer system [42] was installed (see Figure 3.13) to cope with the new challenges (larger beam currents and instantaneous luminosity, more pile-up of bremsstrahlung, polarised beam leptons) and trace the electrons produced from $\gamma \to e^+e^-$ conversion.

Sources of systematic uncertainties are the vertical alignment and y-position measurement (2.5%), photon conversion rate (2%), pile-up (0.5%), deadtime measurement (0.5%) and the theoretical Bethe-Heitler cross section (0.5%), which added up to 3.5% in the early operations, but decreased over time. An uncertainty of 2.6% is assumed in this thesis, in accordance with recent ZEUS publications (see e.g. Ref. [43]).

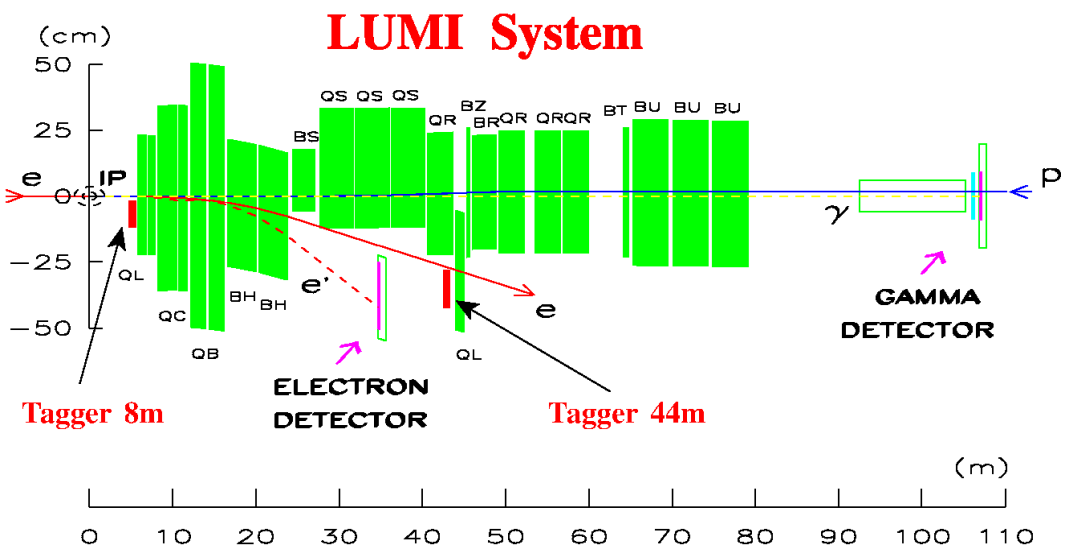

Figure 3.12: Schematic view of the HERA-I ZEUS LUMI monitor system.

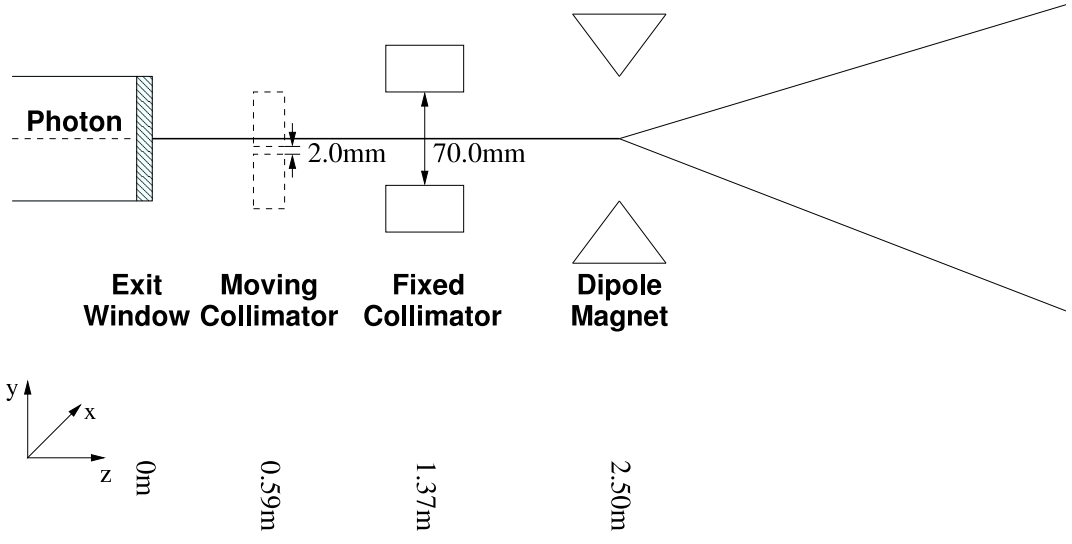

Figure 3.13: Schematic view of the ZEUS luminosity spectrometer.

Chapter 4

Event Reconstruction

The basic event reconstruction is performed by the ZEUS ZEPHYR package.

4.1 Calorimetric Variables

Before precise quantities can be calculated from the energy deposits in the calorimeter, the energies have to be corrected for detector effects. To suppress the noise from the intrinsic radioactivity of the Uranium in the cells, isolated cells with an energy content of less than 80 MeV in the electromagnetic part and 140 MeV in the hadronic part were excluded. Furthermore, noisy cells found during calibration were also excluded.

Inactive material in front of the calorimeter reduces the measurable energy. This effect was compensated by correction factors to the CAL energies, estimated using a map of inactive materials and parametrised as functions of polar and azimuthal angles.

Additionally, the scale of measured energies had to be corrected with factors derived from Monte Carlo simulations.

The total energy of the event, E_{tot}, is the sum of all energy deposits E_i in the calorimeter cells:

$$E_{\text{tot}} = \sum_{i}^{\text{cells}} E_i. \tag{4.1}$$

The total momentum $\vec{p}$ is the same sum weighted with the directions from the reconstructed interaction vertex to the cell centres, given by unit vectors $\vec{r}_i$:

$$\vec{p}_{\text{tot}} = \sum_{i}^{\text{cells}} E_i \vec{r}_i. \tag{4.2}$$

The Cartesian components of $\vec{p}$ in the ZEUS reference coordinate system are called p_x, p_y and p_z. Using this notation the imbalance of the transverse momentum is given by

$$p_T^{\text{miss}} = \sqrt{p_x^2 + p_y^2}. \tag{4.3}$$

The longitudinal energy-momentum imbalance can be expressed as

$$(E - p_z)_{\text{CAL}} = E_{\text{tot}} - p_z = \sum_{i}^{\text{cells}} E_i (1 - \cos\theta_i), \tag{4.4}$$

θ_i being the polar angle of the i-th CAL cell. This quantity is more convenient than just p_z, because the proton remnant usually carried a significant unknown energy fraction down the beam pipe in forward direction. $E - p_z$ is invariant under this effect, because particles moving exactly forward give no contribution.

4.1.1 Clustering

As particles interacting with the calorimeter material shower and deposit their energy usually in more than one cell, the cells which are likely to belong to the same shower of a single particle are clustered.

In a first step, cell islands (local clusters of cells) are formed in each of the different layers (EMC, HAC1, HAC2) and sections of the CAL (FCAL, BCAL, RCAL) separately (see Chapter 3 for the definitions of the calorimeter parts). In this procedure each cell is iteratively connected with the highest energy neighbouring cell until every cell is assigned to a cell island.

In the next step cell islands are combined to cone islands according to probability functions based on the (η, ϕ) separation. These probability functions are derived from single pion Monte Carlo events. The pseudorapidity η is defined as

$$\eta = -\ln\left(\tan\frac{\theta}{2}\right), \tag{4.5}$$

where θ is the polar angle with respect to the proton beam direction.

The matching goes from the outer layers (HAC2) inwards to the inner layers (EMC). During this procedure also different EMC islands and islands from different CAL section are allowed to be connected to each other. A position is assigned to the cluster by the centre of gravity of the cone island, taking into account the energy imbalance of each cell. The cluster energies are corrected for backsplashing effects, inactive material absorption, super-crack energy loss and data-MC discrepancies.

4.2 Vertex and Track Reconstruction

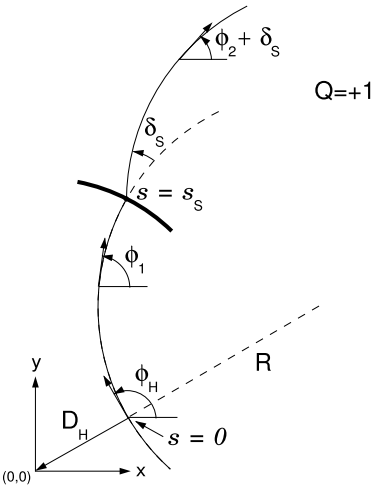

Figure 4.1: Helix parametrisation

Tracks were reconstructed using information from the CTD, the MVD (for the reconstruction of MVD hits and details of the track reconstruction chain refer to Chapter 5) and in the case of forward tracks from the STT. A change between two approaches took place while this analysis was carried out: KFFIT was replaced by RTFIT.

In KFFIT (Kalman Filter Fit, [44]) first a helix curve at a reference point in the (x, y) plane with the five parameters ϕ_H (angle tangent to the helix in the (x, y) plane), Q/R (Q is the charge, R the local radius), QD_H (D_H connects the helix to the reference point), z_H and $\cot\theta$ is fitted to the CTD hits. Then the MVD hits are added with a Kalman filter technique [45] and provide corrections to the helix parameters, yielding a more precise track reconstruction.

In RTFIT (Rigorous Track Fit, [46] all hits (CTD, MVD, STT) are treated basically equal

with only a weight factor to take into account the different resolutions. In this sense a rigorous fit is performed, that takes also inhomogeneities in the forward magnetic field and thus deviations from the helix shape into account.

By extrapolating the tracks, primary and secondary interaction vertices can be determined.

4.3 Jet Reconstruction

Jets are reconstructed with the longitudinally invariant inclusive k_T algorithm [47].

Starting point for the algorithm as used in this thesis is a list of cone islands and an empty list of jets, an iterative clustering procedure is applied to group the islands into jets. For each of the cone islands the algorithm decides if it is merged with another island or added as a separate jet, until the list of islands is empty.

The energy, pseudorapidity and azimuthal angle are then defined as

$$E_T^{\text{jet}} = \sum_i E_{T,i}, \tag{4.6}$$

$$\eta^{\text{jet}} = \sum_i \frac{E_{T,i}\eta_i}{E_{T,i}}, \tag{4.7}$$

$$\phi^{\text{jet}} = \sum_i \frac{E_{T,i}\phi_i}{E_{T,i}}, \tag{4.8}$$

where the index i runs over all cone islands.

4.4 Electron Identification

The key signature of electrons and photons is their electromagnetic shower in the calorimeter, contained mostly in the electromagnetic part. These showers are the result of pair creation, compton scattering, photoelectric effect and bremsstrahlung reactions. A shower stops when electron energies get so low that they lose their remaining energy through ionisation.

To find electrons the electron finder EM [48] was used. Seeds for EM are CAL cells with a local energy maximum. To these cells, surrounding cells with an energy above the noise threshold are clustered. The centre of the cluster and thus the position of the electron candidate is obtained from a logarithmic weighting of the energy deposits.

For further information the algorithm tries to match a track to the cluster by extrapolating all tracks with $p_T^{\text{track}} > 0.1\,\text{GeV}$ to the calorimeter surface. If the distance of closest approach (DCA) is less than 50 cm the matching is successful and the track information is taken into account for the calculation of the electron properties. Else only calorimetric variables are used. For all calculations cell islands with the energy corrections mentioned in Section 4.1 applied are used.

EM uses seven characteristic electron variables (for candidates without a matching track only the first four), that are approximately uncorrelated, and calculates a subprobability $\mathcal{P}_k$ for each:

- the fraction of electromagnetic energy outside the highest energy cell
- the energy fraction of the hadronic section(s),
- the energy fraction in the highest CAL module pair,

- the energy inside a cone of $R = 0.8$ (the cone radius is defined as $R = \sqrt{(\Delta\phi)^2 + (\Delta\eta)^2}$) not associated to the electron candidate,
- $\delta\phi = |\phi_{\text{trk}} - \phi_{\text{cal}}|$,
- $\delta\theta = |\theta_{\text{trk}} - \theta_{\text{cal}}|$,
- $\delta_p = |1/p_{\text{trk}} - 1/E|$.

The $\mathcal{P}_k$ are optimised separately for FCAL, BCAL and RCAL and uniformly distributed between 0 and 1 for real electrons. Fake electrons tend to have larger values for each characteristic variable and receive lower subprobabilities. The product of N subprobabilities $\mathcal{P} = \prod_{i=1}^{N} \mathcal{P}_k$ can be transformed into the variable

$$\mathcal{Q} = \mathcal{P} \sum_{k=1}^{N} \frac{(-\log \mathcal{P})^k}{k!}, \tag{4.9}$$

which again is uniformly distributed between 0 and 1. With this method the calorimeter probability $\mathcal{P}_{\text{CAL}}$ is calculated from the subprobabilities of the first three variables, or the grand probability from all seven subprobabilities.

Electron candidates are only accepted if they fulfil the following requirements:

- $E > 4\,\text{GeV}$,
- $\mathcal{P}_{\text{CAL}} > 10^{-5}$,
- $\mathcal{P}_{\text{trk}}(\delta\phi, \delta\theta, \delta_p) > 10^{-3}$.

Figure 4.2 shows the efficiency of the EM finder as a function of the electron energy, the polar angle and Q^2, compared to the finder Sinistra, which has a slightly worse performance for high electron energies and in the forward region.

4.4.1 Photon Identification

As the shower shape of photons is almost identical to that of electrons, the EM finder is also used to find photons. To distinguish electron candidates from photon candidates, the tracking information is used, exploiting the fact that photons do not leave tracks (cf. 8.2.10).

4.5 Kinematic Variables

According to Equation (2.2) the kinematics of a DIS event are for fixed lepton and proton energies E_e and E_p (and thus fixed centre of mass energy $\sqrt{s}$) defined by only two independent variables of the set x, y, Q^2.

There are different ways to reconstruct these variables from the leptonic and hadronic final state [50], some working only for NC DIS events:

Electron Method: This method is independent of the hadronic system and uses the information energy and the polar angle of the scattered lepton. Therefore it can only be used for NC DIS events. However, the resolution for low y and $\theta' \approx \pi$, where θ', the scattering angle of the electron, is low.

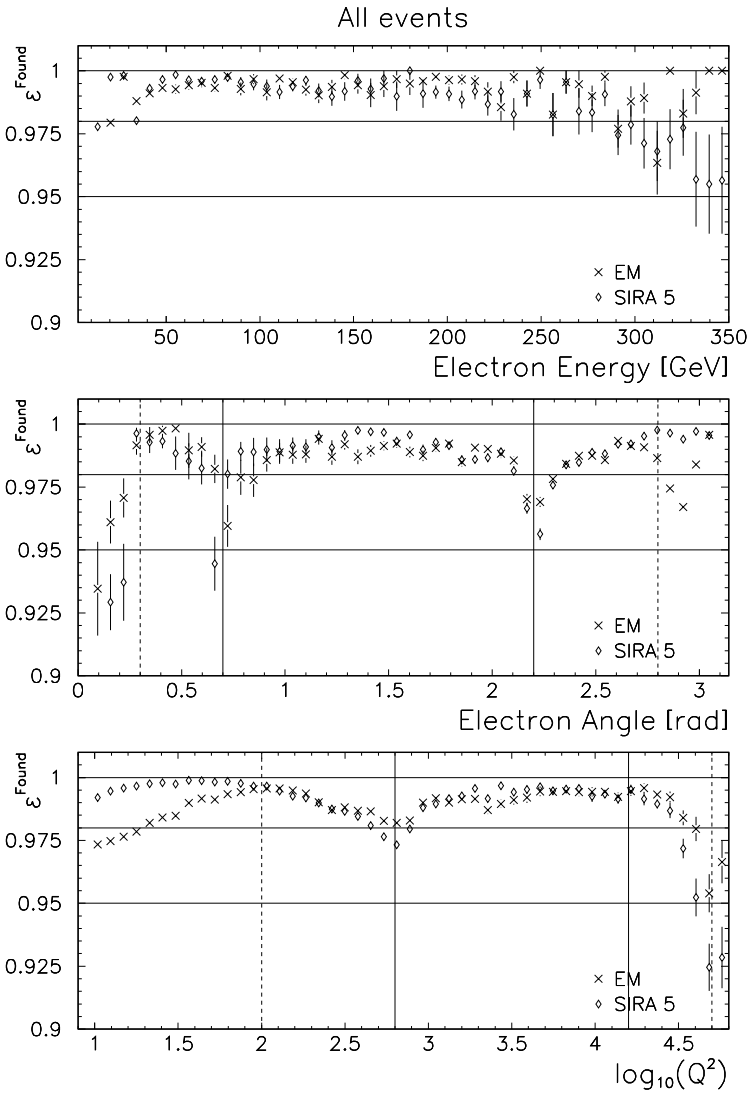

Figure 4.2: Efficiency of the electron finders EM (crosses) and Sinistra (diamonds) as a function of energy (top), polar angle (middle) and Q^2 (bottom) [49]. Vertical lines denote the transition regions between different CAL parts (continuous lines) and the end of the CTD (dashed line).

Jacquet-Blondel Method: This method is independent of the electron reconstruction and initial state radiation, because only the energies and polar angles of the particles belonging to the hadronic final state are used. Consequently, it is highly sensitive to calorimetric energy uncertainties. It can be used both for CC and NC DIS events.

Double Angle Method: In this method only the scattering angles of lepton and hadronic system are used, it is thus independent of the energy scale. As a drawback, it has a bad resolution for small Q^2 and can only be used for NC DIS events.

In this thesis the Jacquet-Blondel method is used, because there appears no scattered lepton in the signal process, and in the main background process the scattered lepton is a neutrino.

The kinematic variables in the Jacquet-Blondel method are expressed as:

$$Q^2 = \frac{p_{T,\mathrm{had}}^2}{1-y}, \tag{4.10}$$

$$y = \frac{\delta_{\mathrm{had}}}{2E_e}, \tag{4.11}$$

$$x = \frac{Q^2}{sy}, \tag{4.12}$$

with

$$\delta_{\mathrm{had}} = \sum_i (E_i - p_{i,z}), \tag{4.13}$$

$$p_{T,\mathrm{had}} = \sqrt{(\sum_i p_{i,x})^2 + (\sum_i p_{i,y})^2}, \tag{4.14}$$

where i runs over all final state hadrons.

The relative errors of the kinematic variables are

$$\frac{\Delta Q^2}{Q^2} = 2\frac{\Delta p_{T,\mathrm{had}}}{p_{T,\mathrm{had}}} + \frac{1}{2E_e}\frac{\Delta\delta_{\mathrm{had}}}{1-y}, \tag{4.15}$$

$$\frac{\Delta y}{y} = \frac{\Delta\delta_{\mathrm{had}}}{2E_e y}, \tag{4.16}$$

$$\frac{\Delta x}{x} = \left(\frac{1}{2E_e(1-y)} - \frac{1}{2E_e y}\right)\Delta\delta_{\mathrm{had}} + 2\frac{\Delta p_{T,\mathrm{had}}}{p_{T,\mathrm{had}}}. \tag{4.17}$$

The errors are divergent for Q^2 and x as $y \to 1$ and for y as $y \to 0$.

4.6 Additional Event Variables

4.6.1 Gravitino

The gravitino $\tilde{G}$ can only be indirectly reconstructed by its missing transverse and longitudinal momentum, assuming no other particle escapes undetected.

The transverse momentum of the gravitino is given by the total negative p_x and p_y in the CAL. The missing p_z can be obtained from the measured global $(E-p_z)_{\mathrm{CAL}}$ (defined in Equation (4.4)).

The true value of $E - p_z$ can easily be calculated from the total energy

$$E = p_{e,z} + p_{p,z}$$

(assuming highly relativistic particles) and the total z-momentum

$$p_z = p_{p,z} + p_{e,z}$$

(where p_e is the electron momentum and p_p the proton momentum) in the initial state, where $p_{p,z} = p_p$ and $p_{e,z} = -p_e$:

$$E - p_z = 2p_e. \tag{4.18}$$

Due to momentum conservation $E - p_z$ will remain the same in the final state.

The difference between the detected $(E-p_z)_{\mathrm{CAL}}$ and the true $E-p_z$ in the signal process is due to the escaping gravitino:

$$E - p_z = (E - p_z)_{\mathrm{CAL}} + (E_{\tilde{G}} - p_{z,\tilde{G}}). \tag{4.19}$$

Under the assumption of a small gravitino mass, the gravitino energy is given by

$$E_{\tilde{G}}^2 = p_{T,\tilde{G}}^2 + p_{z,\tilde{G}}^2. \tag{4.20}$$

Putting all this together, the forward component of the gravitino momentum can be calculated as

$$p_{z,\tilde{G}} = \frac{1}{2}\left(\frac{p_{T,\tilde{G}}^2}{2E_e - (E - p_z)_{\mathrm{CAL}}} - 2E_e - (E - p_z)_{\mathrm{CAL}}\right). \tag{4.21}$$

4.6.2 Neutralino

The neutralino four-momentum in the analysed signal process is the sum of the photon and the gravitino four-momenta:

$$p_{\tilde{\chi}_1^0} = p_\gamma + p_{\tilde{G}}. \tag{4.22}$$

Its mass is

$$m_{\tilde{\chi}_1^0}^2 = (E_\gamma + E_{\tilde{G}}^2)^2 - (\vec{p}_\gamma + \vec{p}_{\tilde{G}})^2 \approx 2E_\gamma E_{\tilde{G}}(1 - \cos\theta), \tag{4.23}$$

where θ is the angle between the two four-vectors.

4.6.3 Selectron Momentum Transfer

The momentum transferred by the exchanged selectron $\tilde{e}$ can be calculated from the difference of the initial lepton, $p_e = (E_e, 0, 0, -E_e)$ for high energies, and the four-vector of the neutralino:

$$\begin{aligned} Q_{\tilde{e}}^2 &= \left(p_e - p_{\tilde{\chi}_1^0}\right)^2 \\ &= E_e(E_{\tilde{\chi}_1^0} - p_{z,\tilde{\chi}_1^0}). \end{aligned} \tag{4.24}$$

Chapter 5

Clustering Procedures for the ZEUS Micro Vertex Detector

5.1 MVD Sensors

The MVD consists of single-sided silicon strip detectors on high ohmic n-type silicon of 300 µm thickness (see Figure 5.1). The strips are of p^+ type. Separated by five passive strips the readout strips are AC-coupled through a SiO_2-Si_3N_4 double layer to Al-strips, which are connected via wire bonds either to a UPILEX film[1] or a glass fan-out.

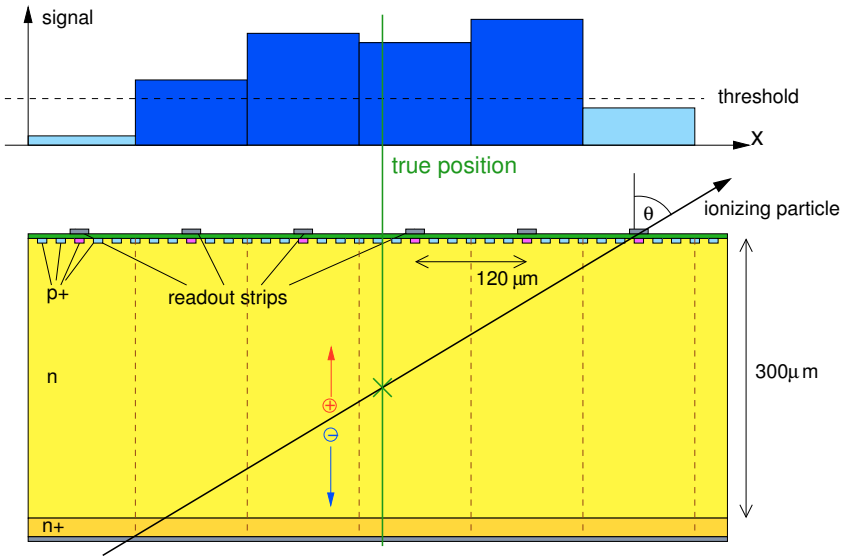

Figure 5.1: Profile of a sensor with associated strip signals for a sample track with large incident angle. Ignoring the energy loss of the traversing particle inside the silicon, it can be assumed that all strips in the inner part have the same signal, varying only due to noise. Only the readout strips at the cluster edge carry meaningful information.

Between each two readout strips with a pitch of 120 µm there are five passive strips, that via capacitive coupling distribute the charge freed by a traversing particle in the silicon to the other passive strips and finally to the readout strips. The readout

[1] UPILEX is a polyimide foil with Cu strips. UPILEX is a registered trademark of UBE Industries LTD., Japan.

is an analogue readout.

5.2 Hit Position Reconstruction and Tracking Chain

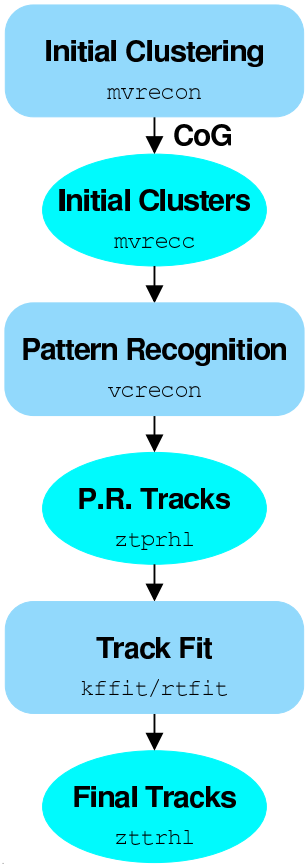

Figure 5.2: Tracking Chain

At the beginning of the ZEUS track reconstruction chain (see Figure 5.2) in ZEPHYR resides the clustering including the cluster position reconstruction, done by the MVRECON package. In the first step, adjacent strips with a signal above a certain strip threshold, that is chosen in a way to suppress noise, are grouped to form a cluster (allowing for single inner strips beneath the threshold), to which a different cluster threshold is applied, mainly to suppress fake hits from delta electrons. The cluster is stored together with the strips at the edge beneath the strip threshold.

To calculate the hit position, the centre of gravity algorithm (CoG) was used until 2007. This algorithm takes all the strip signals S_k in a cluster, ignoring the outermost strips with a signal beneath threshold. The reconstructed position x_{rec} relative to the beginning of the cluster is given by

$$x_{\text{rec}} = \frac{\sum_{k=1}^{n} k S_k P}{\sum_{k=1}^{n} S_k}, \tag{5.1}$$

where P is the readout pitch , $P = 120\,\mu\text{m}$.

The MVD hits are then written to the table of reconstructed MVD clusters (the ADAMO[2] table MVRECC).

This table, together with the hits from CTD and STT, constitutes the input for the pattern recognition phase (done by the VCRECON package). Here, the hits are combined to helix tracks, which are written to a different table (ZTPRHL).

The pattern recognition track table and the tables of the detector hits are afterwards fitted in a more rigorous way (RTFIT package) with the help of sophisticated fitting algorithms and taking into account various corrections. The result is a table of final tracks (ZTTRHL).

In a later step these tracks are subject to vertex reconstruction and higher level analysis.

5.3 Study of Alternative Position Reconstruction Algorithms

Motivated by test beam measurements [51, 52] and earlier studies of detector data [53] which had shown that the CoG algorithm is not the optimal choice for the hit position reconstruction, a study was performed to compare the performance of different alternative algorithms with the aim of implementing the optimal choice into the ZEUS reconstruction software system.

[2] ADAMO is a system for scientific programming based on the Entity- Relationship (ER) model (`http://adamo.web.cern.ch/Adamo/`). It is used in the ZEUS event reconstruction system.

The algorithms that were considered as an alternative to the CoG algorithm can be divided into two classes:

1. Algorithms that need nothing more than the cluster information
2. Algorithms that in addition require some knowledge (e.g. the incident angle) of the track belonging to the hit

Obviously the algorithms of the second class can only be applied after the pattern recognition step, so an algorithm of the first class is needed as a first guess.

5.3.1 Sub-Threshold Centre of Gravity Algorithm

The sub-threshold centre of gravity algorithm is basically identical to the CoG algorithm, with the modification that it uses also the information from up to two strips beneath the strip threshold at the edge of the cluster:

$$x_{\text{rec}} = \frac{\sum_{k=0}^{n+1} k S_k P}{\sum_{k=0}^{n+1} S_k}, \tag{5.2}$$

The main advantage is that it makes use of all the available information for those clusters with only one strip above threshold but two beneath, which otherwise would only be reconstructed with the digital resolution

$$\sigma_{\text{dig}} = P/\sqrt{12} \approx 34.6\,\mu\text{m}.$$

For the same reason the inclusion of sub-threshold strips was also done for all other considered algorithms. Moreover this led to a consistent treatment of all cluster sizes without the need for case differentiations for different widths, especially in the case of the 3-strip algorithm.

5.3.2 3-Strip Algorithm

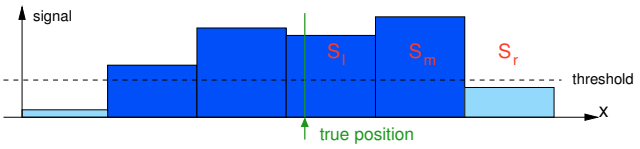

Figure 5.3: Sketch of the 3-strip algorithm.

The 3-strip algorithm focuses on the three strips around the strip with the highest signal S_m in the cluster. In a first step the CoG for this strip and its left (right) neighbour S_l (S_r) is calculated.

In the second step the quadratic, signal-weighted mean of these positions is computed and gives the reconstructed position:

$$x_{\text{rec}} = \frac{p_l S_l^2 + p_r S_r^2}{S_l^2 + S_r^2}, \qquad p_{l/r} = \frac{x_m S_m + (x_m \mp P) S_{r/l}}{S_m + S_{r/l}} \tag{5.3}$$

The 3-strip algorithm can be expected to give good results only for narrow clusters, because for wider clusters the location of the highest signal strip inside the cluster is random.

5.3.3 Head Tail Fusion Algorithm

The head tail fusion (HTF) algorithm explicitly exploits the fact that the signals in the inner part of the cluster are constant with variations only due to noise. Thus the algorithm only takes the two strips at the edges of the clusters into account, and adds sub-threshold strips to them to get S_l and S_r.

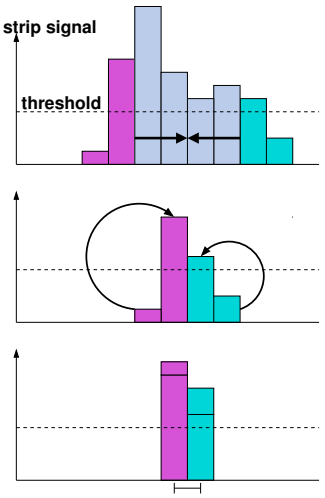

Figure 5.4: Sketch of the head tail fusion (HTF) algorithm.

The reconstructed position lies inside an interval of length P around the centre of the cluster:

$$x_{\text{rec}} = \frac{S_l(x_l + \Delta x) + S_r(x_r - \Delta x)}{S_l + S_r}, \qquad \Delta x = \frac{x_r - x_l + P}{2}, \tag{5.4}$$

where $x_{r/l}$ is the position of the right/left readout strip above threshold.

This head tail fusion algorithm was suggested by Gerd Hartner.[3]

5.3.4 Eta Algorithm

The original Eta algorithm [7] works for two-strip-clusters. Its basic idea is to compensate for non-linearities in the charge distribution.

The quantity η is defined as

$$\eta = \frac{S_r}{S_l + S_r}, \tag{5.5}$$

where $S_{r/l}$ is the signal of the left/right strip.

In this way the CoG algorithm for two-strip clusters corresponds to

$$x_{\text{rec}}^{\text{CoG}} = x_l + \eta P.$$

This would assume a flat η distribution. As the left side of Figure 5.5 shows, the η distribution is in fact not flat.

[3] ZEUS internal tracking group talk at `https://www-zeus.desy.de/zems/ZEUS_ONLY/display.php?p_active=9063`, 16 May 2007.
Note, that the head tail algorithm implemented but never used in MVRECON is different in not restricting the reconstructed position to the small interval around the centre of the cluster. Instead, the reconstructed position is shifted across the hole cluster width according to the ratio of the head and tail strips. This is clearly flawed.

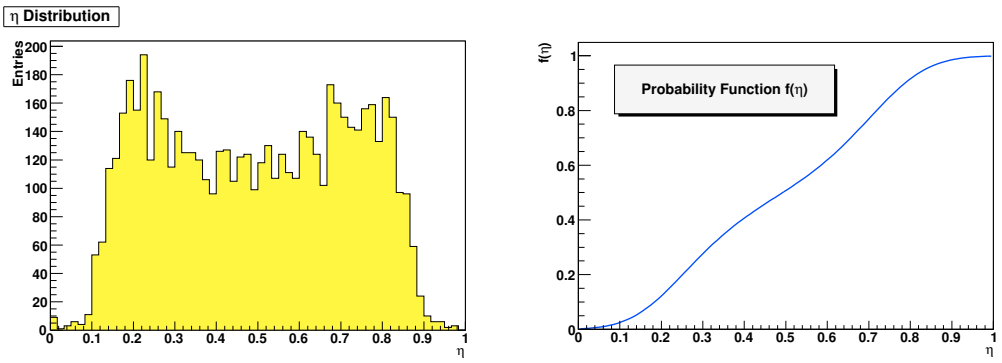

Figure 5.5: Example η and corresponding f distribution.

To compensate for this, one introduces a correcting probability density function $f(\eta)$, so that the reconstructed hit position is

$$x_{\text{rec}}^{\text{CoG}} = x_l + f(\eta)P. \tag{5.6}$$

$f(\eta)$ is calculated by integrating the η distribution:

$$f(\eta) = \frac{1}{N_0}\int_0^{\eta} \frac{\mathrm{d}N}{\mathrm{d}\eta'}\mathrm{d}\eta', \tag{5.7}$$

where $\frac{\mathrm{d}N}{\mathrm{d}\eta'}$ is the differential η distribution and N_0 is the total number of events in the η distribution. This probability function has to be determined before the hit reconstruction, using a large data sample. Note, that this training does not need any knowledge of the true his position. It is purely based on statistics.

When applying this method one has to take into account that the shape of the η distribution changes for different track classes. Most significantly it depends on the incident angle θ (the definition of θ can be found in Section A.1), but there are more factors to be considered, which will be discussed in Section 5.4.

5.3.5 QX (Charge Transfer) Algorithm

The concept of the QX algorithm developed by Gerd Hartner [54] is to take a track candidate from pattern recognition, predict the cluster characteristics,

- the readout strip charges S_i and
- the cluster width w from the track incident angle (see Section A.2),

and match these to the strip data. The model used for this fit is the same as used in the MOZART (see Section 6.4) detector simulation. There, a set of 22 coupling constants c_j is used to transfer charge to each readout strip from the 11 neighbour strips on each side.

Besides the measured signals S_i from the readout strips, the cluster width w estimated from the track angle is input for a fit that, by minimising the quantity

$$\chi^2_{\text{QX}} = \sum_i \frac{1}{\sigma_i^2}\{S_i - s\int_{x_l}^{x_r} dx\rho(x - x_i)\}^2 + \frac{1}{\sigma_w^2}\{W - (x_r - x_l)\}^2 \tag{5.8}$$

in the (x_l, x_r) parameter space, gives the fitted cluster centre $x_m = \frac{1}{2}(X_l + x_r)$ and the fitted cluster width $w = x_r - x_l$.

In Equation (5.8), s is a scale factor for normalisation, and the density function ρ incorporates the coupling constants c_j for the strips.

Seven iterations are done, each of which halves the width of the search steps $\Delta x_{l,r}$, starting at 30 µm and ending at 0.5 µm.

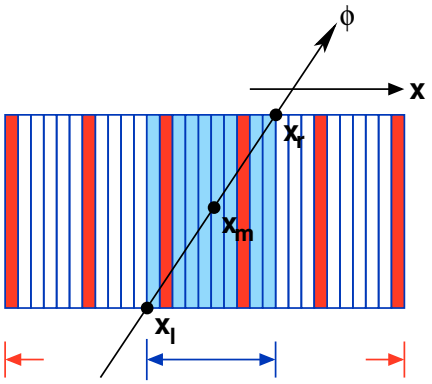

Figure 5.6: Sketch of the QX algorithm.

Because the QX algorithm explicitly uses the track information from the pattern recognition phase, it can correctly handle overlapping clusters (being wider than they should be) and clusters at the edge of a sensor (being narrower than they should be). These effects are taken into account in the QX fitting procedure.

5.4 Eta Algorithm Adaption

In order to apply the Eta algorithm not only to two-strip clusters, as outlined in Section 5.3.4, a method had to be developed to define the quantities S_r and S_l for general clusters.

Two things were changed:

1. Sub-threshold strips are used as well (to include the information carried by them and to reduce the fraction of clusters that consisted of only one strip otherwise).

2. The cluster is split up into two parts of almost equal signal sum, with the condition that the difference between these signals sums is minimal. The reconstructed position lies inside the so called central readout interval between these two halves.[4]

   Figure 5.7 shows a few examples.

Test beam studies [52] had shown that the η distribution depends on

1. The incident angle θ of the track, because this determines the number of strips across which the signal is spread (cf. Section A.2). θ is the angle between the sensor normal and the track, projected onto the plane which is normal to the strips (see Figure A.1).

2. The hit region on the sensor along the strip direction z' (see Figure A.1; $z' = 0$ in the sensor centre). The reason for this is that at certain regions on the

[4] This concept was adopted from ZEUS note ZEUS-99-023 [55].

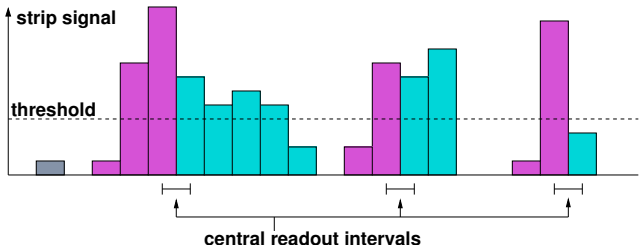

Figure 5.7: A few examples for the splitting into right and left part.

sensor there are additional bond or probe pads (see Figure 5.8), which change the capacitance and thus the capacitive coupling between the strips. The effect on the η distribution is shown in Figure 5.9.

3. The orientation of the sensor. One has to separate Z, $R\phi$ and FMVD sensors, because the geometry, magnetic field, and electrical connection vary for these classes.

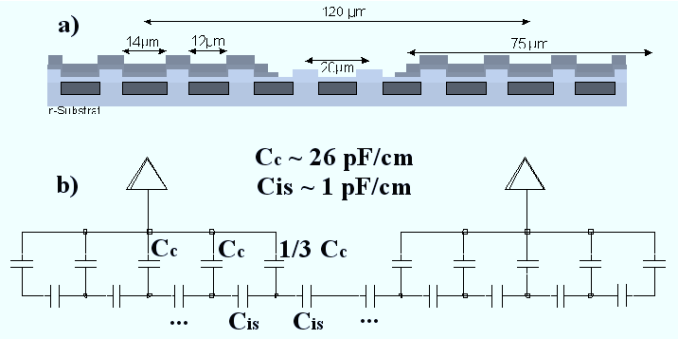

Figure 5.8: Bond region.

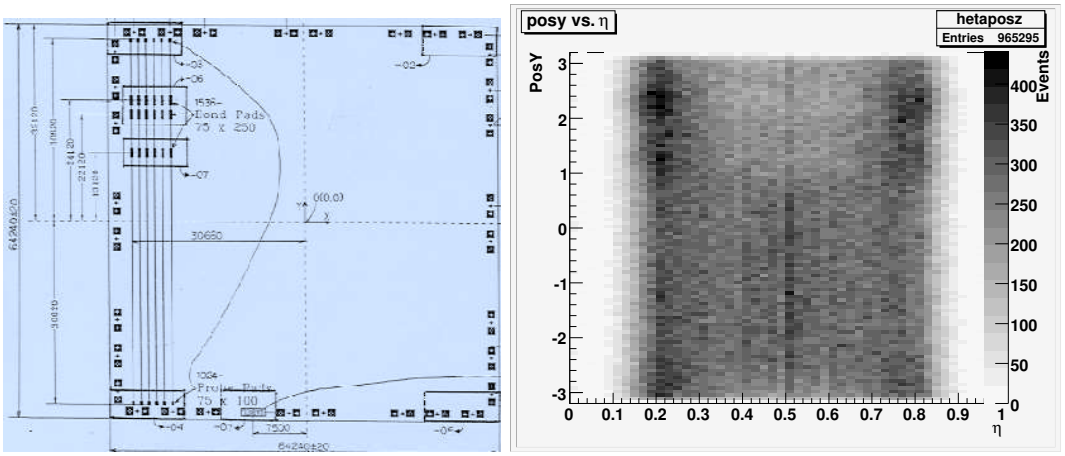

Figure 5.9: Effect of the pads on the η distribution.

The chosen binning in these quantities was a tradeoff between having enough statistics in each bin and covering the relevant significant features of the distributions.

The final tuning was done by means of achieved resolution. Following bins were chosen:

1. 4 bins of $|\theta|$:
   (a) $|\theta| < 20°$
   (b) $20° \leq |\theta| < 40°$
   (c) $40° \leq |\theta| < 60°$
   (d) $60° \leq |\theta|$
2. 4 bins of z':
   (a) $z' < -2.8\,\mathrm{cm}$
   (b) $-2.8\,\mathrm{cm} \leq z' < 0\,\mathrm{cm}$
   (c) $0\,\mathrm{cm} \leq z' < 2.8\,\mathrm{cm}$
   (d) $2.8\,\mathrm{cm} \leq z'$
3. 4 bins of sensor orientation:
   (a) BMVD Z
   (b) BMVD $R\phi$
   (c) FMVD U
   (d) FMVD V

Examples of how the η distribution changes in these bins can be seen in Figure A.3 (different z' bins) and Figure 5.10 (different θ bins). Figure 5.10 shows, that for shallow incident angles the η distribution is completely located around 0.5, so that no significant prediction for the cluster position can be expected in that case.

The histograms that resulted from normalising and integrating the η distributions had to be fitted to get the probability density function $f(\eta)$. This fitting was done to smoothen out fluctuations in the distribution and reduce the amount of data to be stored and used in the algorithm.

Different functions were considered as a fit function. After some tests it was decided to use a modified Fermi function with a fourth degree polynomial in the exponent:

$$f(\eta) = 1 - \frac{1}{1 + \exp(a_0 + a_1\eta + a_2\eta^2 + a_3\eta^3 + a_4\eta^4)} \tag{5.9}$$

This function appeared to be flexible enough to fit the different shapes. An example is shown in Figure 5.11.

5.5 Evaluation

The different position reconstruction algorithms described above were tested and evaluated by analysing residuals and impact parameters.

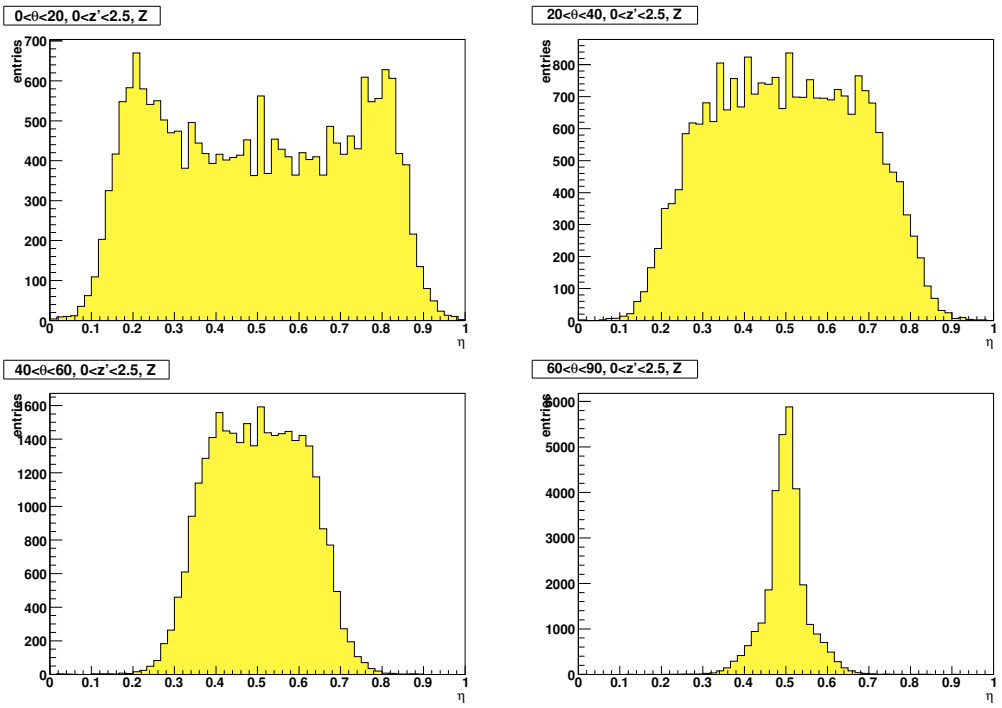

Figure 5.10: η distributions for different incident angles: $0° < \theta < 20°$ (top left), $20° < \theta < 40°$ (top right), $40° < \theta < 60°$ (bottom left), $60° < \theta < 90°$ (bottom left).

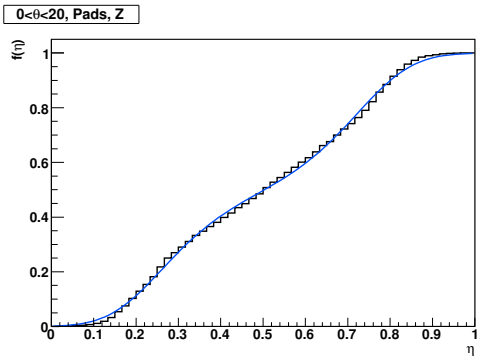

Figure 5.11: Modified Fermi Function fitted to data as a probability density function.

5.5.1 Data Set

For the evaluation a set of data from $e^- p$ collisions recorded in 2006 was used.[5] The analysis was not based on Monte Carlo (except from a few checks for unexpected side effects), because the performance of the different reconstruction algorithms is affected in a subtle way by details of the semi-conductor and readout electronics behaviour. These might not be simulated reliably enough.[6]

For the residual studies the following selection was used:

- Clusters associated to tracks fitted to the primary vertex (with $|z_{\text{vtx}}| < 30\,\text{cm}$), to have well-reconstructed and understood tracks.

[5] Run numbers 59600–59699.

[6] One hint is that the simulation does not reproduce the correct MVD hit resolution.

- In each cylinder at least one Z and one $R\phi$ hit, to make use of the complete MVD and have in most cases enough data points for a reasonable fit of the 5 helix parameters of the tracks.

- Tracks crossing at least CTD super layer 5, to have additional proper information outside of the MVD for cases with insufficient MVD information.

- $p_T > 3\,\text{GeV}$, to ensure that the energy loss and multiple scattering of the particles can be neglected, while still providing enough statistics.

- $|z_H| < 20\,\text{cm}$, to have well understood tracks.

5.5.2 Residuals

Residuals were the primary tool for developing and assessing the different algorithms. The residual is the difference between the position of the cluster on the sensor and the position where the track hits the sensor when it is fitted to all other clusters except this one.

The width of the residual distribution gives a measure for the resolution of a clustering algorithm. In this work the width was calculated by fitting a Gaussian to the distribution.

The different algorithms were tested in a two-stage process.

1. In the first stage a ROOT [56] ntuple was created with the strip signals from every cluster belonging to a track. To obtain unbiased residuals, the evaluated cluster was removed and the track was refitted. For this refitting, a routine (KFFIT, see Section 4.2) of the tracking software was used that provided more interfaces to the user suitable for these tests. The track parameters and inter-/extrapolated hit positions and angles were written to the ntuple. This ntuple could later be analysed effectively offline, to develop, test and compare the different algorithms. The drawback of this method was that the cluster positions that were used for the fit were still the CoG positions, which in principle could introduce systematic errors and give only a pessimistic estimate of the resolution improvement.

2. Therefore, with the matured algorithms a second testing stage was established. Now all the clusters were reclustered using the algorithm under test, before a refit excluding the evaluated cluster was performed. For the refit a newer tracking package (RTFIT) was now available, see Figure 5.12.

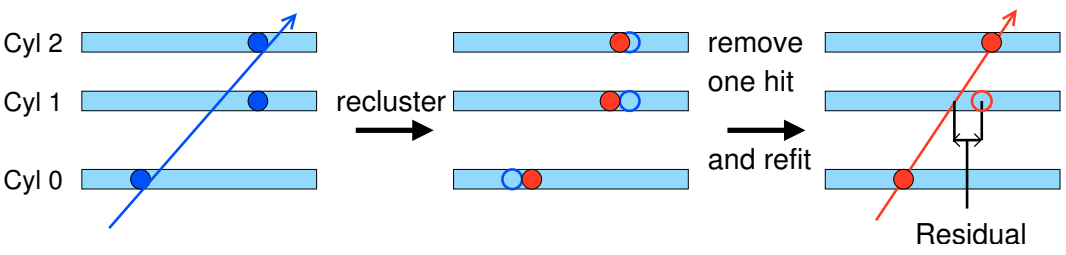

Figure 5.12: More sophisticated residual calculation with elimination of systematic errors.

In the first stage the Eta algorithm as outlined in Section 5.4 was developed, and the other algorithms were tested, with the exception of the QX algorithm, which was developed and made available only later.

The residual distributions for the Eta algorithm (as an example) for different cylinders are plotted in Figure 5.13.

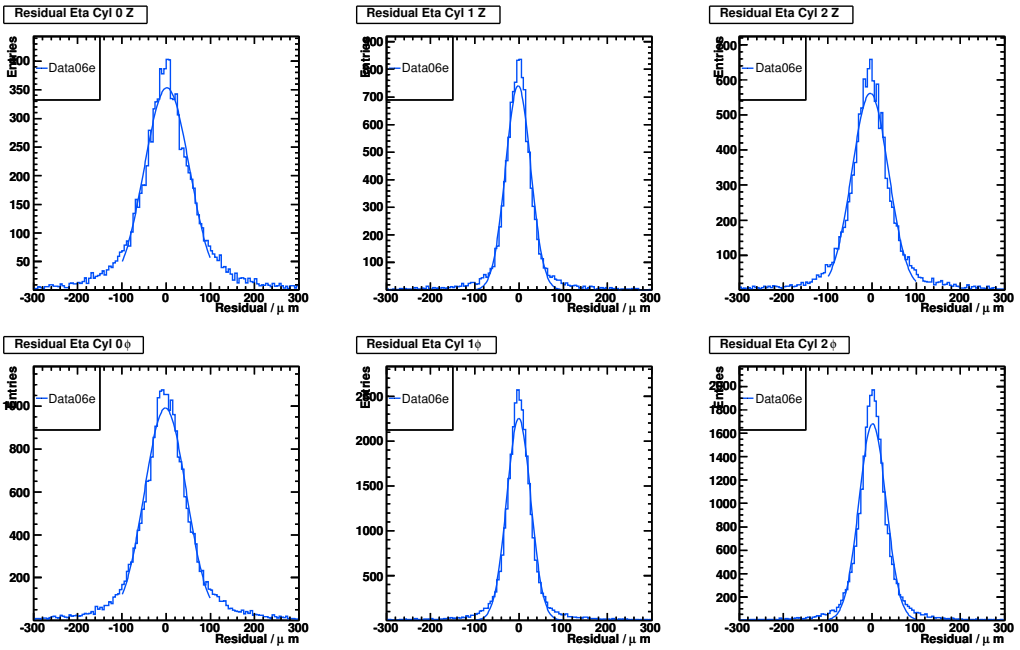

Figure 5.13: Residual distributions for normal incident ($|\theta| < 10°$) for the Eta algorithm, for different cylinders (innermost to outermost from left to right) and different module orientations (top: Z, bottom: $R\phi$).

Figure 5.14 shows the angle dependent residual distribution widths for cylinder 1. The fact that cylinder 1 has a smaller residual distribution width than cylinders 0 and 2 reflects that the width σ of the distributions is not only determined by the intrinsic resolution σ_i of the algorithm, but also by the track error σ_t:[7]

$$\sigma = \sqrt{\sigma_i^2 + \sigma_t^2}. \tag{5.10}$$

The track error σ_t is smaller for cylinder 1, because in that case the track is interpolated between cylinder 0 and 2, while in the other cases an extrapolation is done.

It is clearly visible that the Eta algorithm performs best for small incident angles. For large incident angles the head tail fusion algorithm and the sub-threshold CoG are close together (within errors). In a small intermediate region the 3-strip algorithm shows the best resolution, but as expected gets worse for larger cluster sizes. The usual CoG algorithm performs poorly, the gain by adding sub-threshold strips is substantial.

For stage 2 also the QX algorithm, which was not available before, was integrated into the tests.

[7] Here, the uncertainties are assumed to be uncorrelated and Gaussian. This is not strictly true, but the basic idea remains valid.

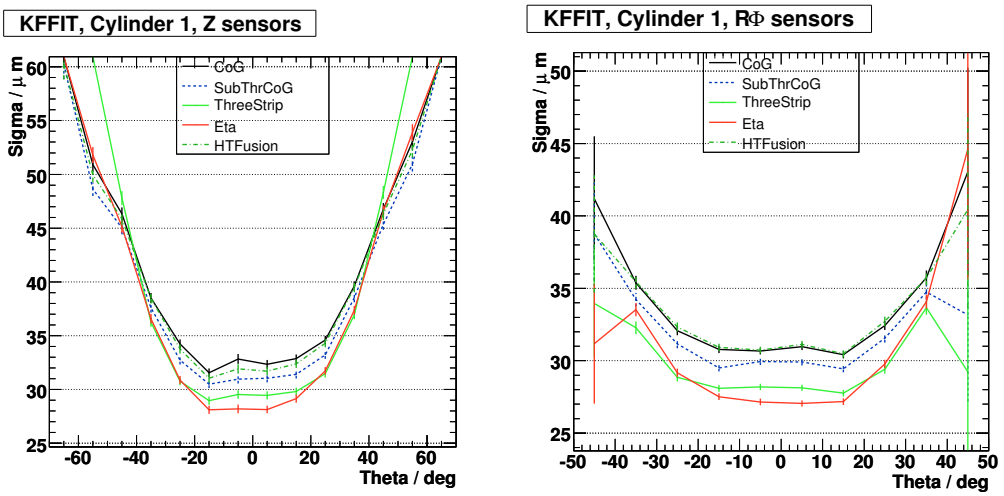

Figure 5.14: Dependence of the width of the residual distribution on the incident angle for different clustering algorithms without reclustering of the hits used for the track refit (KFFIT) for Z sensors (left) and $R\phi$ sensors (right). For shallower incident angles the statistics and thus the fit uncertainties (denoted by the vertical bars) are worse. The incident angles are generally lower for $R\phi$ hits due to geometry.

	Cyl 1 Residuals / μm	
Algorithm	Z Sensors	$R\phi$ Sensors
CoG	32.4 ± 0.5	31.7 ± 0.3
SubThrCoG	30.5 ± 0.3	30.3 ± 0.2
ThreeStrip	27.9 ± 0.3	27.2 ± 0.2
HTF	31.7 ± 0.4	32.2 ± 0.2
Eta	26.4 ± 0.3	26.2 ± 0.2
Eta/QX	26.2 ± 0.3	26.1 ± 0.2
QX	26.7 ± 0.3	26.8 ± 0.2

Table 5.1: Residuals at normal incident for the different algorithms for cylinder 1 (tracks refitted with RTFIT).

Figure 5.15 shows the θ-dependent results for the different algorithms, Table 5.1 summarises the residuals for normal incident angle for cylinder 1 (which has the least track uncertainty). Again for small incident angles the Eta algorithm performs best, while the QX algorithm is close. Still there is a turnover at $\theta = 40°$, beyond which the QX algorithm gives the best resolution. Thus also the combination of Eta algorithm for small incident angles and QX algorithm for shallow angle was used as a candidate. This setup seemed to be the optimum (ignoring the small region where the 3-strip algorithm is slightly superior; the final clustering system should not be too fragmented).

The visible (i.e. with track error included) resolutions for the different cylinders and wheels are plotted in Figure 5.16 for perpendicular incident. Also here the expected structure is spotted: In the cylinders/wheels with the biggest extrapolation contribution the visible resolutions are largest. In all cases the chosen combination of the Eta algorithm and the QX algorithm gives the best results.

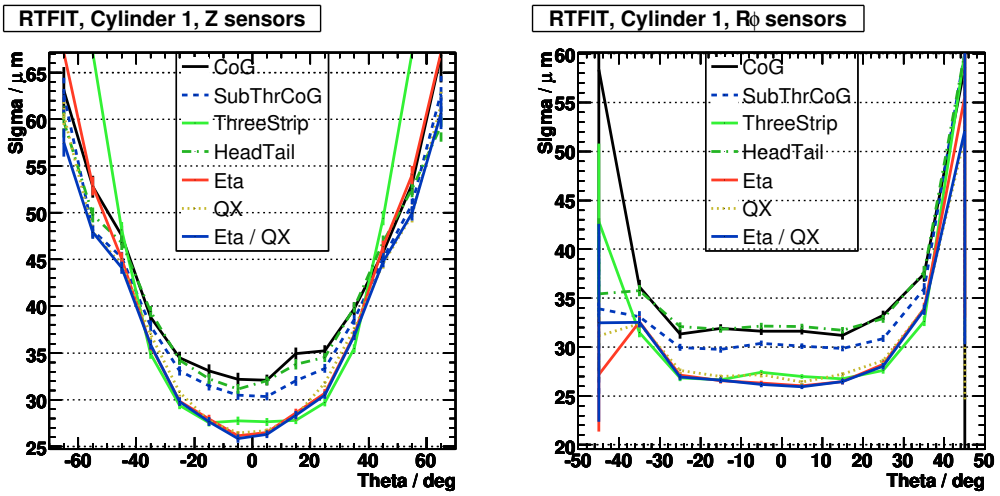

Figure 5.15: Dependence of the width of the residual distribution on the incident angle for different clustering algorithms with reclustering of the hits used for the track refit (RTFIT) for Z sensors (left) and $R\phi$ sensors (right). For shallower incident angles the statistics and thus the fit uncertainties (denoted by the vertical bars) are worse. The incident angles are generally lower for $R\phi$ hits due to geometry.

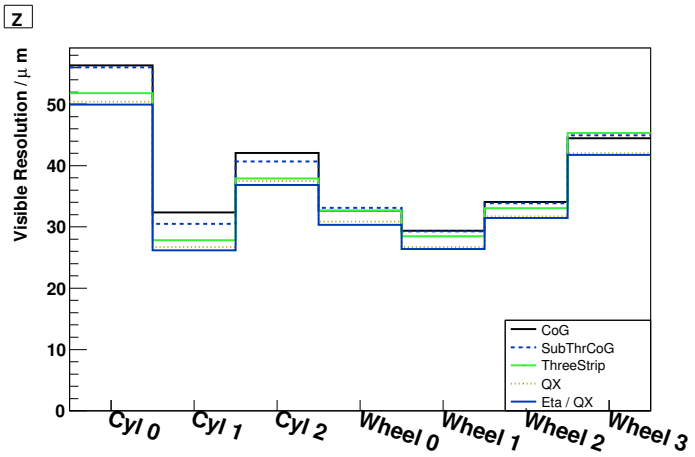

Figure 5.16: Normal incident ($|\theta| < 10°$) residuals for different algorithms and different parts of the MVD (Z sensors only).

5.5.3 Impact Parameters

An independent and more physics related test is to study the distribution of impact parameters or distances of closest approach with respect to the beam-spot mean. The width of this distribution for different azimuthal angles ϕ is determined by the size of the beam-spot in this direction and by the track error for this angular region of the detector. The concept is sketched in Figure 5.17.

The track error contains the error of the individual hits and of multiple scattering effects. Hence it has a large dependence on the transverse momentum,

$$\sigma_d \propto \frac{1}{\sqrt{p_T}}. \tag{5.11}$$

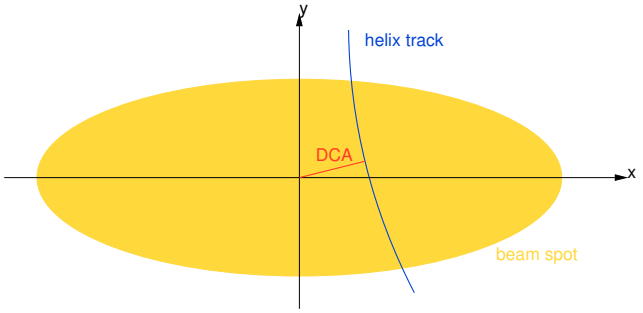

Figure 5.17: The impact parameter is the distance of closest approach (DCA) between the track and the centre of the beam-spot.

To minimise the multiple scattering contribution, only tracks with $p_T > 3\,\mathrm{GeV}$ were selected. Now the width of the impact parameter distribution is a measure for the resolution of the algorithm.

For these parameter studies, the requirement on the number of MVD hits was dropped and replaced by a requirement of at least four MVD hits. By this also the azimuthal regions with only two MVD layers could be charted.

Results for the impact parameter distribution as a function of the azimuthal angle ϕ are shown in Figure 5.18. It shows that the combination of Eta algorithm and QX algorithm yields the best results for most angles.

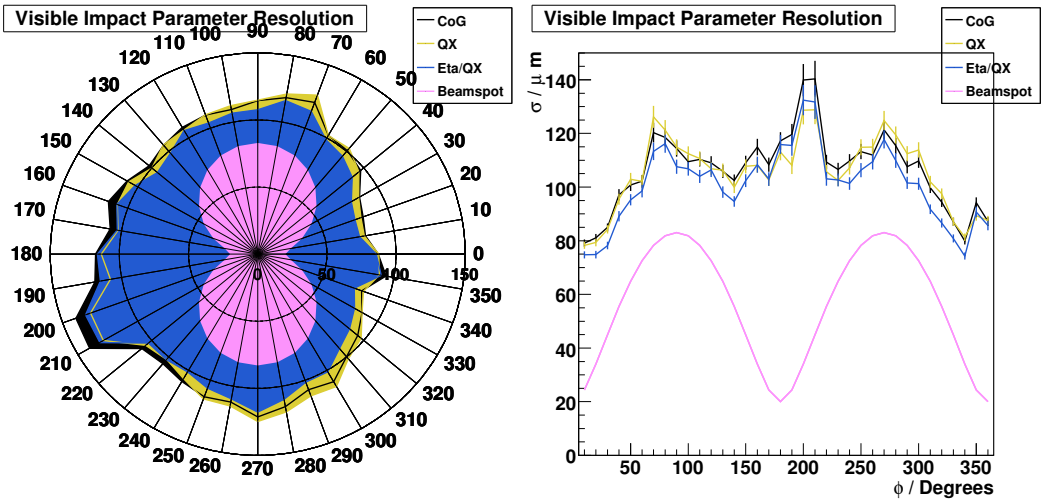

Figure 5.18: Visible impact parameter distribution width. In dusky pink the contribution of the beam-spot is drawn.

The effects of the performance differences is superimposed with

1. the fact that in the left region only two layers of MVD modules are situated;
2. the contribution of the elliptical beam-spot.

Taking into account the fact that the beam-spot width is approximately $b_x = 83\,\mu\mathrm{m}$ in x direction and $b_y = 20\,\mu\mathrm{m}$ in y direction, the beam-spot contribution b can be estimated for a given angle ϕ as

$$b^2 = (b_x \sin(\phi))^2 + (b_y \cos(\phi))^2 \,. \tag{5.12}$$

To eliminate the effect of the beam-spot contribution b has to be quadratically subtracted from the impact parameter distribution width w. This is done in Figure 5.19.

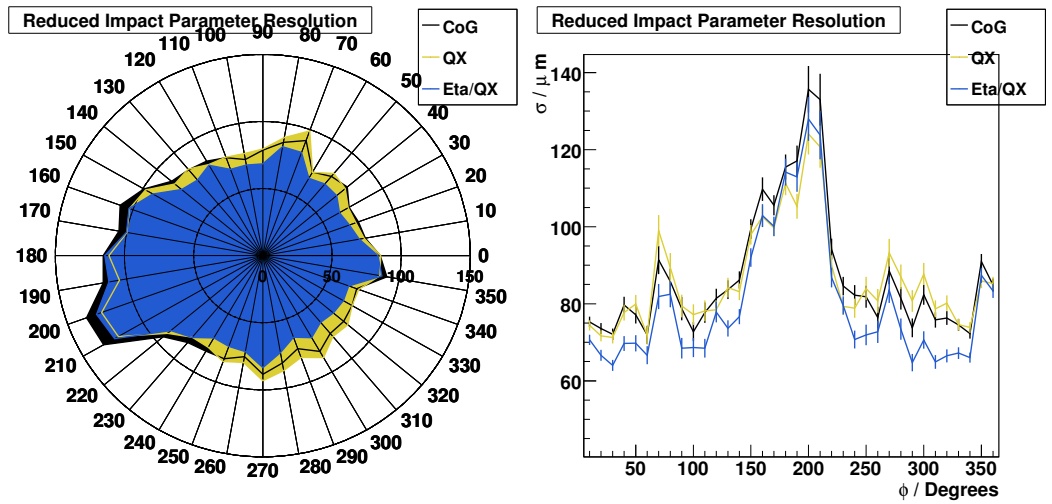

Figure 5.19: Reduced impact parameter distribution width.

In the ideal case this plot should be flat. The reason for it not being flat is the effect of missing modules in the inner cylinder at certain angles (cf. Figure 3.7).

Consequently it is best to look at the region around $\phi = 0°$, which exhibits a good coverage of 3 to 4 modules and a small lever arm. Here, the combination of Eta algorithm and QX algorithm with a reduced impact parameter distribution width of $\sigma_d = 64 \pm 2\,\mu\text{m}$ outperforms the CoG algorithm ($\sigma_d = 73 \pm 2\,\mu\text{m}$) and the QX algorithm ($\sigma_d = 74 \pm 2\,\mu\text{m}$).

The conclusion is that the combination of Eta algorithm and QX algorithm seems to be the optimal choice and should be used to second the previously existing hit reconstruction system.

5.6 New System

Based on the findings in Section 5.5 an improved position reconstruction algorithm was implemented.

5.6.1 Post Pattern Recognition Reclustering

To integrate the new algorithms that use knowledge of the tracks, there had to be additions to the track reconstruction chain after the pattern recognition phase (see Figure 5.20).

Since the QX algorithm was developed and runs as part of the VC package for pattern recognition, it is called from there and produces a new output ADAMO table ZTRECC of reclustered clusters, which can later be used by the track fit. ZTRECC has identical structure to the previously existing table MVRECC of reconstructed MVD clusters, and is referenced by the tables ZTPRUSE of hits used for each track by the pattern recognition package and ZTTRUSE of hits used for each track by the track fit. The reason for introducing this new table is to keep the MVRECC

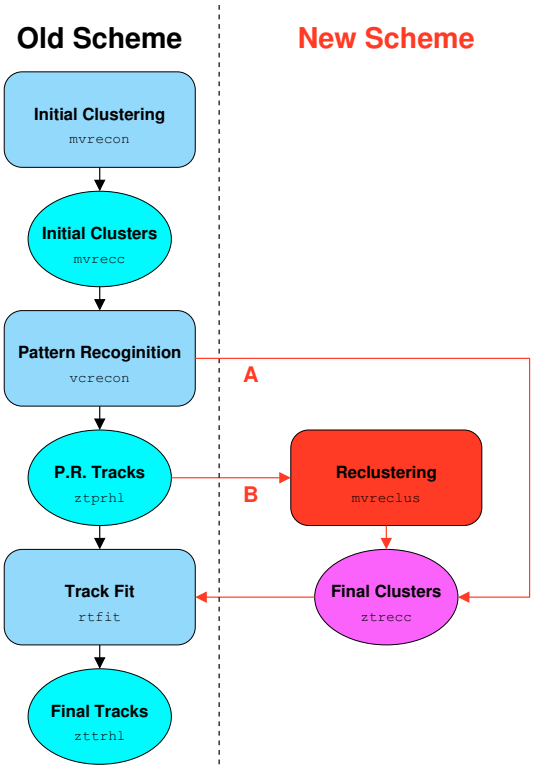

Figure 5.20: The new track reconstruction chain.

information intact and make it possible for the same cluster to be reconstructed differently for different tracks.

The Eta algorithm was implemented in the `mvreclus` routine and requires a new call from the `zrphs1` routine in ZEPHYR between the pattern recognition and the track fit. If the impact angle is less than 40° with respect to the sensor normal, `mvreclus` writes the newly reconstructed clusters to ZTRECC. Else the information from the QX algorithm is kept, because for shallow angles it is more accurate.

5.6.2 Initial Clustering

It was also tested to use algorithms different to the CoG in the initial clustering. Via control cards (see Reference A.4) it is possible to switch on the 3-strip or the head tail fusion algorithm. Nevertheless tests showed that these changes had only a negligible impact on the final performance if the post pattern recognition clustering was switched on. Therefore the CoG remains the default that is used in production.

5.7 Summary

It was shown that the visible clustering resolution can be significantly improved by 20% from 32 µm using the CoG algorithm to 26 µm using a combination of the Eta algorithm for close to normal impact and the QX algorithm for shallow impact. This improvement is also visible in the impact parameter resolution, which improved from 74 µm to 64 µm (beam-spot contribution subtracted) in regions with high module coverage. In particular for high energetic tracks, which are not dominated by multiple

scattering, this is a big improvement.

The new setup with a post pattern-recognition clustering has been successfully implemented into the ZEUS event reconstruction system.

5.8 Outlook

Work could be invested to combine the Eta algorithm and the QX algorithm to one single algorithm. The way in which QX makes use of the track information especially in the cases of overlapping clusters and clusters at the sensor edge is compelling, but the tuning of the coupling constants could be treated in a more systematic way than just inherit it from the detector simulation. Here, the Eta algorithm seems to be superior.

On the other hand, the Eta algorithm could be improved for wide clusters. The splitting in two parts and factoring in of all strips works extremely well for small clusters but is in theory and experiment not convincing for wide clusters. One would expect that mixing the concept of the head tail fusion algorithm with the Eta algorithm would produce better results, but no successful way of doing this has been found yet.

The improved ZEUS tracking system, with the presented framework to reconstruct MVD hit positions as a part, has come to use for the final ("Grand") reprocessing of all HERA II data sets. With important features of a clustering algorithm tuned on real data, alignment from data tracks as well as its rigorous track fit, it sets a standard for future HEP experiments.

Chapter 6

Monte Carlo Simulation

For the understanding of the data and development of signal selection criteria this analysis makes use of the simulation of large numbers of Monte Carlo (MC) events. All the different parts of an event have to be simulated, both for the background processes and for the signal. Finally, the detector response has to be simulated.

6.1 General Event Simulation

6.1.1 Hard Process

The hard process is the part of the event described by Feynman diagrams with the beam lepton and a parton from the proton as initial particles. The parton carries a momentum $q = xp$ (see Sect. 2.2), so that the available centre of mass energy is

$$\hat{s} = xs. \tag{6.1}$$

This establishes a minimum x for the production of heavy particles.

By folding the hard cross section $\hat{\sigma}$ with the parton densities $q_f(x, Q^2)$ one arrives at the total cross section

$$\sigma = \int dt \int_{x_{\min}}^{1} dx \sum_f q_f(x, -t) \frac{d\hat{\sigma}(\hat{s}, t)}{dt}, \tag{6.2}$$

where $t = (q' - q)$ is the transfered momentum.

In this thesis only the Feynman diagrams in leading order (LO) are used for MC simulation, higher orders in perturbation theory are neglected for the hard process and are only factored in as corrections, as described in the following.

6.1.2 QED Radiation

Radiation of initial state photons (ISR) from the incoming lepton lowers its effective energy and shifts the mean of the reconstructed kinematic variables.

Additionally, there is a small contribution from prompt photons from quarks, which changes the cross section slightly.

All these effects are simulated or corrected for in the MC generator programs.

6.1.3 QCD Radiation

Radiation of gluons (in the initial state or in the final state) leads to additional hard jets. To model these effects at the hadron level two different approaches are

commonly used: The Colour Dipole Model and the Matrix Element Plus Parton Shower Model.

Colour Dipole Model (CDM)

If a quark is struck and separated from the proton remnant, according to the CDM [57], these two objects form a colour dipole. By radiation of gluons further colour dipoles are formed ($g \rightarrow q\bar{q}$) in a cascade until a minimal cut-off energy is reached.

Matrix Element Plus Parton Shower Model (MEPS)

In the MEPS model [58] the Altarelli-Parisi splitting functions [59] are used to determine the energy fractions in each branch in the parton shower. The splitting functions are derived by summing up higher orders of perturbation theory to all orders by using the DGLAP leading-log approximation [60]. Quarks and gluons evolve by successive branchings until all partons reach a minimum cut-off energy.

6.1.4 Hadronisation

The merging of the produced coloured partons to form stable colourless hadrons cannot be described perturbatively. There are two important phenomenological models used to describe this process: The Lund Model and the Cluster Hadronisation Model.

Lund Model

The Lund string fragmentation model [61,62] treats the colour field between a quark and an antiquark as a string of constant energy density by taking into account the self-interactions of the gluons. The string energy increases proportional to the growing distance, until it is large enough to create new $q\bar{q}$ pairs. By this process the string splits recursively into smaller parts until the energy of the initial $q\bar{q}$ pair is exhausted.

Cluster Hadronisation

In the cluster hadronisation model [63] colour preconfinement [64] of the quarks in the parton shower is assumed. The gluons are split non-perturbatively into $q\bar{q}$ pairs. In the next step all neighbouring quarks and antiquarks can be combined to low mass colour singlet clusters, which decay isotropically into hadrons by momentum exchange with the neighbouring clusters, taking into account the available phase space.

6.2 Background Simulation

For the simulation of background NC and CC processes DJANGO [65] was used as event generator with HERACLES [66] modelling the initial and final state QED radiation. The QCD radiation was modelled with the CDM as implemented in ARIADNE [57]. For proton PDFs CTEQ5D [67] was used.

6.3 Signal Simulation

For most parts the event generator SUSYGEN [68] with some modifications was used to simulate the signal events. It can simulate $2 \to 2$ SUSY production processes for ep interactions in the R-parity violating MSSM, as well as sparticle decays in two- and three-body processes from the exact first order matrix elements, taking into account s-, t- and u-channel contributions. The mass spectrum of the GMSB model is implemented via an interface to the SuSpect [69] program. Initial state radiation from the beam electron is modelled using the Weizsäcker-Williams approximation [70]. QCD radiation is treated in the MEPS approach and parton densities of CTEQ5M are used. For the hadronisation SUSYGEN was interfaced to Pythia [62] in this thesis, treating the gravitino as a neutrino. Pythia uses the Lund string model.

Some studies were performed using CalcHEP [71].

6.4 Detector Simulation

After their generation the events were passed to the detector simulation program MOZART. MOZART, which is based on the GEANT [72] package, simulates the response of the different detector components, taking into account the ZEUS geometry and interaction with inactive material, which results in energy loss and multiple scattering. The model in MOZART, based initially on geometry and testbeam data, was continuously improved by studies of the running ZEUS experiment. The output of MOZART is passed to the trigger simulation program ZGANA. Accepted events are finally reconstructed with ZEPHYR, which is likewise used to reconstruct the real data events.

Chapter 7

Gravitino Production at HERA

This chapter discusses the signal process for this analysis, $ep \to \tilde{\chi}^0 qX \to \tilde{G}\gamma qX$. Previous analyses can be found in Reference [4, 73].

7.1 Signal Process

For this analysis a GMSB scenario with a neutralino NLSP and R-parity violation was assumed. The Feynman diagram for the investigated process is shown in Figure 7.1. By $\tilde{e}$ exchange between the incoming lepton and a quark from the proton via an R-parity violating coupling λ', a neutralino $\tilde{\chi}^0$ is produced.

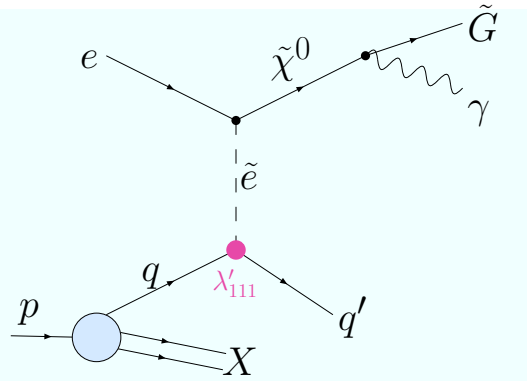

Figure 7.1: Feynman diagram for the signal process. The neutralino decays dominantly into a photon γ and a gravitino $\tilde{G}$.

Being the NLSP the neutralino decays dominantly into a gravitino $\tilde{G}$ and a photon.[1] The signature of the process is

- an isolated high-energetic photon,
- a jet
- and missing transverse energy.

Figure 7.2 shows a typical event display for a SUSY candidate from e^+p data.

[1] There are other signatures when the neutralino undergoes a 3-body decay via an R-parity violating coupling, but those involve heavy virtual sleptons and are suppressed, as long as the neutralino is the NLSP. Decays $\tilde{\chi}^0 \to Z^0\tilde{G}$ are also possible, but suppressed, because the neutralino is photino-like, except for cases with large N and small M_{mess} and Λ [29].

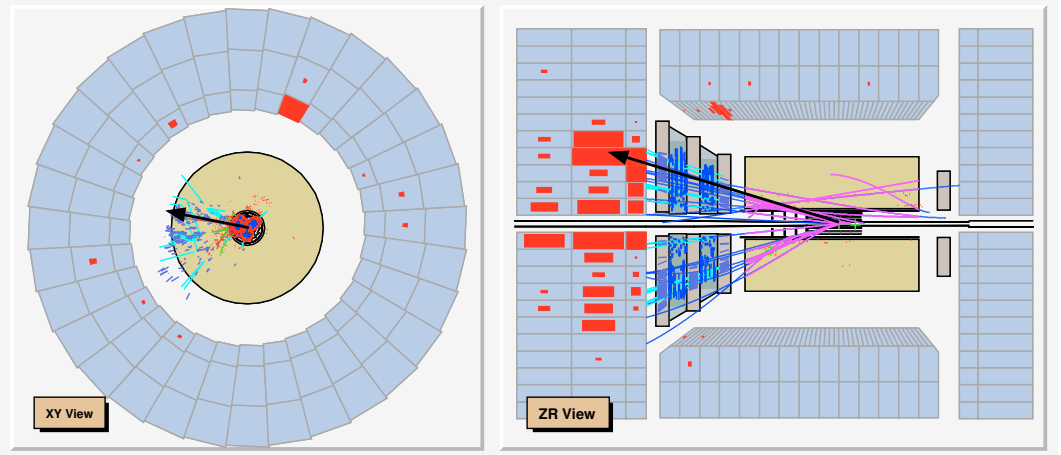

Figure 7.2: Event display for a SUSY candidate. ($Q^2 = 9.9 \cdot 10^3\,\mathrm{GeV}^2, x = 0.25, y = 0.44, E_\gamma = 39\,\mathrm{GeV}, p_T^{\mathrm{miss}} = 74.6\,\mathrm{GeV}$)

7.1.1 Standard Model Background

From the signature of the signal process it is clear that the main background is CC DIS, with an additional photon from initial state radiation or from the quark.

Another source of possible background are NC DIS events, where the energy is mismeasured resulting in missing transverse energy. A false photon may then be due to an electron, for which the track is not reconstructed, or a real photon might be emitted from the initial or the final state electron, or be created during hadronisation and decay.

Furthermore, photoproduction events, where the beam lepton emits a quasi-real ($Q^2 \approx 0$) photon, which interacts directly or via pair production of quarks (resolved photoproduction) with a parton from the proton, can be falsely identified as a signal, when the energy is mismeasured and a false photon is present (e.g. the scattered beam lepton without a properly reconstructed track).

7.1.2 Cross Section and Branching Ratio

The cross section for this process (Figure 7.3) depends mainly on the masses of the selectron and of the lightest neutralino and falls off steeply with increasing masses. For the reference point ($m_{\tilde{\chi}^0} = 96\,\mathrm{GeV}$, $m_{\tilde{e}} = 140\,\mathrm{GeV}$) its value is $\sigma^{e^+p} = 0.14\,\mathrm{pb}$ for the e^+p initial state and $\sigma^{e^-p} = 0.34\,\mathrm{pb}$ for e^-p.

In addition, if the selectron mass is lighter than the neutralino mass and the selectron is thus the NLSP, the branching ratio for the $\gamma\tilde{G}$ channel (see also Figure 7.3) diminishes drastically, since the predominant neutralino decay is then via the slepton. For the reference point, the branching ratio for $\tilde{\chi^0} \to \tilde{G}\gamma$ is 99.7%.

The GMSB parameters used for the mass scan in Figure 7.3 are discussed in Section 7.4.

7.2 Search Strategy

The search strategy in this analysis is to eliminate essentially all the NC background by a high cut on the missing transverse momentum and by selecting only events

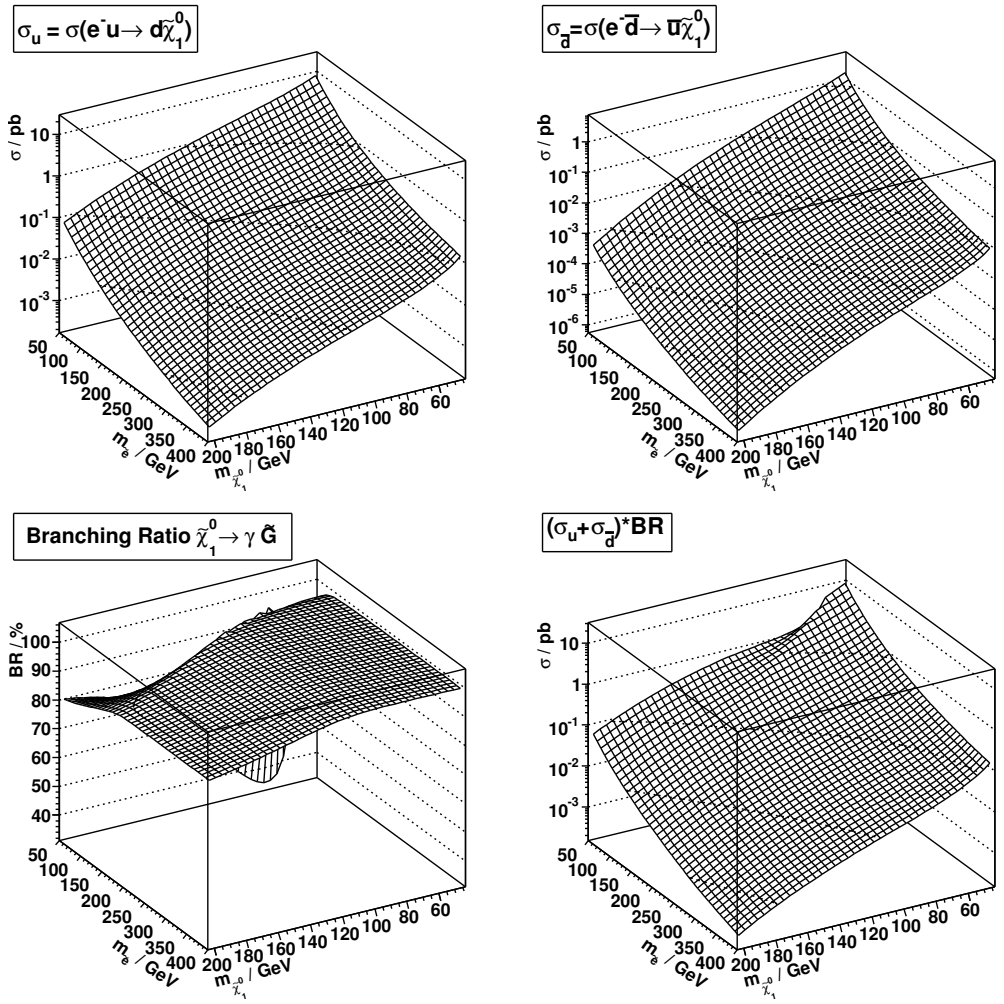

Figure 7.3: Cross section for the $e^- p \to q\tilde{\chi}^0$ channel, and branching ratio for the $\tilde{\chi}^0 \to \gamma\tilde{G}$ decay, assuming $\lambda'_{111} = 1$.

were the photon candidate and the jet are not back-to-back (which is the case for the electron and the jet in LO NC, due to momentum conservation).

The high p_T cut at the same time eliminates the photoproduction background.

It remains to reject events coming not from ep interactions, like cosmic muons, halo muons and beam-gas events. The details are given in Chapter 8.

The event selection aims at a high signal efficiency, at the cost of a higher background. In a second step a multi-variate method is used to discriminate the signal from the background events. After the training of the discriminant , it is applied on data and Monte Carlo with the photon restricted much more. This way the signal-to-background ratio is optimised, before limits on the SUSY masses are derived.

7.3 Previous Limits on GMSB Masses

The GMSB model is frequently considered as "non-canonical" [74], especially in combination with R-parity violation. The process under investigation does only rely on the gravitino mass, the neutralino mass and the selectron mass, which is here assumed to be independent of the other slepton masses. Therefore, virtually no

experimental constraints applicable to this channel exist.

There are generic searches from the LEP experiments, which, however, assume R-parity conservation.[2] The lower limit for the selectron is $m_{\tilde{e}_R} > 73\,\text{GeV}$ [75], the limit for the lightest neutralino is $m_{\tilde{\chi}_1^0} > 47\,\text{GeV}$ [76]. Assuming a GMSB model with a neutralino NLSP, the neutralino limit improves a little bit: $m_{\tilde{\chi}_1^0} > 54\,\text{GeV}$ [77]. In the channels $e^+e^- \to \tilde{G}\tilde{\chi}_1^0 \to \tilde{G}\tilde{G}\gamma$ and $e^+e^- \to \tilde{\chi}_1^0\tilde{\chi}_1^0 \to \tilde{G}\gamma\tilde{G}\gamma$ the limit depends on the selectron mass (due to the possibility of t-channel selectron exchange in the production mechanism), and for low selectron masses ($m_{\tilde{e}_R} \lesssim 200\,\text{GeV}$), the limit touches the 100 GeV mark, see Figure 7.4 [78].

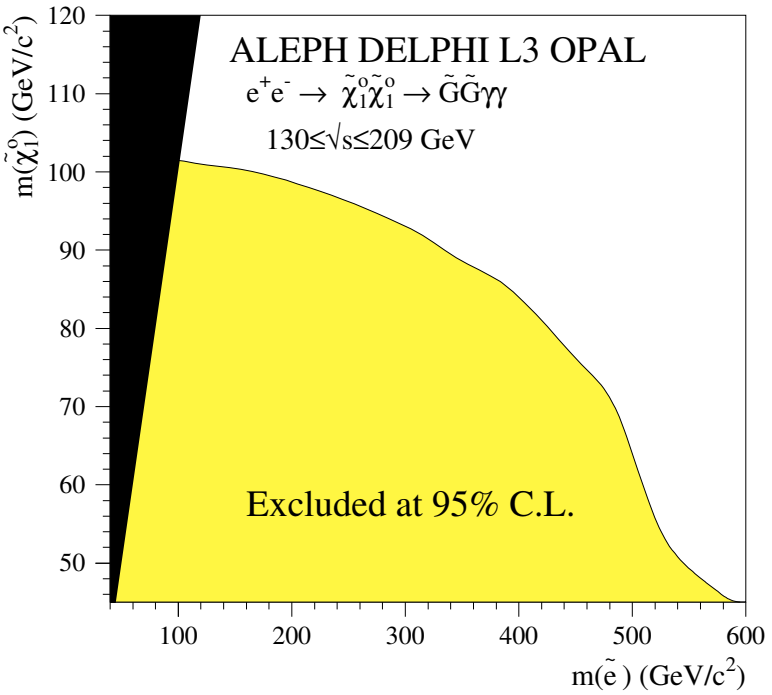

Figure 7.4: LEP exclusion limits in the neutralino/selectron mass plane for a gravitino LSP, assuming R-parity conservation [78].

Other limits come from the Tevatron. The CDF collaboration has derived a lower limit $\sqrt{F} > 221\,\text{GeV}$ [79], equivalently $m_{\tilde{G}} > 1.17 \cdot 10^{-5}\,\text{eV}$.

The DØ experiment has excluded neutralino masses below 125 GeV [80] for the parameter slope $M_{\text{mess}}/\Lambda = 2$, $N = 1$, $\tan\beta = 15$, $\mu > 0$ ("Snowmass Slope SPS 8", [81]). However, these limits are not independent of squark masses and have at best only restricted relevance for the channel under investigation here, which is independent of squark masses.

The H1 experiment at HERA has searched for the same signature as this work, but using only an integrated luminosity of $64\,\text{pb}^{-}1$ [82]. They can exclude R-parity violating couplings of electromagnetic strength for selectron and neutralino masses close to 55 GeV.

[2] Limits on the R-parity violating coupling have been discussed in Section 2.3.5.

7.4 Choice of Reference GMSB Parameters

In addition to the usual GMSB parameters listed in table 2.3, the selectron mass was treated as an extra free parameter.[3] A further free parameter comes into play via the R-parity violating coupling, e.g. λ'_{111}.

To reduce the number of free parameters to a manageable quantity, some of the GMSB parameters were fixed in this analysis:

- $\sqrt{F} = 230\,\mathrm{GeV}$,
- $\tan\beta = 2$,
- $\mathrm{sgn}\,\mu = -1$,
- $N = 1$,
- $M_{\mathrm{mess}}/\Lambda = 2$.

The value of Λ directly determines the mass of the lightest neutralino $m_{\tilde{\chi}_1^0}$. The relation is shown in Figure 7.5.

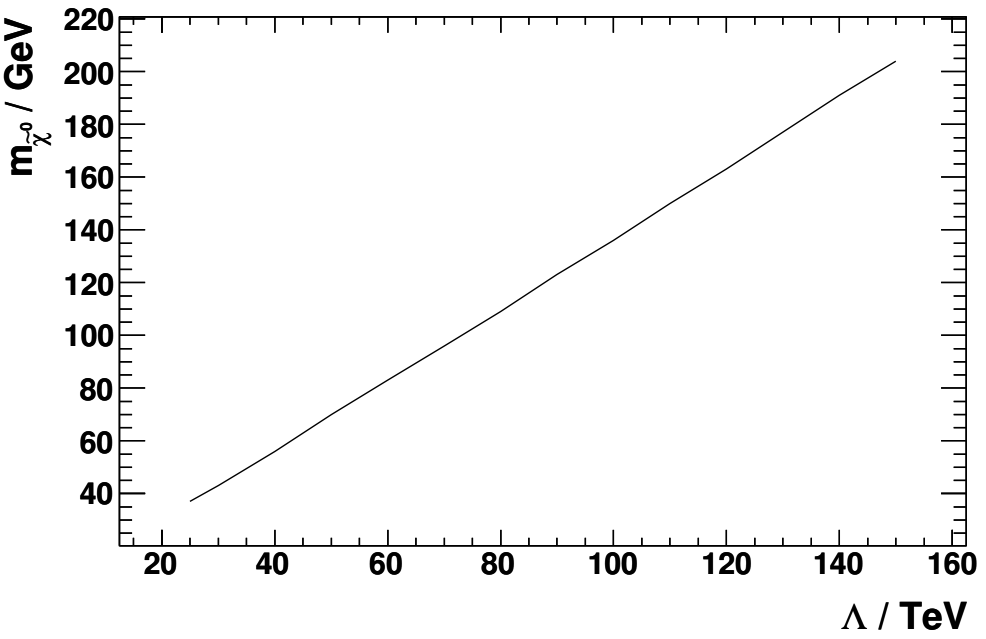

Figure 7.5: Relation between Λ and the neutralino mass $m_{\tilde{\chi}_1^0}$.

When nothing else is mentioned, $\lambda'_{111} = 1$ is assumed. The impact of other values is simple: the total production cross section scales with $(\lambda'_{111})^2$.

[3] This is a deviation from the usual GMSB, but there is no fundamental reason that forbids this.

Chapter 8

Event Selection

8.1 Data Sets

8.1.1 Data

This analysis uses the complete HERA II data sets recorded with the ZEUS detector in years 2003 to 2007 with a total integrated luminosity of $\mathcal{L} = 325\,\mathrm{pb}^{-1}$ (for details see Table 8.1). Runs with insufficient MVD or polarisation information were excluded.

8.1.2 Monte Carlo

The generators used for the production of Monte Carlo background and signal samples were described in Sections 6.2 and 6.3.

In total $5.3 \cdot 10^5$ CC DIS events were generated for the background simulation. To accurately cover the whole kinematic plane, samples with different lower Q^2 cuts of $100\,\mathrm{GeV}^2$, $5000\,\mathrm{GeV}^2$, $10\,000\,\mathrm{GeV}^2$ and $20\,000\,\mathrm{GeV}^2$ were combined and weighted according to the luminosity described by them in relation to the the data luminosity.

Studies with NC DIS and photoproduction MC samples[1] showed, that those events are almost[2] completely rejected by the used set of cuts (which is described in

[1] The NC DIS sample corresponds to an integrated luminosity exceeding that of the data by a factor $6.6 \cdot 10^3$. The photoproduction samples (both resolved and direct) are roughly equivalent to the data luminosity.

[2] In the direct photoproduction MC sample only 2 events were selected, which are outside the signal region. In the NC DIS MC sample no events were selected.

Data set	Lepton Beam	Polarisation	Luminosity / pb^{-1}
2003/04 right handed	e^+	32.5%	21.2
2003/04 left handed	e^+	−38.4%	16.7
2004/05 right handed	e^-	31.8%	45.0
2004/05 left handed	e^-	−26.9%	87.0
2006 right handed	e^-	26.9%	34.3
2006 left handed	e^-	−25.7%	18.9
2006/07 right handed	e^+	31.8%	81.5
2006/07 left handed	e^+	−36.0%	59.0

Table 8.1: Used HERA data sets with lepton beam type and polarisation and integrated luminosity.

Section 8.2). Because of this, and to simplify the treatment, they are normally not explicitly quoted throughout this thesis.

For the signal samples, $2 \cdot 10^4$ SUSY events were generated per point in the GMSB parameter space.

8.2 Selection

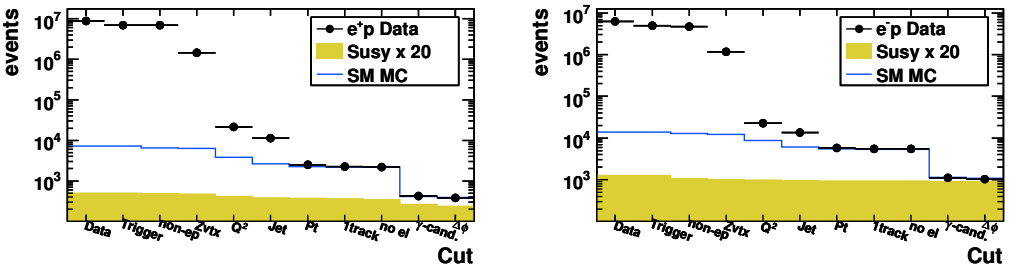

Figure 8.1: Cut flow; left: e^+p, right: e^-p data. To simplify matter, the cuts are grouped: Data combines the cuts that are only applied to data (like timing cuts or manual rejection), Trigger sums up the trigger selection, non-ep pools the cuts against beam gas and halo muons, Zvtx is the cut on the vertex position, Q^2 is the kinematic selection, Jet the jet requirement, the rejection of events without tracks is denoted as 1track, that of events with an high-energetic electron is no el, and the requirement of a photon candidate and its angle to the jet are γ-cand and $\Delta\phi$. After all cuts, a reasonable agreement between data and Monte Carlo is reached.

8.2.1 Jet Requirement

Significant for the SUSY signal is a high energetic jet from the R-parity violating vertex. The leading jet is required to have

$$p_T^{\text{jet}} > 10\,\text{GeV} \qquad \text{and} \qquad -1.5 < \eta^{\text{jet}} < 2.5. \tag{8.1}$$

The distributions of different jet-related quantities are shown in Figure 8.2. There and in all other plots the Monte Carlo SM distributions are normalised to the data luminosity, while the signal distribution is scaled up to make it better visible.

The jet quantities are reasonably described by the SM Monte Carlo; only the η distributions show some slight distributions. In the e^-p data case the region $\eta \approx 1.2$ is below the expectation, which could hint to a detector effect in the crack region between the BCAL and the FCAL. However, in the e^+p data case this region shows perfect agreement, while the next two bins are below the expectation. Here the e^-p data agree with the SM Monte Carlo. This suggests that the effect can be attributed to statistical fluctuations.

8.2.2 Tracks and Vertex

Some cuts that require tracks are only reliable when the hadronic system is inside the CTD acceptance and not too forward, i.e. $\gamma_0 > 0.4\,\text{rad}$. γ_0 is the hadronic angle assuming the nominal vertex position, $Z_{\text{vtx}} = 0$. For these high-γ_0 events a vertex position

$$|Z_{\text{vtx}}| < 30\,\text{cm} \tag{8.2}$$

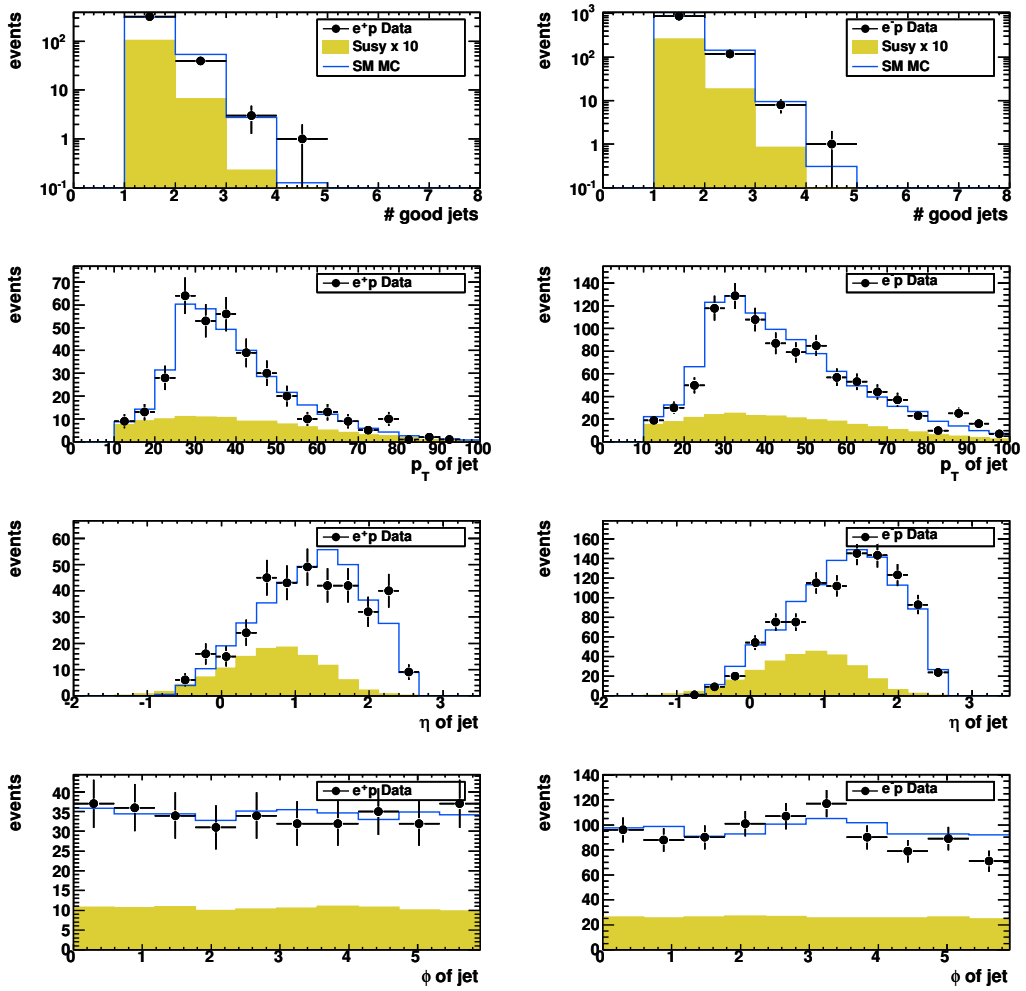

Figure 8.2: Distributions of the number of good jets, transverse momentum, pseudo-rapidity and azimuthal angle of the leading jet, on the left for e^+p data, on the right for e^-p data. The Monte Carlo distributions are normalised to the data luminosity. The background MC distributions (continuous line) are weighted to the data polarisation, the signal MC distributions (filled area) are scaled with a factor 5 to enhance their visibility. All errors are statistical uncertainties on the data (black dots) only, all distributions are after the final selection.

is required to reject events like beam gas, cosmic muons and halo muons not coming from ep collisions, or events from satellite bunches which are reconstructed unreliably. Events from ep collisions have a vertex around $Z_{\text{vtx}} = 0$ with a standard deviation $\sigma = 11\,\text{cm}$.

Furthermore one good track is required. Good tracks originate in the primary vertex, cross the innermost super-layer of the CTD and at least three of the outer super-layers, and have a transverse momentum

$$p_T^{\text{trk}} > 0.2\,\text{GeV}. \tag{8.3}$$

Additionally, to remove beam gas events, which have a high number of poor tracks, the following requirement based on background studies is imposed on the number of

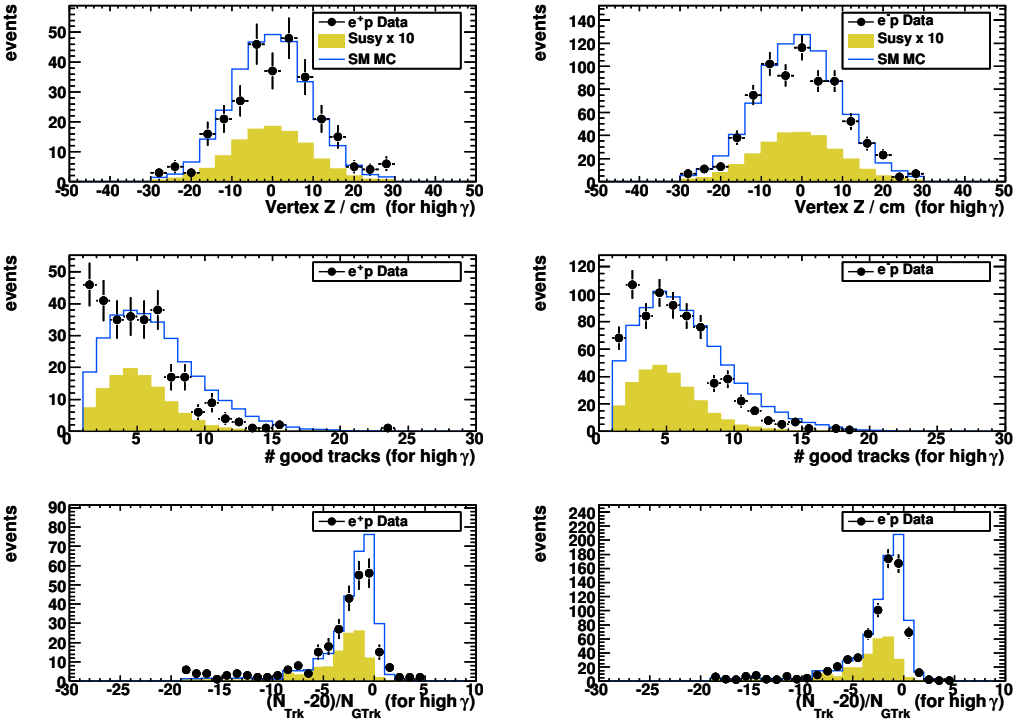

Figure 8.3: Vertex z-position, number of good tracks and relation of number of tracks to number of good tracks (for beam gas rejection). All three distributions are plotted only for events with $\gamma_0 > 0.4$.

tracks N_{trk} and on the number of good tracks $N_{\mathrm{trk}}^{\mathrm{good}}$:

$$\frac{N_{\mathrm{trk}} - 20}{N_{\mathrm{trk}}^{\mathrm{good}}} < 4. \tag{8.4}$$

The distributions of these quantities are shown in Figure 8.3.

The vertex position distributions show fluctuations in single bins, without exhibiting a systematic deviation from the expectation.

Clearly the number of good tracks are not perfectly described by the Monte Carlo. The expected track multiplicity is higher than the measured one. However, being sensitive to details in the tracking, this quantity is always hard to simulate. As a consequence, only a very low cut of at least one good track is made, where only few signal events are located.

Similar arguments can be made for the distribution of the ratio of good tracks to all tracks, which deviates from the expectation around the peak. The cut is far enough away from the peak and the signal to not disturb the results of this analysis.

8.2.3 Kinematic Region

The analysis is restricted to the region with high Q^2, where we have relatively clean DIS samples and the CC cross section (cf. Equation (2.3)) is low enough to not completely hide any small signal. Furthermore, SUSY events should contain high masses and would also appear at high Q^2.

In accordance with an earlier SUSY analysis [4] and to suppress various sources of background (e.g. photo-production) only events with

$$Q^2_{\mathrm{jb}} > 700\,\mathrm{GeV}^2 \tag{8.5}$$

were selected.

The distribution of Q^2 and the other kinematic variables is shown in Figure 8.4. They all agree with the expectation.

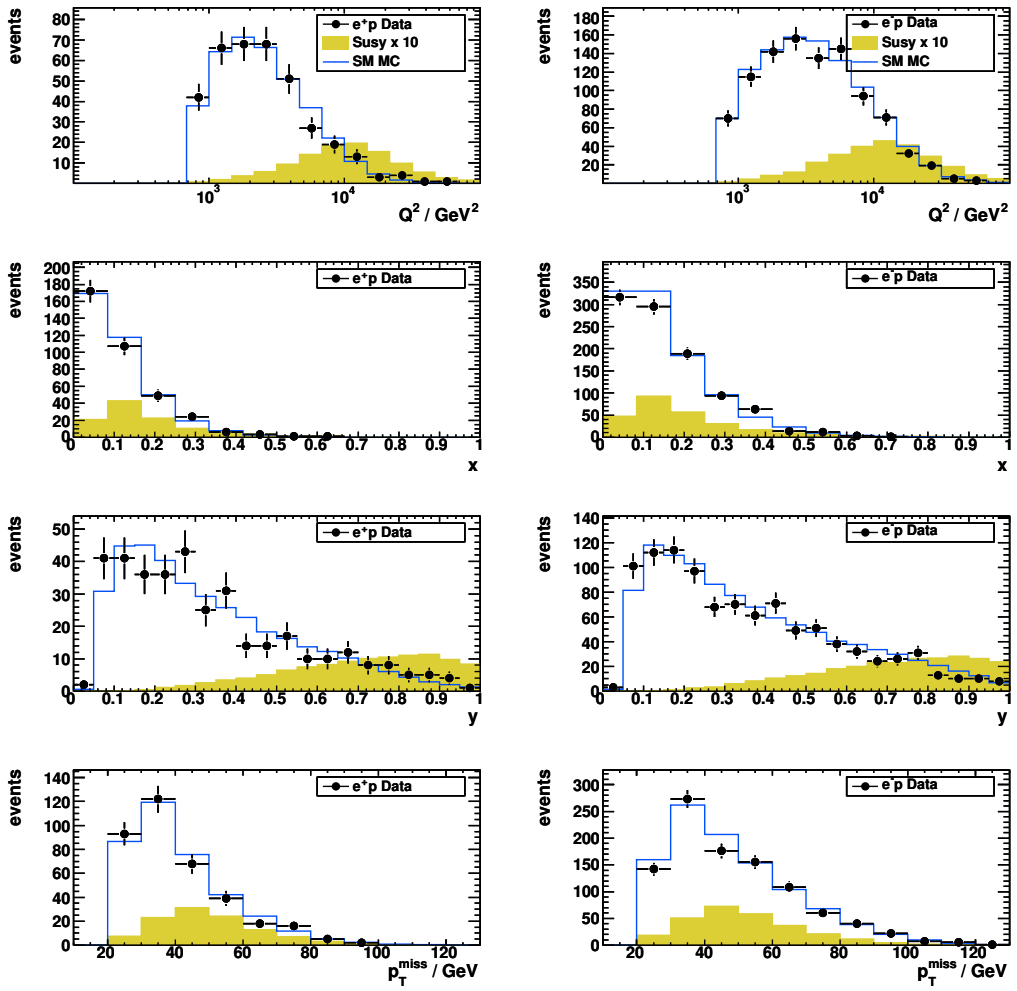

Figure 8.4: Distributions for kinematic variables: Q^2, x and y. Additionally, the missing p_T from the CAL is plotted.

8.2.4 Missing Transverse Momentum

Because both the gravitino in the signal process and the neutrino in the CC background process carry away undetected momentum, a large p_T^{miss} is required to reject photoproduction events, where the transverse momentum is balanced:

$$p_T^{\mathrm{miss}} > 20\,\mathrm{GeV}. \tag{8.6}$$

The distribution of the missing transverse momentum is shown in Figure 8.4. The Standard Model MC describes the data reasonably.

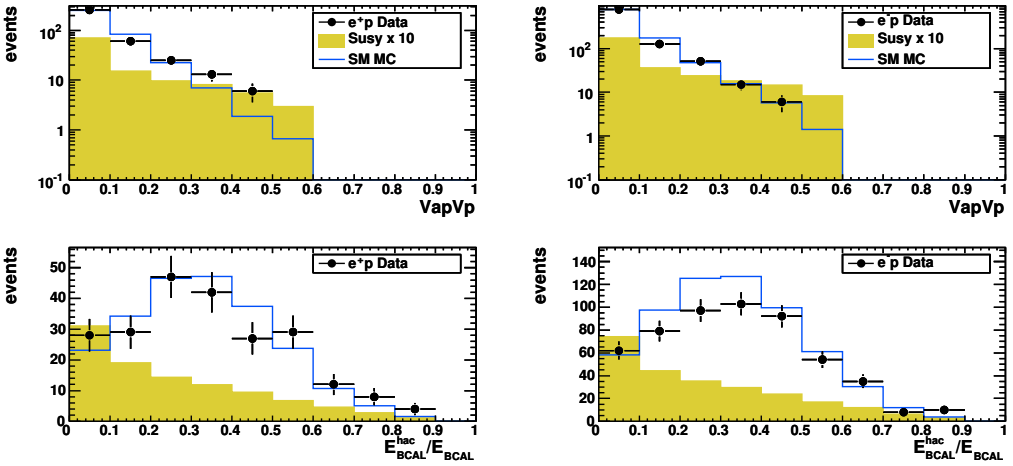

Figure 8.5: Distributions of Vap/Vp (without further restriction) and $E_B^{\mathrm{HAC}}/E_B^{\mathrm{CAL}}$ (only for events with BCAL energy greater than 5 GeV).

Beam gas events can also have a large missing p_T signature, which is however mainly close to the beam pipe and mostly contained in the CAL cells of the inner FCAL ring. This leads to a requirement on $p_T^{-\text{i. Ring}}$, which is the transverse component of the momentum calculated as in Equation (4.2), except that the sum does only run over FCAL cells excluding the inner ring:

$$p_T^{-\text{i. Ring}} > 20\,\mathrm{GeV}. \tag{8.7}$$

8.2.5 Calorimeter Energy Ratios

In ep collision events there is usually a significant fraction of the total BCAL and RCAL energy deposited in the electro-magnetic part (in the FCAL this does not hold, due to the typically very forward proton remnant). These fractions can be used to reject some non-ep background like cosmic muons by the requirement

$$\begin{aligned} E_B^{\mathrm{HAC}}/E_B^{\mathrm{CAL}} &> 0.9 \quad \text{if} \quad E_B^{\mathrm{CAL}} > 5\,\mathrm{GeV}, \\ E_R^{\mathrm{HAC}}/E_R^{\mathrm{CAL}} &> 0.9 \quad \text{if} \quad E_R^{\mathrm{CAL}} > 5\,\mathrm{GeV}. \end{aligned} \tag{8.8}$$

The distributions of this ratios are shown in Figure 8.5.

8.2.6 Timing

To reject events not coming from ep interactions, the timing information from the calorimeter can be used. ep events happen in a time window around the nominal collision time and fulfil certain conditions on the timing differences for the signal between RCAL and FCAL and between upper and lower CAL. Details can be found in Appendix B.2.

Because the timing is not properly simulated in the Monte Carlo, and non-ep events are not simulated at all, this cut is applied to data only.

8.2.7 Halo Muons

Events with a low hadronic angle $\gamma_0 < 0.4\,\mathrm{rad}$ and with no photon of energy $E_\gamma > 30\,\mathrm{GeV}$, can be rejected as halo muons, when the FCAL energy is either not

spread over all layers,

$$\begin{aligned} \frac{E_F^{\mathrm{EMC}}}{E_F^{\mathrm{CAL}}} &< 0.1, \\ \frac{E_F^{\mathrm{HAC1}}}{E_F^{\mathrm{CAL}}} &< 0.1, \\ \text{or} \quad \frac{E_F^{\mathrm{HAC2}}}{E_F^{\mathrm{CAL}}} &> 0.5, \end{aligned} \tag{8.9}$$

or when the FCAL cluster is only located in one tower or module,

$$\begin{aligned} N_{\mathrm{towers}}^{\mathrm{FCLUS}} &< 2, \\ \text{or} \quad N_{\mathrm{modules}}^{\mathrm{FCLUS}} &< 2, \end{aligned} \tag{8.10}$$

or has insufficient transverse energy,

$$E_T^{\mathrm{FCLUS}} < 10\,\mathrm{GeV}, \tag{8.11}$$

or has a significant associated RCAL cluster,

$$E_{\mathrm{asso}}^{\mathrm{RCLUS}} < 10\,\mathrm{GeV}. \tag{8.12}$$

8.2.8 Jet Shape

To reject photoproduction events that are falsely identified as signal events, the fact that their events are less collimated can be exploited. This is reflected in the ratio V_{AP}/V_P of the (anti-)parallel components of their vectorial transverse momentum $\vec{p_T}$,

$$\begin{aligned} V_{AP} &= \sum_{\substack{i \\ \vec{p}_{T,i}\cdot\vec{n}_{p_T}<0}} \vec{p}_{T,i} \cdot \vec{n}_{p_T}, \\ V_P &= \sum_{\substack{i \\ \vec{p}_{T,i}\cdot\vec{n}_{p_T}>0}} \vec{p}_{T,i} \cdot \vec{n}_{p_T}, \end{aligned} \tag{8.13}$$

where the sums are performed over all calorimeter cells and $\vec{n}_{p_T} = \vec{p}_{T,\mathrm{miss}}/p_{T,\mathrm{miss}}$. A value of

$$V_{AP}/V_P < 0.6 \tag{8.14}$$

is required, which is less strict than in the standard CC analyses, because the SUSY signal extents higher into the V_{AP}/V_p region than the CC events (but still less than typical photoproduction events).

8.2.9 Scanning by Eye

Scanning of the events that passed the selection revealed, that some of them were clearly background not coming from *ep* collisions and consequently not simulated by the Monte Carlo. It was decided to manually reject these events. For this purpose the scan list used for the ZEUS CC analysis was completed with some other unambiguous events found in this analysis. A total of 9 events was rejected exclusively this way.

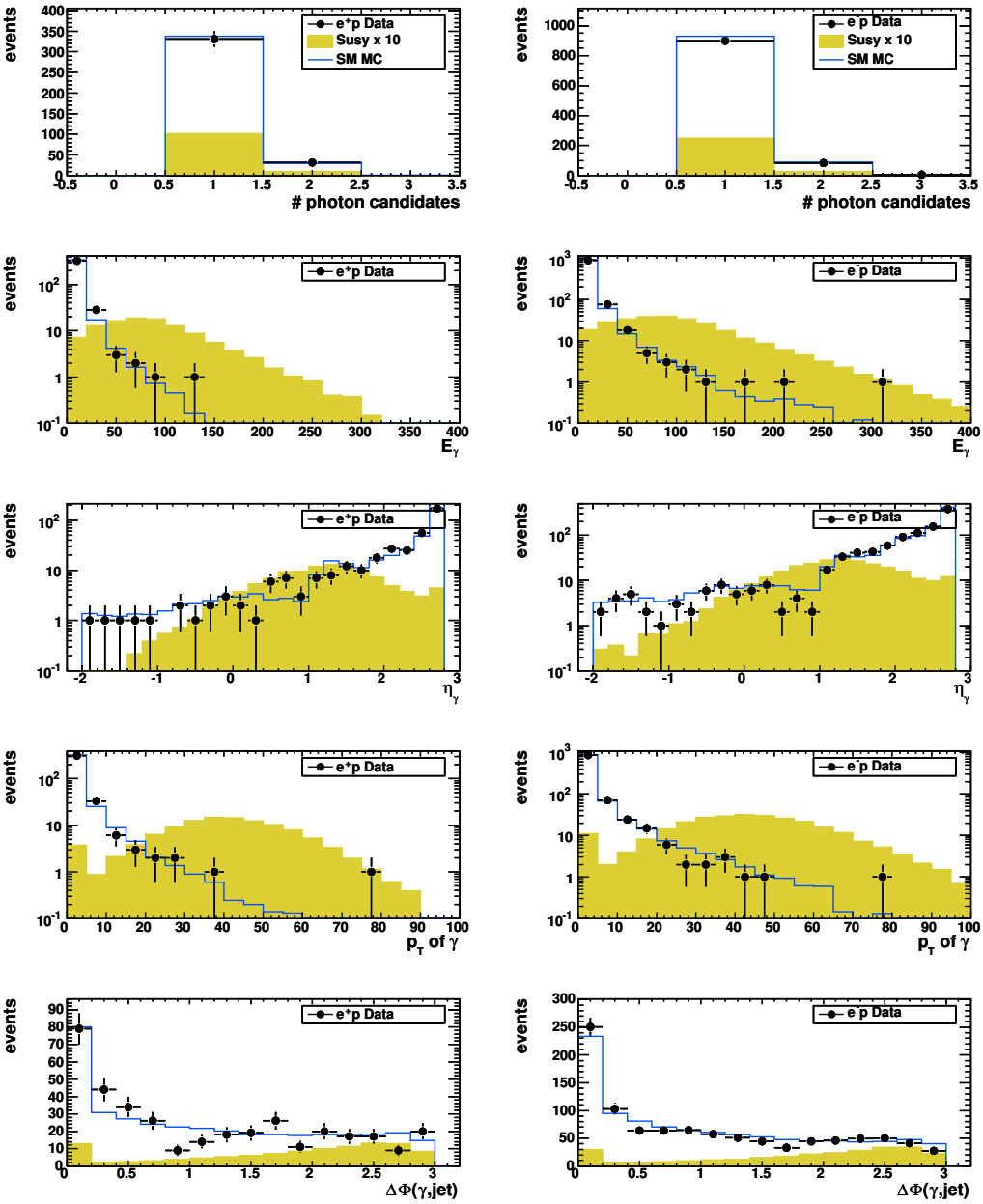

Figure 8.6: Number of photon candidates and properties of the most-energetic photon candidate: Energy, pseudo-rapidity, transverse momentum and azimuthal angle between most-energetic photon and leading jet.

8.2.10 High Energetic Photon

As a strong cut against CC background a high energetic photon is required. Photon candidates are essentially electron candidates found by the electron finder EM (see Section 4.4) without a track. They have to be in a region with good acceptance,

$$-2 < \eta^{\gamma} < 2.8, \tag{8.15}$$

have a reasonable energy,

$$E^{\gamma} > 4\,\mathrm{GeV}, \tag{8.16}$$

and a significant total EM probability,

$$\mathcal{P} > 10^{-4}. \tag{8.17}$$

For the isolation from charged tracks the distance of closest approach on the CAL plane has to be large:

$$\mathrm{DCA} > 30\,\mathrm{cm}. \tag{8.18}$$

To further reject NC events, which are characterised by an electron and a jet which are – in leading order perturbation theory – back-to-back, a cut on the azimuthal angle

$$\Delta\Phi(\gamma, \mathrm{jet}) < 2.95\,\mathrm{rad}, \tag{8.19}$$

is applied to reject events were the electron track is not properly reconstructed and fakes a photon.

The distributions of quantities related to the photon candidate are shown in Figure 8.6. In general, the data are quite well described by the Standard Model MC. Some outliers can be seen in the tails of the signal region.

At a later step (Section 9.3) the photon requirement will be tightened more before calculating the discriminant.

8.2.11 No High-Energetic Electron

Because some events that look like NC events ended up in the final selection as SUSY candidates,[3] a cut against high-energetic electrons was introduced. Events with

$$E^{\mathrm{el}} > 8\,\mathrm{GeV} \qquad \wedge \qquad \mathrm{DCA} < 5\,\mathrm{cm} \tag{8.20}$$

are rejected. These are events with significant deposits in the electromagnetic calorimeter, which, due to the short distance to the next charged tracks, are very likely no photons

Distributions of these quantities are shown in Figure 8.7.

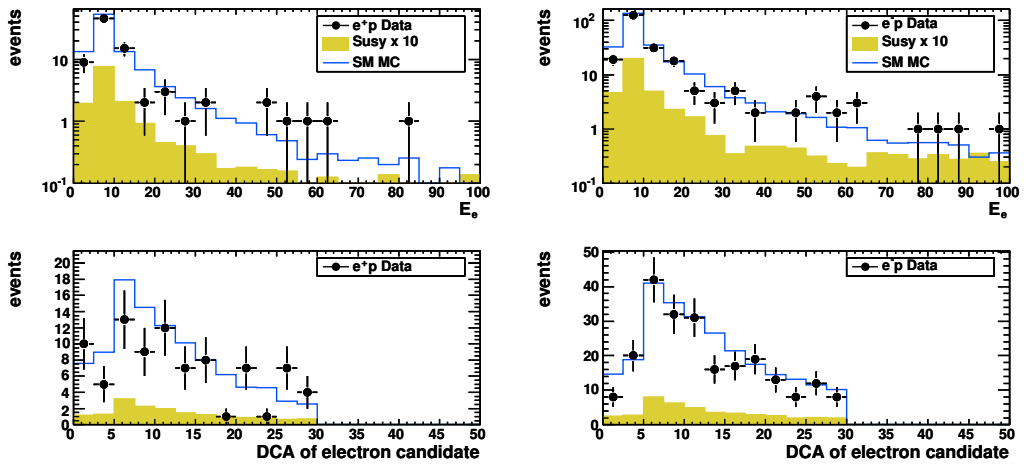

Figure 8.7: Distribution of the electron energy and distance of closest approach to the nearest track.

[3] Although no generated NC events were selected; probably some part of the phase space is not perfectly reproduced by the Monte Carlo.

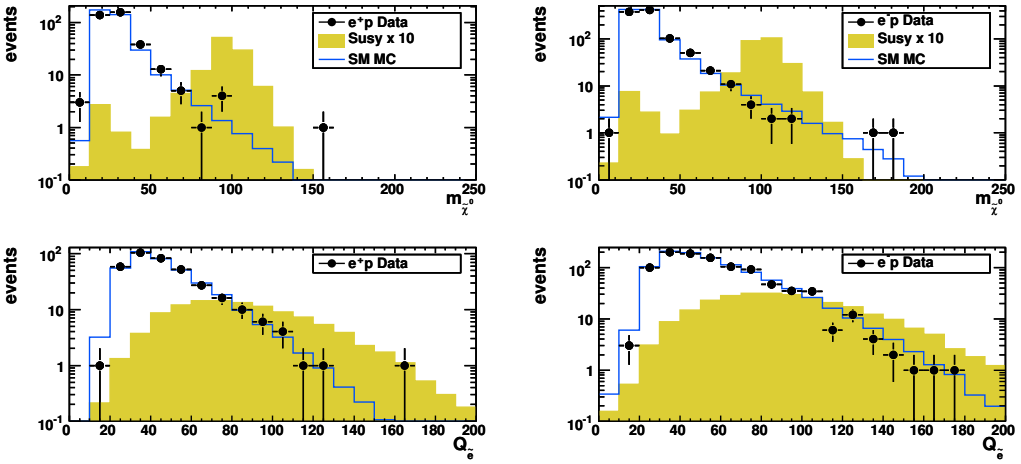

Figure 8.8: Distribution of the reconstructed neutralino mass and four-momentum transferred by the selectron.

	Background		Signal	
Cut	$r_{\text{incl.}}/\%$	$r_{\text{excl.}}/\%$	$r_{\text{incl.}}/\%$	$r_{\text{excl.}}/\%$
FLT	0.37	0.07	0.83	0.5
DST 34	7.16	0.0	1.02	0.0
No halo muons	1.32	0.02	0.03	0.0
No beam gas	0.07	0.01	0.04	0.01
CAL ratios	0.13	0.0	0.29	0.12
Zvtx	5.32	0.24	3.74	1.64
Q2	40.31	0.15	12.42	3.29
Good jet	44.36	0.4	6.83	3.42
Pt excl. 1 iR	49.5	0.52	9.61	0.59
Pt	38.29	0.01	8.47	0.13
Good track	3.0	0.18	2.96	1.41
No electron	4.85	0.35	13.26	2.64
Photon candidate	84.7	25.25	25.66	12.25
$\Delta\Phi(\gamma, \text{jet})$	0.89	0.32	9.66	4.68

Table 8.2: Inclusive and exclusive rejection rates for signal and background, for a neutralino mass of $m_{\tilde{\chi}^0} = 96\,\text{GeV}$.

8.3 Efficiencies and Rejection Rates

To study the effects of the different cuts, for each cut i the rejection rates

$$r^i_{\text{incl./excl.}} = \frac{N_{\text{cut/excl.cut}}}{N_{\text{total}}} \tag{8.21}$$

were calculated. Here $r^i_{\text{incl.}}$ is the fraction of events rejected by the cut i, and $r^i_{\text{excl.}}$ is the fraction of events that are removed by the cut i and no other cut. The numbers are listed in Table 8.2 for the reference parameter point with $m_{\tilde{\chi}^0} = 96\,\text{GeV}$ and $m_{\tilde{\text{e}}} = 140\,\text{GeV}$.

Some cuts (like the p_T cut) inclusively cut a large number of signal events. Releasing them would not increase the overall signal efficiency very much, because their inclusive signal rejection rate is low.

The cut against high energetic electrons and the cut on the angle between the photon candidate and the leading jet exclusively removes a significant fraction of signal events and a smaller fraction of CC DIS events. Yet, they were kept in order to reject NC DIS events (which are not shown in this table). Giving numbers on the cut performance on NC events would be misleading, because it was observed that some events that turned out to be clear NC events when examined with the event display passed all cuts, although all NC Monte Carlo events were rejected.

Requiring a photon is absolutely necessary. Unfortunately, it rejects a significant portion of the signal. This is due to passive matter in the detector (some of this was introduced with the MVD, which was not present in older HERA data), which causes some photons to undergo photon conversion before they reach the calorimeter.

The question arises how the rejection rates change with the neutralino mass $m_{\tilde{\chi}^0}$ and the selectron mass $m_{\tilde{e}}$. Varying $m_{\tilde{e}}$ has a vanishing effect on the kinematic quantities and on the number of rejected events [4]. The dependence of the cut rejection rates on $m_{\tilde{\chi}^0}$ is shown in Figure 8.9 for the most important cuts. The p_T cut is most effective at low neutralino masses, because the missing transverse momentum is due to the escaping gravitino, whose momentum distribution follows a Jacobian peak around half the neutralino mass, smeared out due to the Lorentz transformation and the finite detector resolution.

The higher the neutralino mass, the less phase space is available for the process, so that the photon as well as the jet are found in the forward section of the detector. Here the tracking is difficult, so that the reliance on a good track becomes problematic. Also, the reconstruction of the jet is less efficient there. Thus the corresponding cuts reject more signal events for high-mass neutralinos.

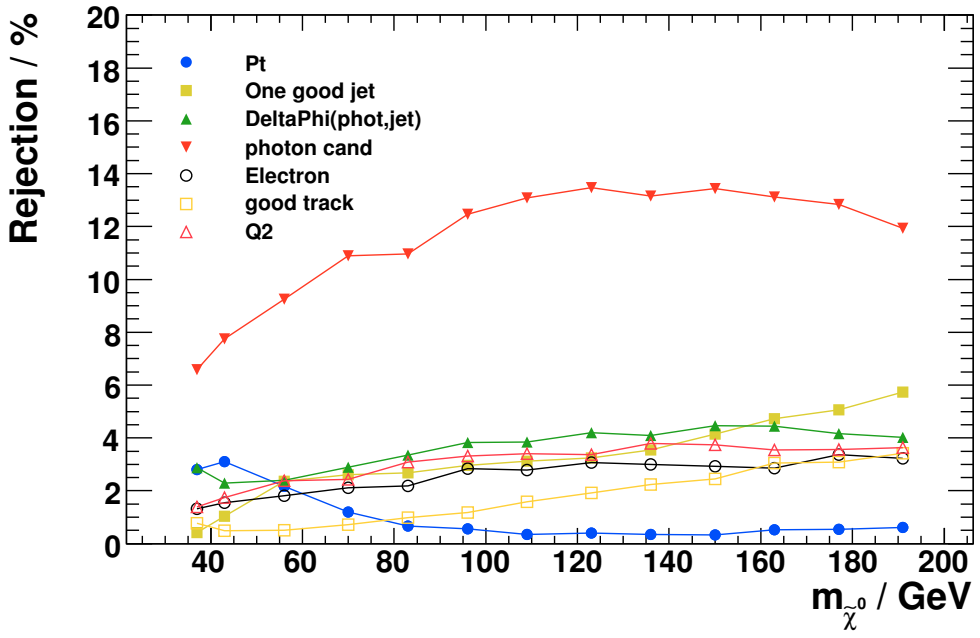

Figure 8.9: Fraction of signal events exclusively cut by main cuts for different neutralino masses.

The resulting signal selection efficiency for different neutralino masses is shown in Figure 8.10. For low neutralino masses the efficiency is very low, but it rises steeply and reaches a plateau around $m_{\tilde{\chi}^0} = 90\,\mathrm{GeV}$.

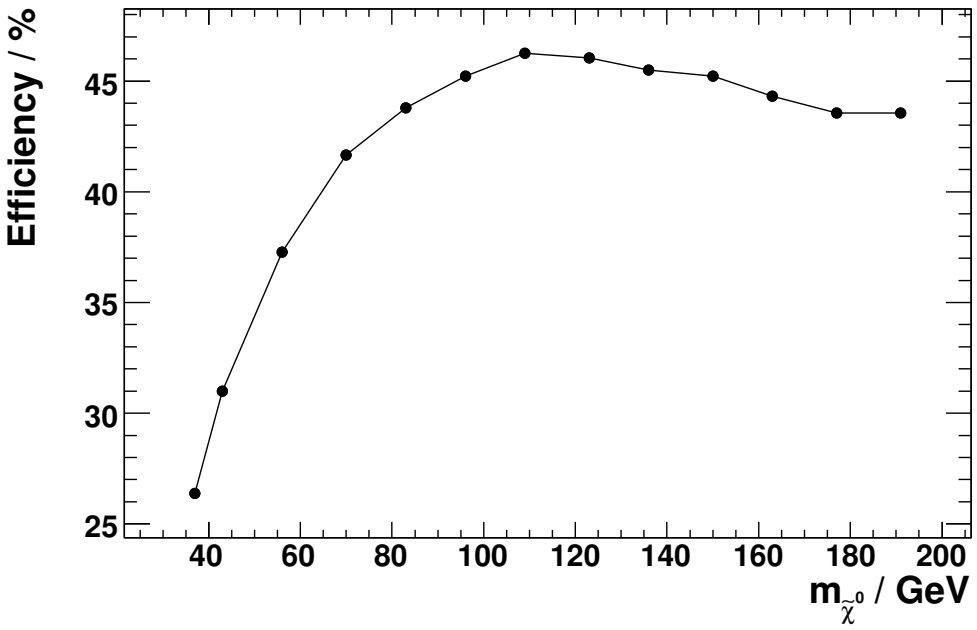

Figure 8.10: Signal selection efficiency for different neutralino masses.

Chapter 9

Discriminant Method

9.1 Multivariate Data Analysis

In this analysis, no single quantity calculated from the event data has a sufficient separation power to enable a good signal-to-background ratio via simple 1-dimensional cuts in the presence of only a small number of signal events over an irreducible background. Therefore, it is necessary to combine several variables and compute a discriminant value out of them on an event-by-event basis, in a mapping of a n-dimensional space of observables onto an 1-dimensional classifier space, which is often the interval $[0, 1]$. Usually the lower end of this interval corresponds to background-like events, the higher end corresponds to signal-like events.

In order to calculate this decision for real data events, the multivariate data analysis (MVA) algorithm has to be trained on simulated events for these two classes. It is crucial to tune the settings of the algorithm to provide a good separation while avoiding overtraining, i.e. the sensitivity to features of the training samples which are only statistical fluctuations.

A certain threshold discriminant value separates the good signal candidates, or the discriminant distribution for the data can be compared to the expected distribution to calculate exclusion limits or discovery significances.

There are many different classification algorithms with even more settings and sub-algorithms on the market, each with particular strengths and weaknesses. Most of them are implemented in a canonical way in the TMVA (Toolkit for Multivariate Data Analysis) framework [83] for ROOT [56], which was used in this analysis.

Out of these, the PDERS algorithm (Probability Density Estimator based on Range-Searching) proved to be the best choice. Other algorithms, like an artificial neural network, did not perform better.

9.2 Probability Density Estimator Range Search

Since the exact probability density functions for signal and background are unknown, the principle of the PDERS algorithm [84] is to count the normalised number n_S of signal and n_B of background training events in some volume V around a test event i. The ratio

$$D(i) = \frac{n_S(i, V)}{n_S(i, V) + n_B(i, V)} \tag{9.1}$$

serves as a discriminant value and is an estimate for the probability of the test event being of the signal class.

The event counting for every test event is computationally intensive. To make it feasible a range-searching algorithms based on binary trees is used [85].

Apart from the computational complexity it was shown [84] that the PDERS algorithm is compatible to artificial neural networks (ANNs), and has the additional benefit of being more intuitive and transparent.

There are two improvements of original PDERS algorithm in the TMVA implementation used in this analysis:

- It is possible to choose the shape and size of the volume V different from a rigid multi-dimensional box.
- To weight the training events according to their distance from the test events and to smooth out the classification behaviour, the events can be weighted with kernel functions.

9.2.1 Choice of the Volume

The simplest choice for the volume would be a rigid box, with sizes fixed a priori or depending on the event distribution in each dimension.

This analysis uses a more flexible (but with the need for more computing time) adaptive volume with better performance. Here bounds for the minimum and maximum numbers of events per volume were set (1000 and 1200 in this analysis after some optimisation for separation power and minimal overtraining), and the estimator then adjusted the volume size dynamically, so that for each test event the number of training events inside the volume lies within this user-defined range. This requirement automatically enlarges the volume in scarcely populated phase space regions and makes the graining fine in strongly populated areas.

9.2.2 Choice of Kernel Function

Simple choices are kernels with no weighting (a box), or a hyper-ellipsoid that modifies the volume shape without additional weighting. In these cases the probability estimate is very sensitive to the exact placement of the sampling volume boundaries.

To smooth out this behaviour, a Gaussian weighting of the training events according to their distance to the test event can be applied, where the width σ of the Gaussian (in units of the volume size) can be selected freely. For this analysis $\sigma = 0.3$ was found as an optimal choice to maximise separation power and to minimise overtraining.

9.3 Tighter Photon Selection

Up to now rather soft cuts on the photon are applied (cf. Section 8.2.10) in order to enable a high-statistics comparison with Standard Model expectations. This demonstrates a good agreement with a radiative Charged Current selection. However, the events with low-p_T photons dominating this process are irrelevant for SUSY searches. For this reason and in order to suppress possible photon misidentification from π^0 background additional cuts are applied from now on:

- $\eta_\gamma > 0$ is required, because the signal photons, coming from the decay of a heavy particle, are boosted almost completely in the forward region (cf. Figure 8.6).

- $p_{T,\gamma} > 10\,\mathrm{GeV}$ is required in addition. The vast majority of signal photons has a greater transverse momentum, whereas the low $p_{T,\gamma}$-region suffers from huge background and thus contributes little benefit to the analysis.

9.4 Choice of Variables for Discriminant Analysis

There are constraints on the input variables for the discriminant analysis:

- They should have good separation power by themselves to be useful.
- They should be reasonably uncorrelated to make the phase space economic and avoid use of redundant information.

To this effect, the following variables were chosen:

CalEmPz, the global $E - p_z$, measured in the calorimeter. This quantity tends to be greater for signal events, since the gravitino is travelling more forward than the neutrino in CC events, (cf. Equation (4.19)).

NeutralinoMass, the reconstructed mass of the neutralino (cf. Equation (4.23)), peaks around the neutralino mass for the signal process. For the background process, the peak is at lower values and is an effect of the typical falling p_T spectrum and the lower p_T cut.

NeutralinoEta, the reconstructed pseudo-rapidity of the neutralino, $\eta_{\tilde{\chi}}$. In the signal process, the neutralino travels quite forward, whereas the corresponding quantity for background processes is to a large extent meaningless and thus centred around 0.

PtSum, $p_{T,\gamma} + p_{T,\mathrm{jet}}$. The combination of high photon momentum and high jet momentum is typical for signal events.

DPhiGravJet, the azimuthal angle $\Delta\Phi(\tilde{G}, \mathrm{jet})$ between the missing momentum and the jet. In CC DIS the neutrino and the jet are back-to-back. The additional photon contributes to the momentum balance and makes the angular distribution nearly flat.

QSelectron, the reconstructed four-momentum transferred by the selectron, $Q_{\tilde{e}}$, defined in Equation (4.24). This quantity relies also on a proper reconstruction of the neutralino and thus differs for background processes without a neutralino.

Figure 9.1 shows the distributions of these variables. Their linear correlations are shown in Figure 9.2. Most correlated are $Q_{\tilde{e}}$ and $p_{T,\gamma} + p_{T,\mathrm{jet}}$, and, to a lesser degree, $\eta_{\tilde{\chi}}$. Still, including all these variables improved the discriminant, so they were kept. Moreover, the correlations are only pronounced in the background sample and much weaker in the signal sample.

Other sets of kinematic quantities were tested as well, but did not improve the results. It was also considered to include calorimetric quantities characterising the shower size and shape of the photon candidate. Since the separation power of these quantities was low and the simulation did not reliably describe this aspect of the data, this approach was discarded.

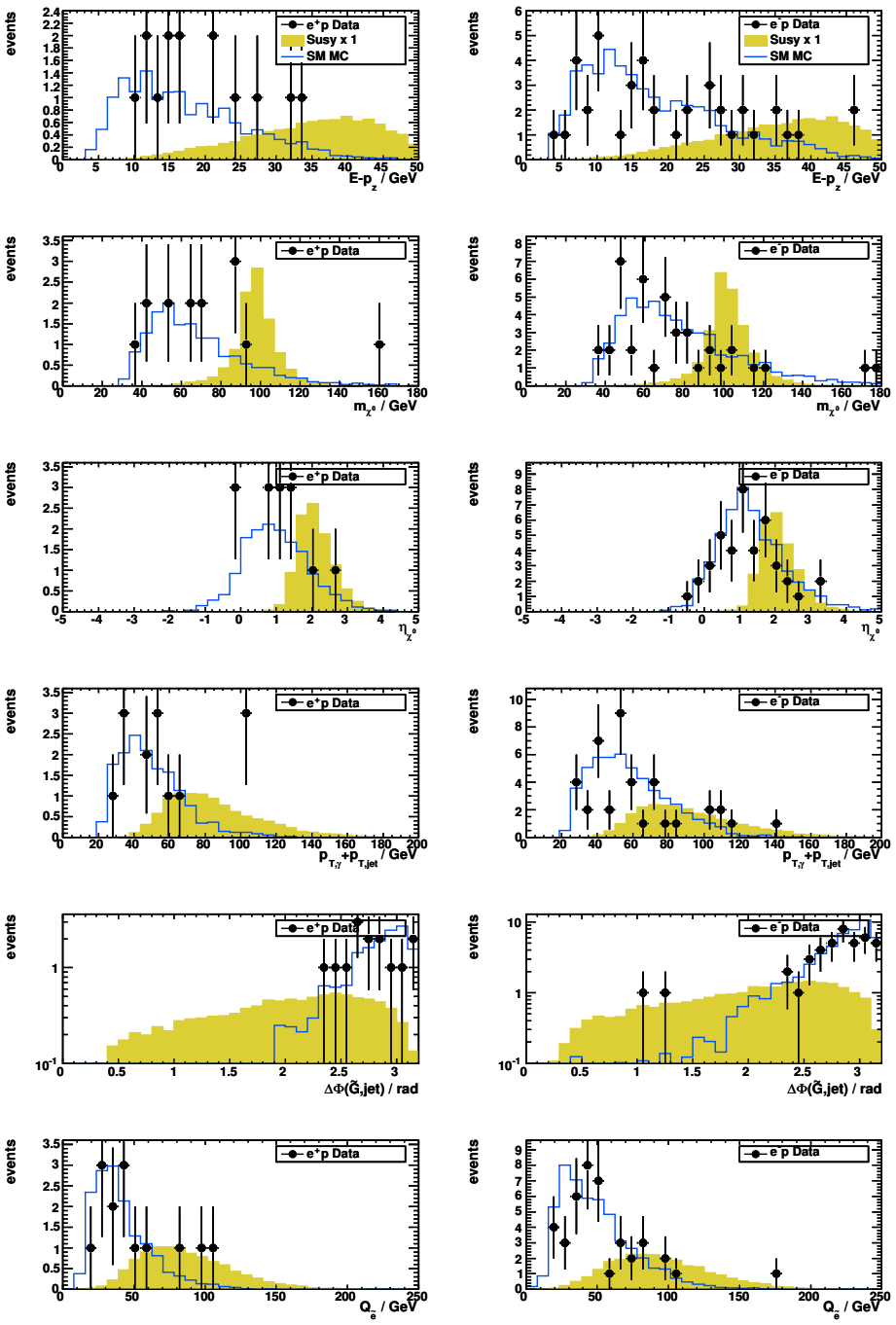

Figure 9.1: Distribution of variables used for the discriminant: CalEmPz, NeutralinoMass, PtSum, DPhiGravJet, NeutralinoEta, QSelectron (definitions in the text).

9.5 Evaluation

Different ways were used to compare and tune the discriminant method to arrive at an optimal signal-background discrimination. The optimisation was done for the model point with $m_{\tilde{\chi}^0} = 96\,\text{GeV}$ and $m_{\tilde{e}} = 140\,\text{GeV}$.

In order to have an estimate for the overtraining, the Monte Carlo background and signal samples were split into two halves. The first one was used to train the

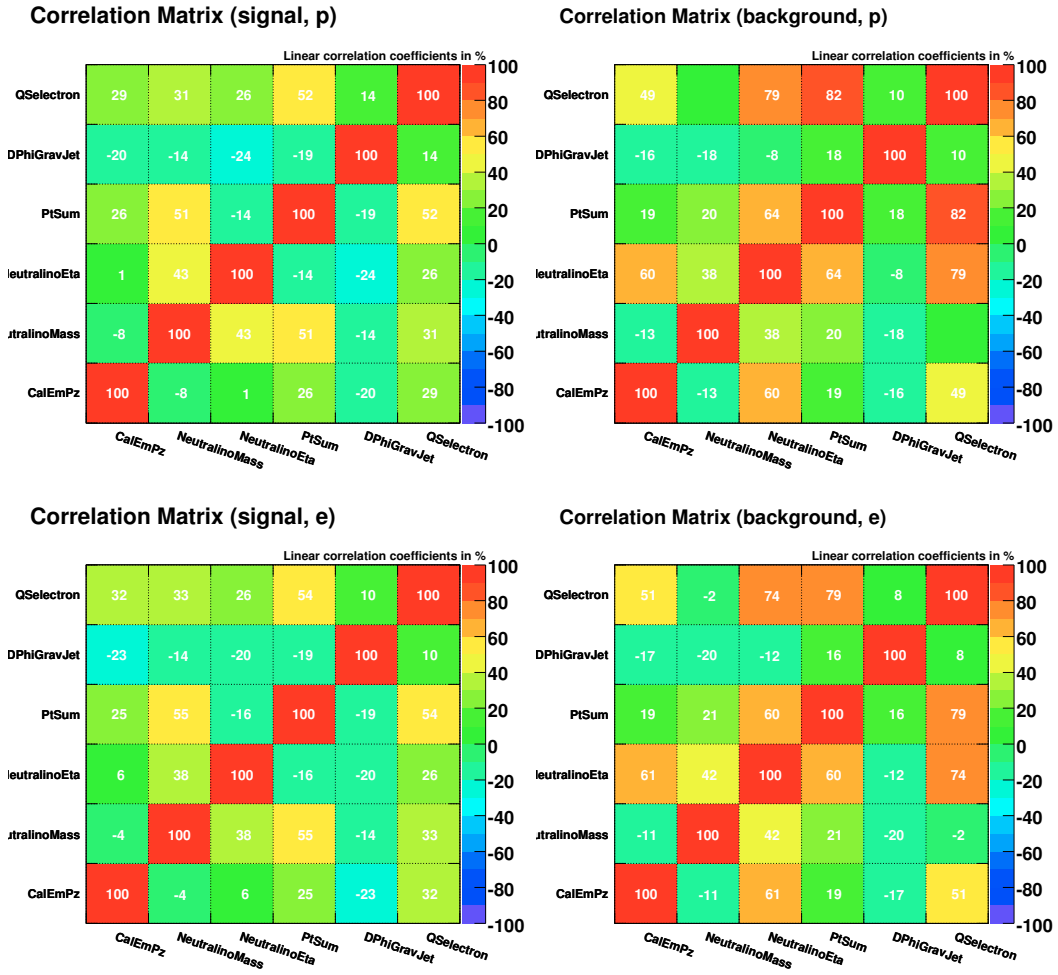

Figure 9.2: Linear correlation coefficients for e^+p (top) and e^-p (bottom), for signal (left) and background (right).

	ϵ_S from test sample (training sample)		
Data Set	at $\epsilon_B = 0.01$	at $\epsilon_B = 0.1$	at $\epsilon_B = 0.3$
e^+p	0.939 (0.953)	0.987 (0.987)	0.998 (0.998)
e^-p	0.918 (0.931)	0.980 (0.981)	0.991 (0.991)

Table 9.1: Signal efficiencies (after the event selection) at different background efficiencies for test and training samples, for e^+p and e^-p data (at $m_{\tilde{\chi}^0} = 96\,\text{GeV}$ and $m_{\tilde{e}} = 140\,\text{GeV}$).

discriminant, the second one to test its performance on an independent sub-sample.

The comparison of signal efficiencies at different background efficiencies in Table 9.1 shows that at lower background efficiencies there is some moderate overtraining, but the performance is still good.

The curve comparing signal efficiency and background rejection is often called receiver operating characteristic (ROC) curve and is shown in Figure 9.3. The area under the curve is 0.995 for e^+p samples and 0.991 for e^-p samples, which is very

close to one and a sign of good discrimination.

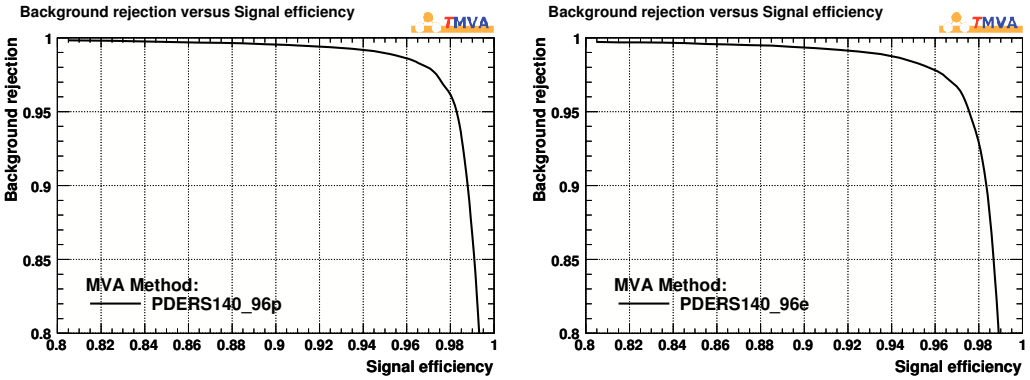

Figure 9.3: Background rejection vs. signal efficiency for e^+p (left) and e^-p (right) .

Other measures for the quality of a discriminant are the separation and the significance.

The separation $\langle S^2 \rangle$ of classifier y is defined as

$$\langle S^2 \rangle = \frac{1}{2} \int \frac{(\hat{y}_S(y) - \hat{y}_B(y))^2}{\hat{y}_S(y) + \hat{y}_B(y)} dy, \tag{9.2}$$

where $\hat{y}_{S/B}(y)$ is the signal/background PDF for y. The separation measures the overlap between signal and background discriminant distributions, where 0 indicates complete and 1 indicates no overlap. For the model point with $m_{\tilde{\chi}^0} = 96\,\text{GeV}$ and $m_{\tilde{e}} = 140\,\text{GeV}$ the separation was calculated as $\langle S^2 \rangle = 0.867$ for e^+p data and $\langle S^2 \rangle = 0.853$ for e^-p data.

The significance s is a measure for distance of the means of the distributions with respect to the widths of the distributions:

$$s = \frac{\langle y_S \rangle - \langle y_B \rangle}{\sqrt{\langle y_S^2 \rangle + \langle y_B^2 \rangle}}. \tag{9.3}$$

For the considered model point and e^+p data the significance is $s = 4.534$, for e^-p data it is $s = 4.043$.

As a last check the discriminant distributions for the training and the testing subsample were examined and compared to detect overtraining. As Figure 9.4 shows, the separation is quite clean, and the testing distribution follows the training distribution in most parts. Only at the end of the tails the test distributions rise again, while the training distributions vanish. Here some slight overtraining is visible. However, the actual amount is small compared to the height of the peak of the other distribution at the sample place. Attempts to reduce this overtraining simultaneously reduced the overall performance of the discriminant and were discarded.

9.6 Final Discriminant Distributions

The discriminant estimator, optimised in the way described above, was applied on the data and the Monte Carlo samples for signal and background. To be able to scan different neutralino masses, and since especially the reconstructed neutralino

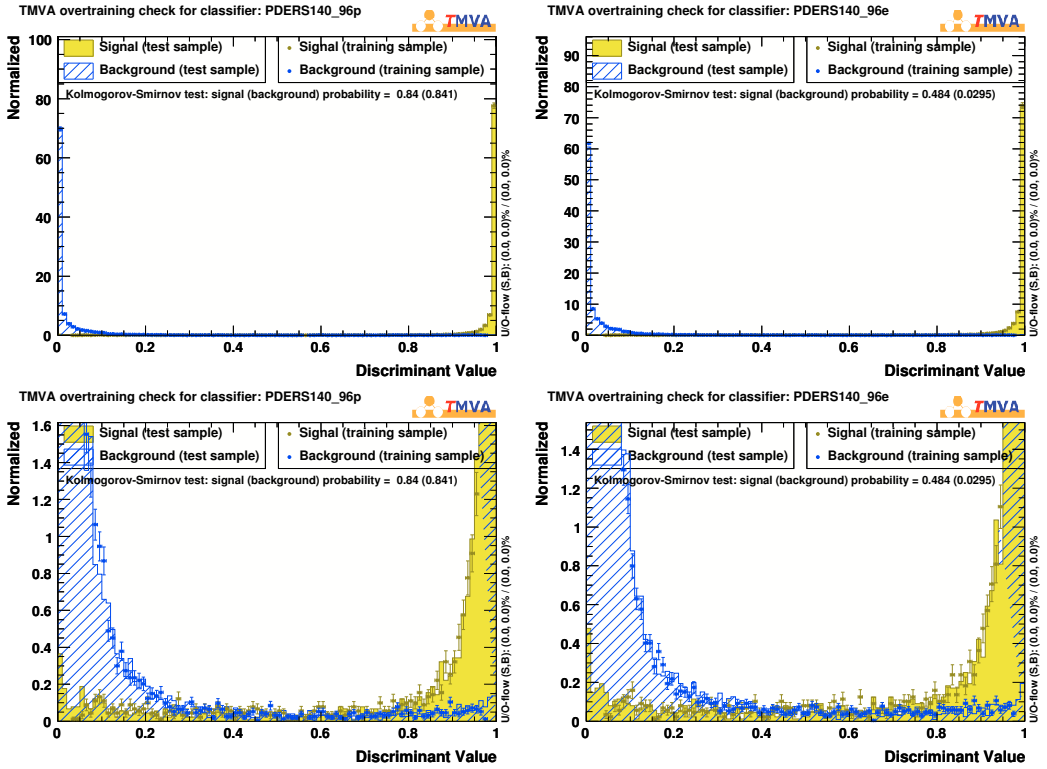

Figure 9.4: Overtraining check for e^+p (left) and e^-p (right). Superimposed are the discriminant distributions for the training sample (dots with statistical error bars) and for the test sample (histograms). The signal distributions are filled and coloured in dark yellow, the background ones are hatched and blue. Both distributions are normalised to 100 events.

mass is one of the input variables for the discriminant estimator, the training of the discriminant was re-iterated for the different neutralino masses.

The resulting distributions are shown in Figure 9.5 for e^+p data and in Figure 9.6 for e^-p data. For neutralino masses greater than the selectron mass, the favoured decay channel for the neutralino changes drastically (see Section 7.1), so that this analysis loses sensitivity to a SUSY signal.

It is also visible that, mostly for low neutralino masses and e^-p data, the number of SUSY candidates found in the data exceeds the Standard Model expectation. It is unclear, if this is a fluctuation, remaining background, or evidence of SUSY.

The location of the SUSY candidates in the control distributions is shown in Section 9.7.

A quantitative analysis of the discriminant distributions is performed with the calculation of exclusion limits (see Chapter 10).

9.7 Location of SUSY Candidates

The plots in this section show the location of the SUSY candidates with a discriminant value $D > 0.8$ for the parameter point with neutralino mass $m_{\tilde{\chi}^0} = 96\,\text{GeV}$ and selectron mass $m_{\tilde{e}} = 140\,\text{GeV}$ before the final photon selection.

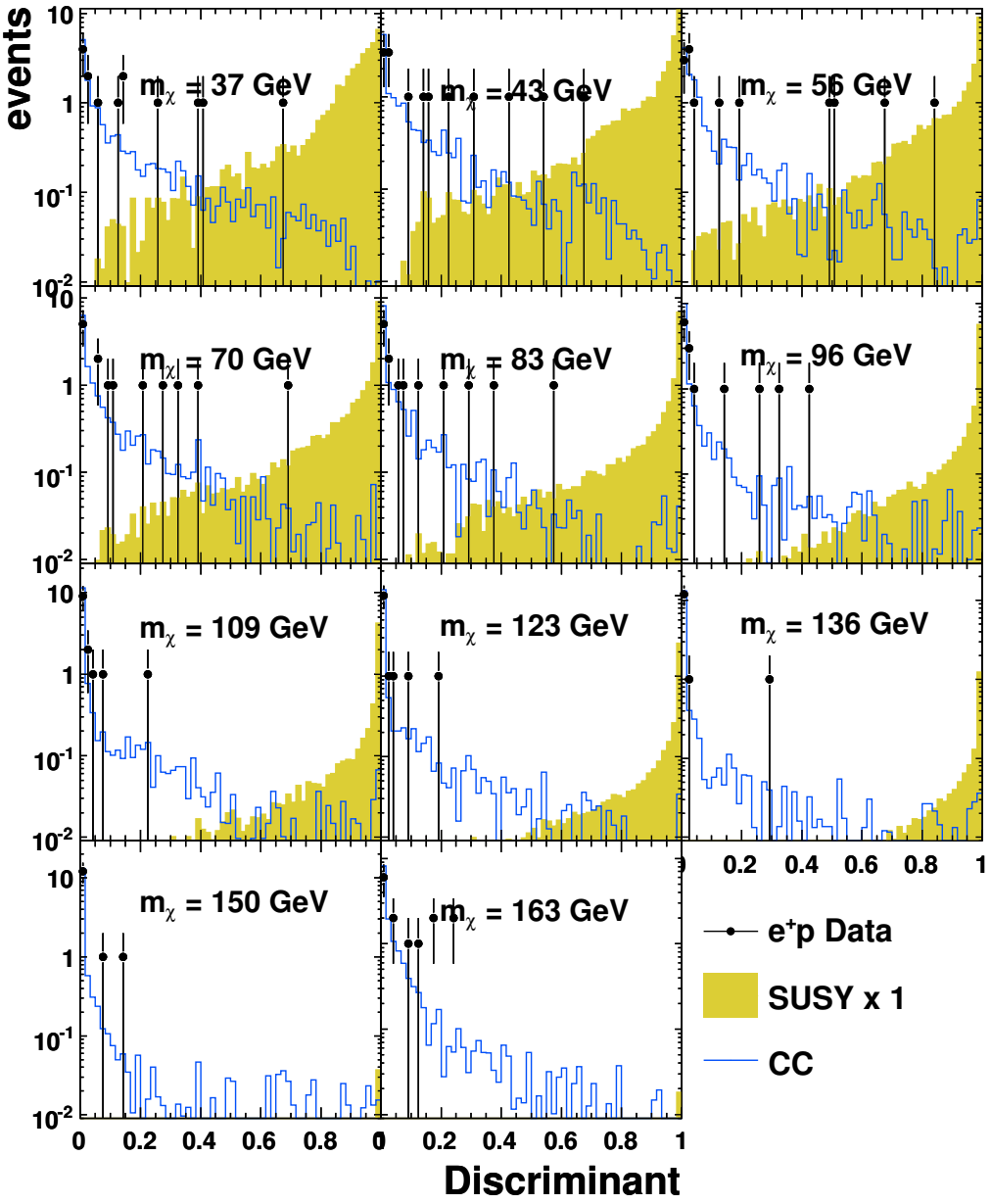

Figure 9.5: Discriminant distributions for e^+p for different neutralino masses $m_{\tilde{\chi}}$ and a selectron mass $m_{\tilde{e}} = 140\,\text{GeV}$. The Standard Model background is the blue line, the SUSY signal the dark yellow shape, and the data are the black dots with statistical error bars.

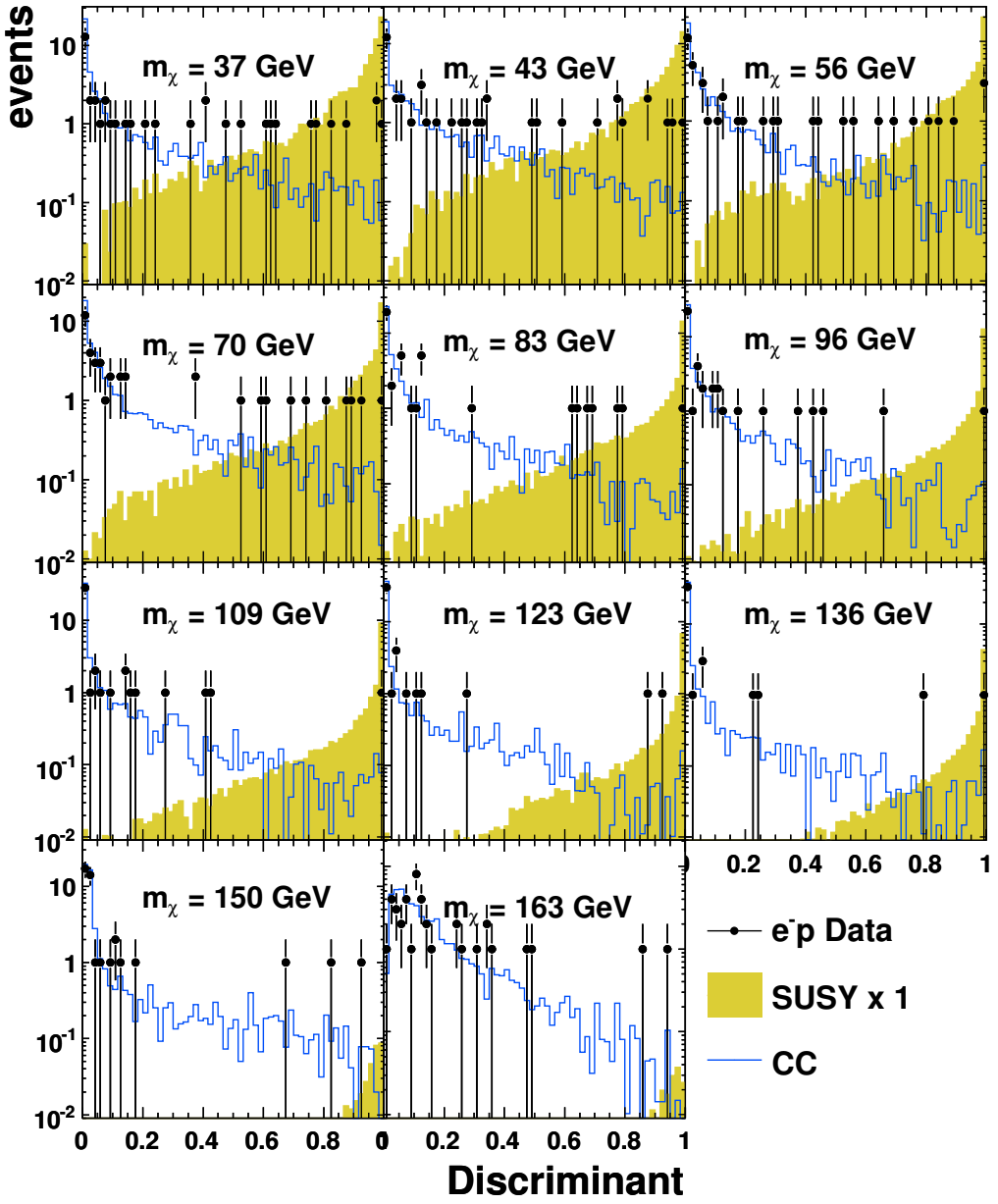

Figure 9.6: Discriminant distributions for e^-p for different neutralino masses $m_{\tilde{\chi}}$ and a selectron mass $m_{\tilde{e}} = 140\,\text{GeV}$. The Standard Model background is the blue line, the SUSY signal the dark yellow shape, and the data are the black dots with statistical error bars.

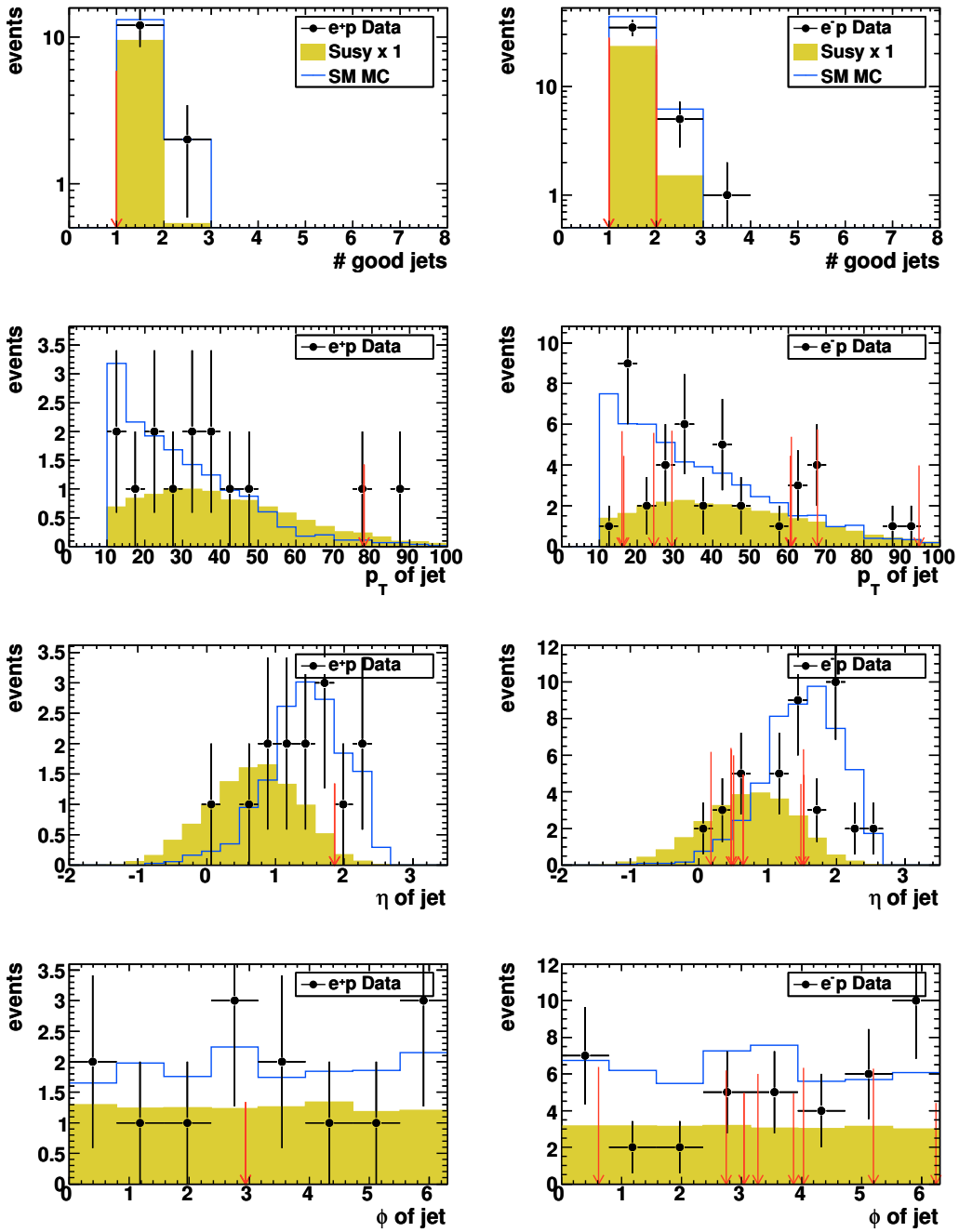

Figure 9.7: Arrows mark events with discriminant value D greater than 0.8. Arrow length is proportional to D^2.

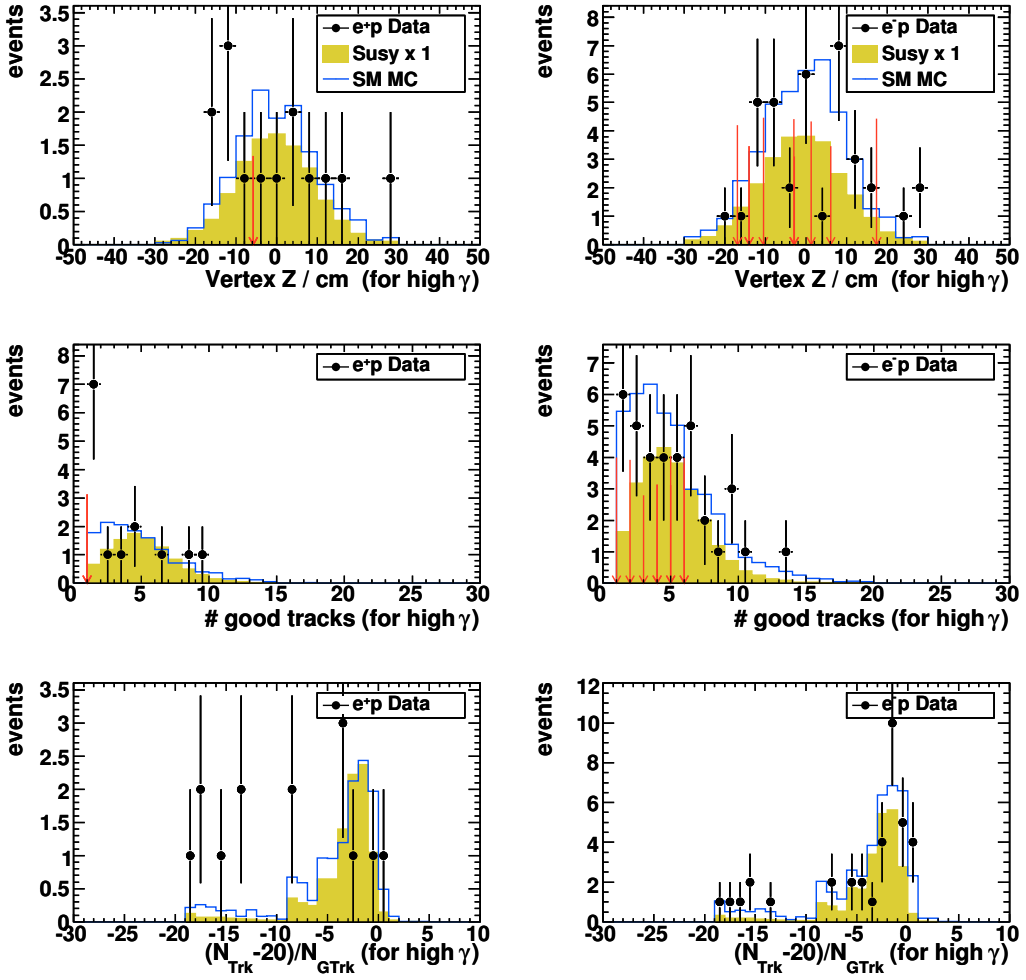

Figure 9.8: Arrows mark events with discriminant value D greater than 0.8. Arrow length is proportional to D^2.

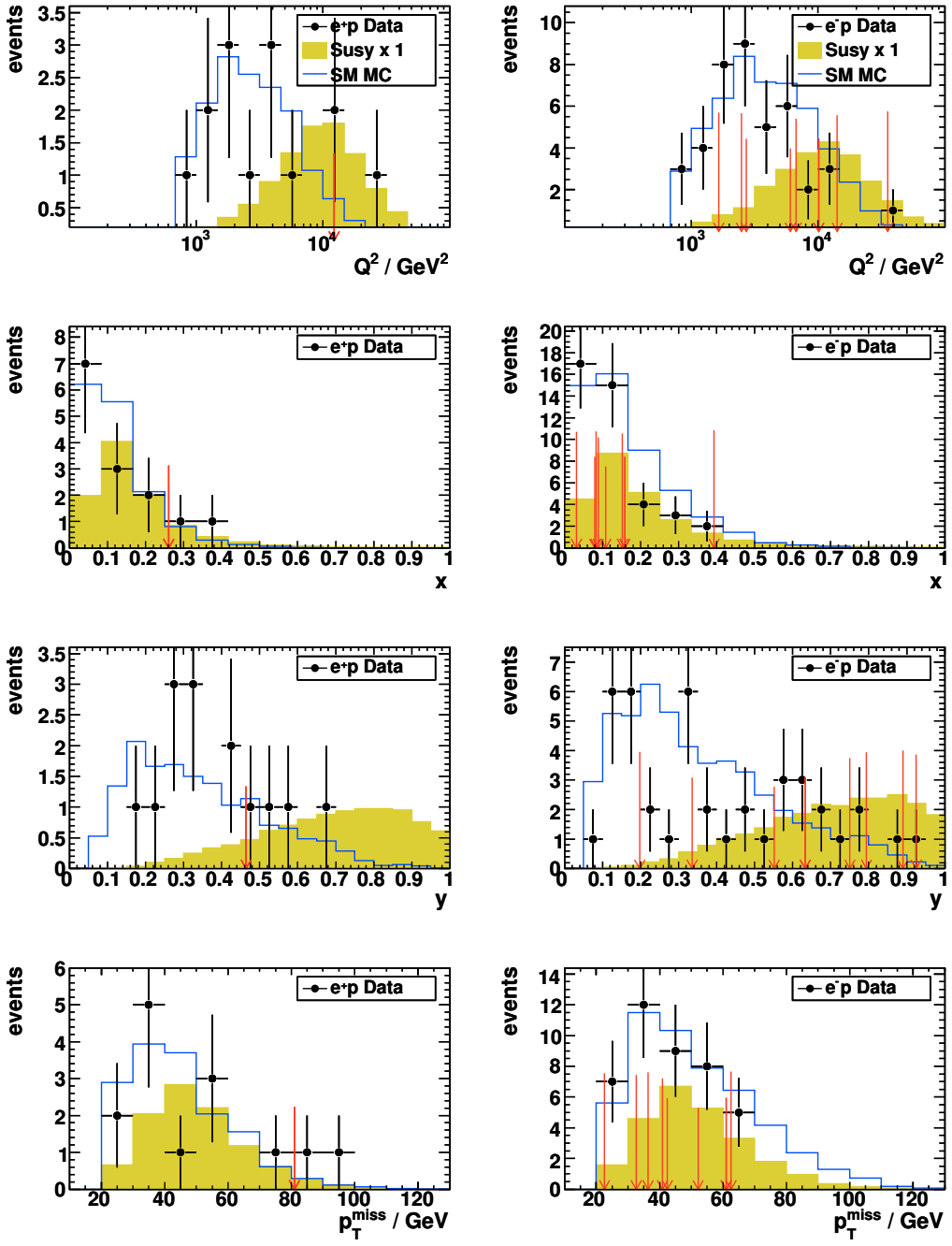

Figure 9.9: Arrows mark events with discriminant value D greater than 0.8. Arrow length is proportional to D^2.

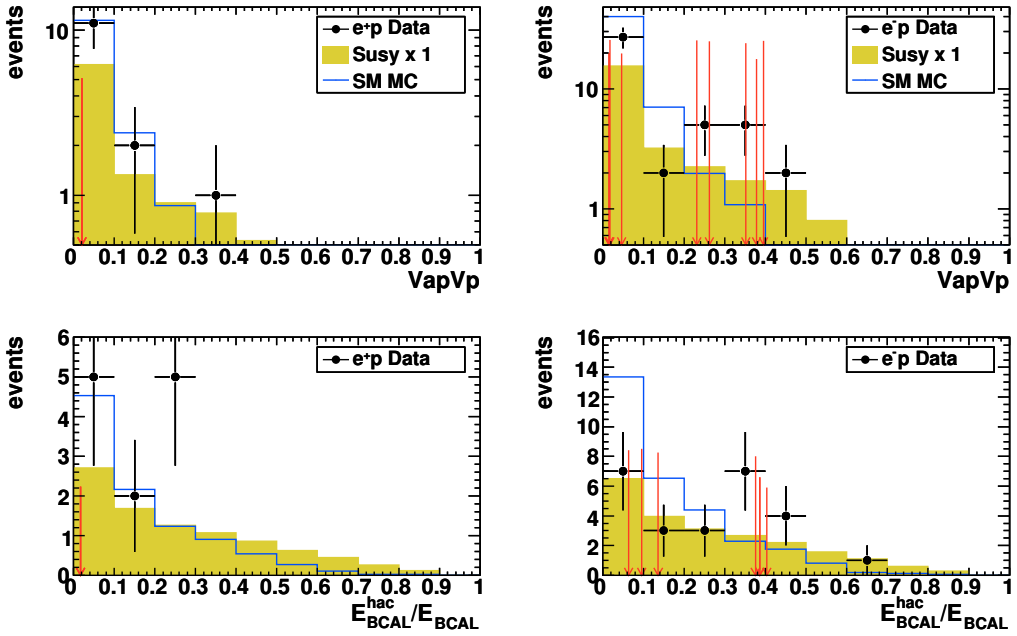

Figure 9.10: Arrows mark events with discriminant value D greater than 0.8. Arrow length is proportional to D^2.

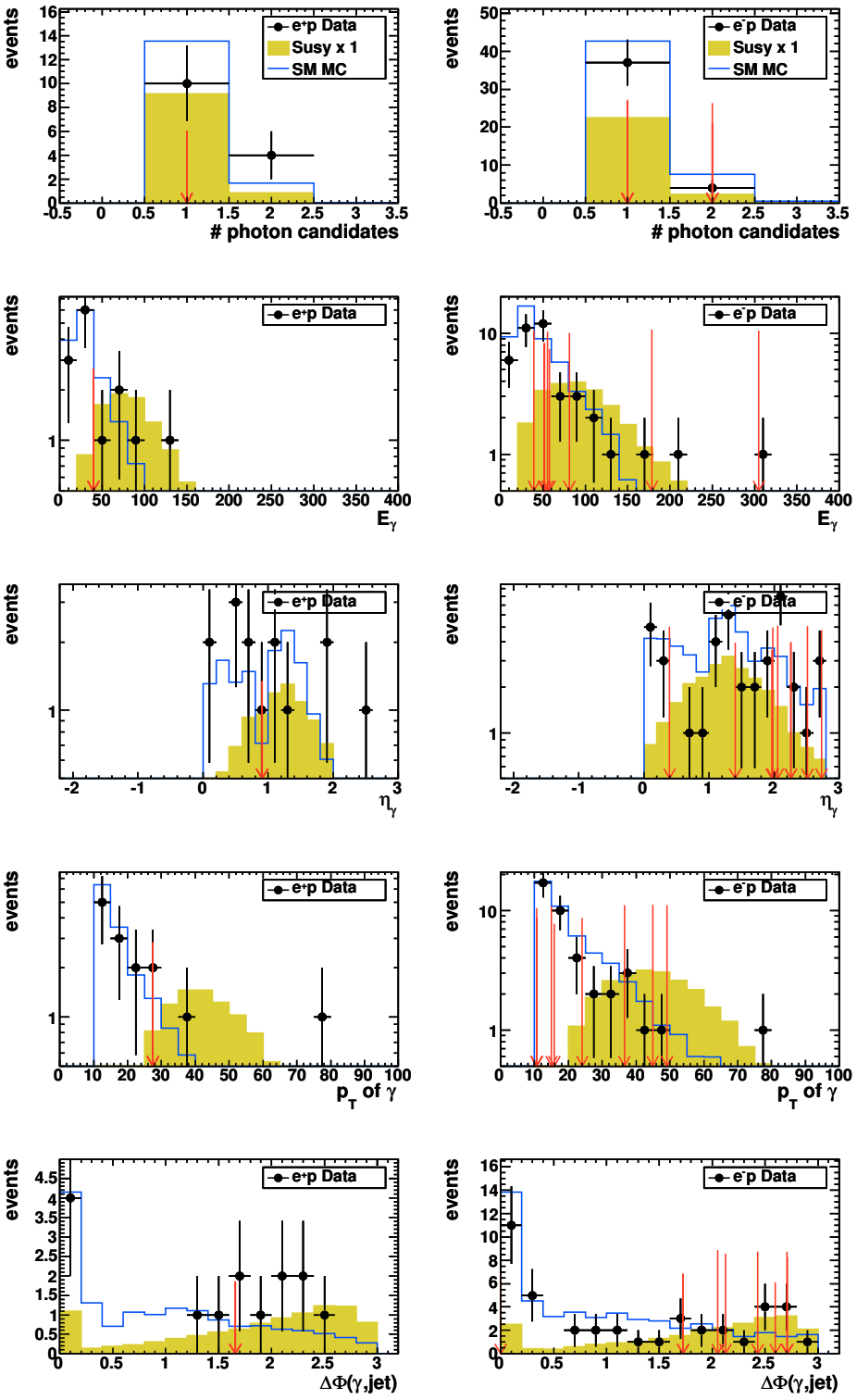

Figure 9.11: Arrows mark events with discriminant value D greater than 0.8. Arrow length is proportional to D^2.

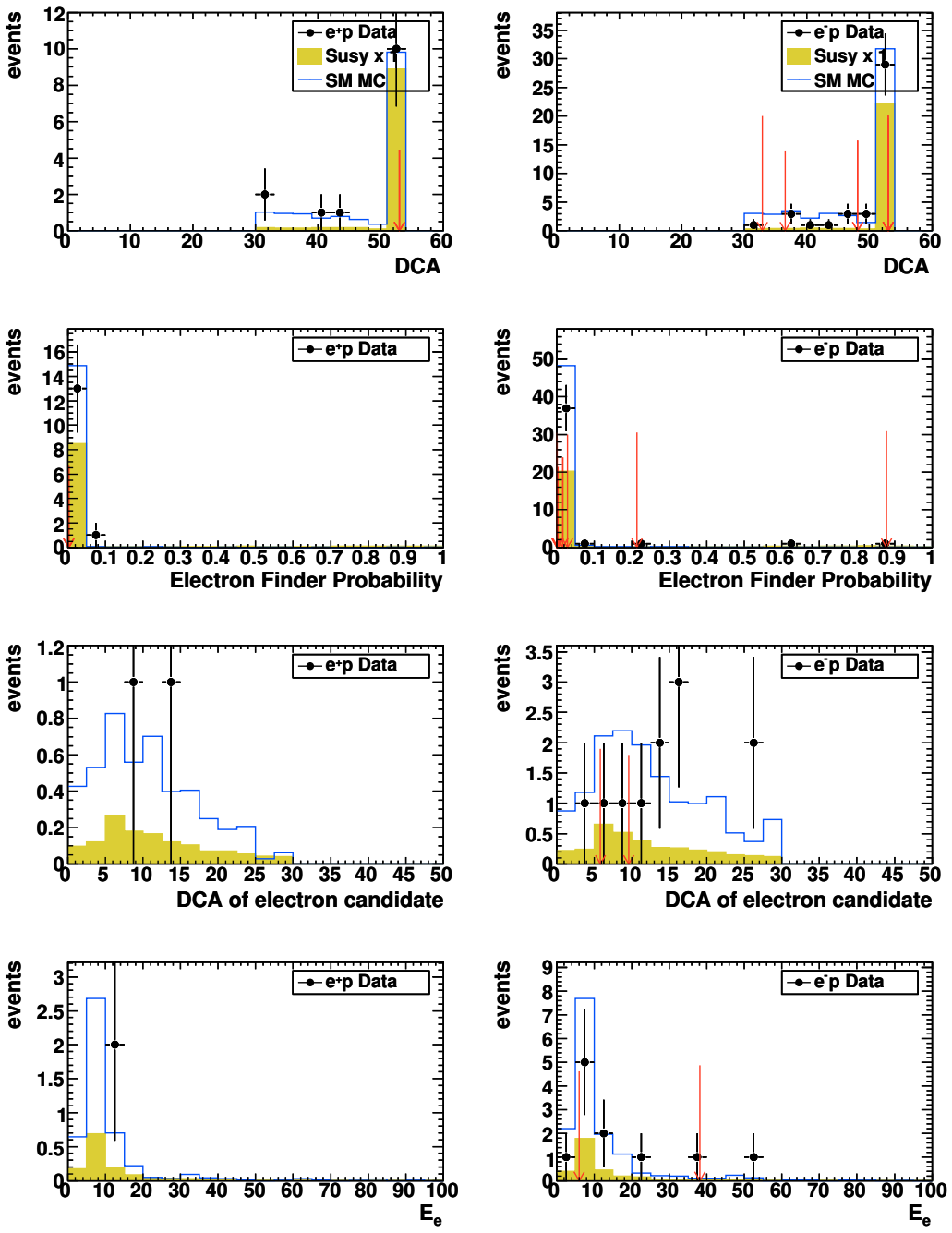

Figure 9.12: Arrows mark events with discriminant value D greater than 0.8. Arrow length is proportional to D^2.

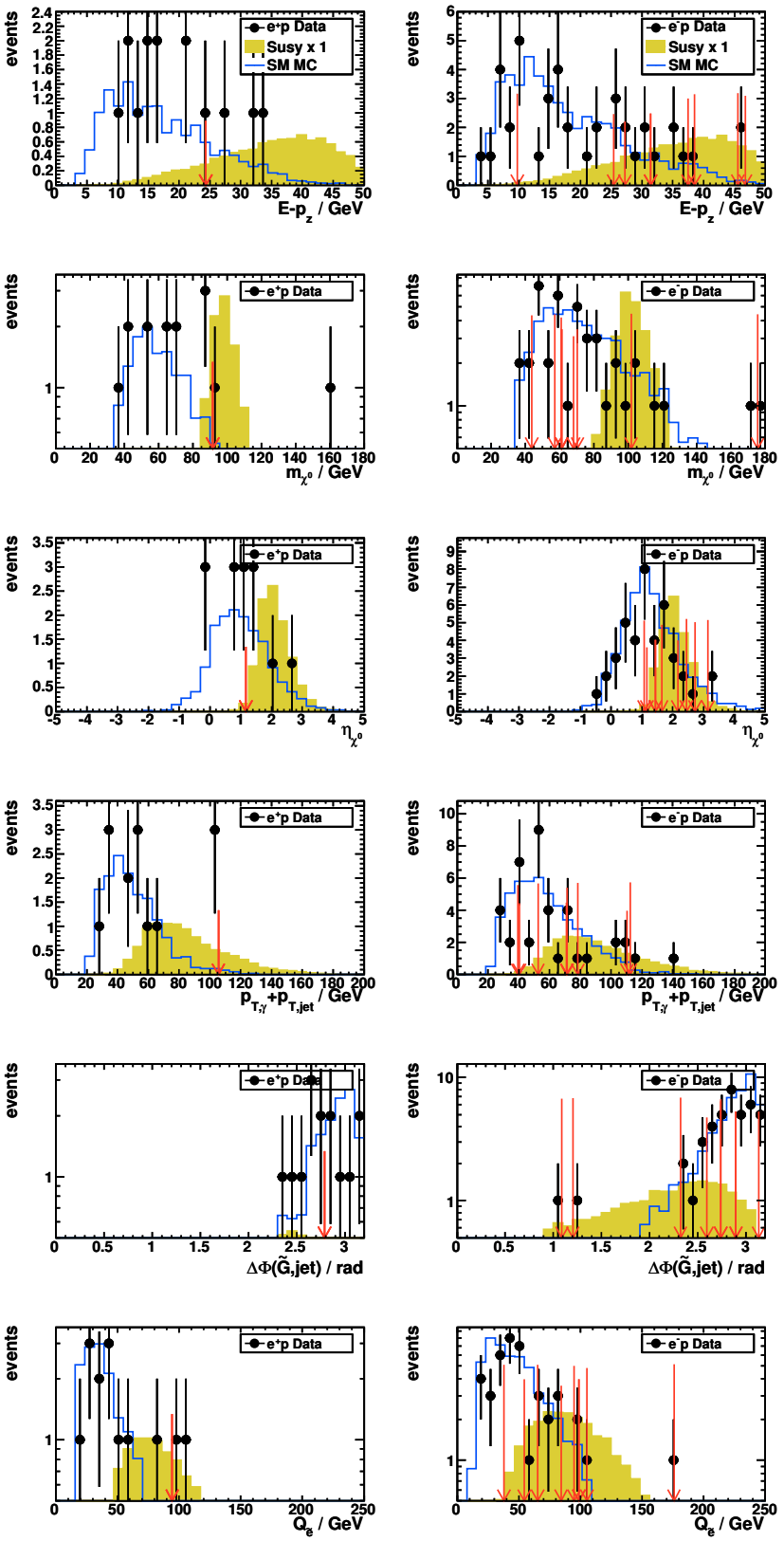

Figure 9.13: Arrows mark events with discriminant value D greater than 0.8. Arrow length is proportional to D^2.

Chapter 10

Limit Calculation

10.1 Modified Frequentist Confidence Levels

To set limits on parameters and observables of the SUSY model the modified frequentist approach (also called CL_s technique) [86], which is implemented in the ROOT [56] class TLimit, is used. It is an efficient method for calculating approximate 95% confidence levels (CL). It allows the inclusion of statistical and systematic uncertainties and the combination of several channels in the case of low statistics.

To discriminate signal-like outcomes from background-like ones, for every channel i the likelihood ratio

$$X_i(d_i) = \frac{e^{-(s_i+b_i)}(s_i+b_i)_i^d}{d_i!} / \frac{e^{-b_i} b_i^{d_i}}{d_i!} \tag{10.1}$$

is calculated from the number of observed candidates d_i, and the number of expected signal and background events, s_i and b_i. This test statistics increases monotonically with the number of candidates d_i.

The total likelihood ratio for n channels (or bins) is the product of the test statistics for the single channels,

$$X(d) = \prod_{i=1}^{n} X_i(d_i), \tag{10.2}$$

where $d = (d_0, \ldots, d_n)$ is the collection of all data channels.

To exclude a signal, we are interested in the probability $P_{s+b}(X \leq X_{\text{obs}})$ that in the presence of a signal the test statistics is equal to or less than the observed test statistics. This probability is the sum of Poisson probabilities

$$P_{s+b}(X \leq X_{\text{obs}}) = \sum_{\substack{d' \\ X(d') \leq X(d)}} \prod_{i=1}^{n} \frac{e^{-(s_i+b_i)}(s_i+b_i)^{d'_i}}{d'_i!}. \tag{10.3}$$

for the individual outcomes. The probability $P_b(X \leq X_{\text{obs}})$ for only the background hypothesis is defined analogously.

With the ratio of these probabilities the confidence level for excluding the signal hypothesis is given by

$$\text{CL} = 1 - \frac{P_{s+b}}{P_b}. \tag{10.4}$$

This definition of a confidence level has the preferable property that it takes also the confidence level for the background hypothesis into account, especially in cases

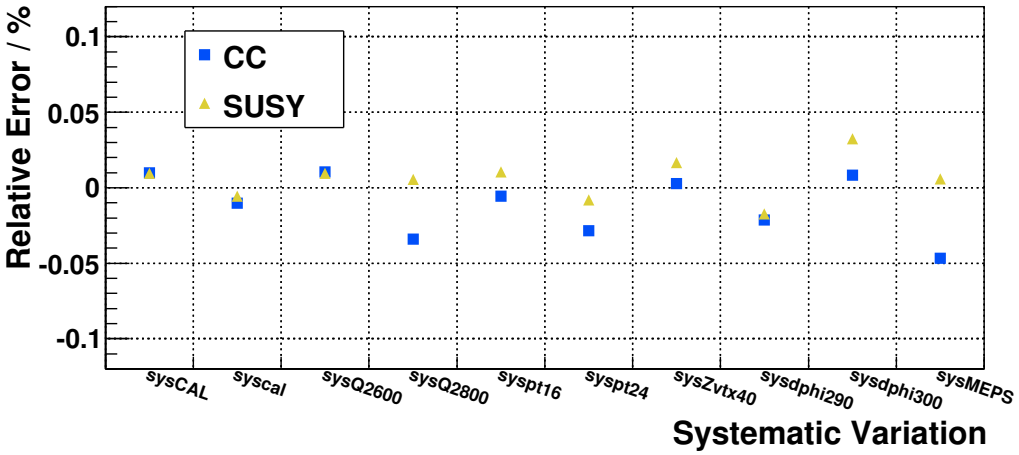

Figure 10.1: Sources of Systematic Uncertainties. sysCAL (syscal) denotes the greatest positive (negative) energy scale uncertainty, sysQ2600 (sysQ2800) the change of the Q^2 cut 100 GeV^2 down (up), syspt16 (syspt24) the change of the missing p_T cut 4 GeV down (up), sysZvtx40 the 10 cm relaxing of the Z-vertex cut, sysdphi290 (sysdphi300) the change of the $\Delta\phi(\gamma, \text{jet}$ cut 50 mrad down (up), and sysMEPS denotes the change of the QCD radiation model to MEPS.

where the number of events is small and due to statistical fluctuations beneath the expected background level. In some respects this is a Bayesian modification of frequentist confidence levels [87].

Instead of computing all the $\mathcal{O}(n^m)$ terms of Equation (10.3), which is not affordable for large numbers of channels n and possible outcomes m, a Monte Carlo approach, selecting representative outcomes of the experiment and comparing them with the actual data, is used to approximate the confidence level.

Sources of systematic uncertainties are included by assuming the number of signal and background events to be Gaussian distributed (with a cut-off at zero), with a width $\sigma_j^{s/b}$ for uncertainty j.

10.2 Systematic Uncertainties

There are different sources of systematic uncertainties that have to be taken into account when calculating limits. These are uncertainties in the detector calibration, in the theory and in the Monte Carlo simulation.

10.2.1 Calorimeter Energy Scale

The uncertainty in the hadronic energy scale was estimated to be 1% in the FCAL and BCAL, and 2% in the RCAL, while the relative uncertainty between the hadronic and electromagnetic energy scales was estimated to be 2% [88].

Therefore, the following variations were applied in the MC samples to all calorimeter cells, except for the cells that belong to the photon candidate:

1. FCAL energy $\pm 1\%$, BCAL energy $\pm 1\%$, RCAL energy $\pm 2\%$,

2. FCAL energy $\pm 1\%$, BCAL energy $\mp 1\%$, RCAL energy $\pm 2\%$,

Data set	Polarisation	$\Delta\sigma/\sigma$
left handed e^+p	-0.37	1.1%
right handed e^+p	0.32	2.5%
left handed e^-p	-0.27	0.9%
right handed e^-p	0.31	1.8%

Table 10.1: Polarisation and relative systematic error on the CC DIS cross section due to the polarisation measurement.

3. FCAL EMC energy $\pm 2\%$, FCAL HAC energy $\mp 2\%$,
4. BCAL EMC energy $\pm 2\%$, BCAL HAC energy $\mp 2\%$,
5. RCAL EMC energy $\pm 2\%$, RCAL HAC energy $\mp 2\%$.

To determine the influence of the calorimeter energy scale uncertainty, the relative changes in the most significant discriminant distribution bins due to these variations were evaluated.

The results are shown in Figure 10.1.

10.2.2 Luminosity and Polarisation Measurement

Polarisation: To weight the cross section of the CC DIS Monte Carlo, the polarisation of the data had to be taken into account. This measurement is described in section 3.1.1. Both LPOL and TPOL measurement are not available for all data. To maximise the available luminosity, for each run the polarimeter with a longer up-time was selected. To determine the systematic uncertainty in a conservative way, the TPOL error is used to determine the systematic uncertainty due to the polarisation measurement.

The obtained relative uncertainties are listed in Table 10.1. They result in a uncertainty of 1.9% for e^+p CC data and 1.3% for e^-p CC data.

For the SUSY signal cross section the polarisation influence can be neglected, because the neutralino is expected to be photino-like (see Section 7.1) and thus will exhibit only weak polarisation dependence, if any at all, taking into account that left handed and right handed polarisation are distributed almost evenly in the data.

Luminosity: The uncertainty on the luminosity measurement is estimated to be 2.6% (see Section 3.2.5).

10.2.3 Model Uncertainties

Hadronisation: The analysis depends on details of the simulation of the hadronic final state. To estimate the corresponding uncertainty the LEPTO MEPS model was used instead of the ARIADNE CDM model (see Section 6.1.3) in the Monte Carlo simulation. Then the relative change of the discriminant distribution was evaluated.

Signal cross section: The signal cross section was calculated only at leading order. Since no NLO generators are available for the signal process, the cross section

Source of uncertainty	Background	Signal
Signal cross section	-	10%
SUSY mass interpolation	-	10%
PDF	7%	7%
Hadronisation	4.7%	-
Luminosity	2.6%	2.6%
Polarisation	1.6%	-
Energy scale	1.0%	0.8%
Q^2 cut	3.4%	1.0%
Z_{vtx} cut	0.3%	1.7%
p_T cut	2.8%	1.1%
$\Delta\phi(\gamma, \text{jet})$ cut	2.1%	3.3%
Total	10.3%	16.5%

Table 10.2: Summary of systematic uncertainties for background and signal.

uncertainty was estimated by changing the energy scale for the PDF evaluation ($\sqrt{\hat{s}}$, $\sqrt{Q^2}$, $\sqrt{\hat{p}_T^2}$) in SUSYGEN and additionally by using CompHEP instead. All results differ by less than 10%, so a systematic uncertainty of 10% was estimated, which is in line with typical NLO corrections.

Parton Density Function: The uncertainty on the u quark PDF is estimated to be 3%, and 7% on the d quark.

10.2.4 Limit Setting

Another source of uncertainty comes from the limit setting procedure, where the discriminant distributions for most parameter points were interpolated from a grid of generated parameter points. This uncertainty is estimated to be 10%.

10.2.5 Cut Variations

To check for threshold effects, some cuts were varied.

Q^2 cut variation: The cut on $Q^2 > 700\,\text{GeV}^2$ was varied by $\pm 100\,\text{GeV}^2$.

p_T cut variation: The cut on the missing $p_T > 20\,\text{GeV}$ was varied by $\pm 4\,\text{GeV}$.

$\Delta\phi(\gamma, \text{jet})$ cut variation: The cut on the azimuthal angle difference between the photon candidate and the leading jet, $\Delta\phi(\gamma, \text{jet}) < 2.95$, was varied by an amount of $\pm 0.05\,\text{rad}$.

Z_{vtx} cut variation: The cut on the z position of the vertex, $|Z_{\text{vtx}}| < 30\,\text{cm}$, was relaxed to 40 cm.

10.2.6 Summary of Systematic Uncertainties

Table 10.2 summarises the systematic uncertainties for signal and background.

The total systematic uncertainty is the quadratic sum of the single uncertainties. It amounts to 10.3% for the background and 16.5% for the signal.

10.3 Limits on Model Parameters

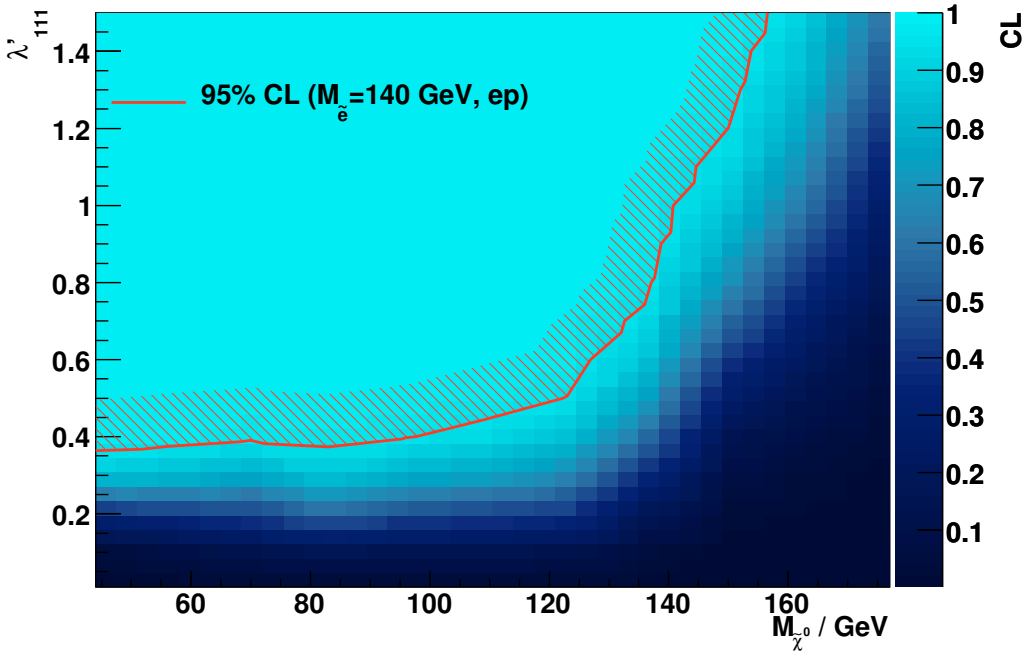

Figure 10.2: Combined limits for e^+p and e^-p on the R-parity violating coupling parameter λ'_{111} in dependence of the neutralino mass for the parameter space point with $m_{\tilde{e}} = 140\,\text{GeV}$.

Figure 10.2 shows the limit on the R-parity violating coupling λ'_{111}, which can be derived for a single parameter space point as a function of the neutralino mass $m_{\tilde{\chi}^0}$. For this scan, the SUSY breaking scale Λ, which directly determines $m_{\tilde{\chi}^0}$ (see Figure 7.5), was varied in steps of 10 TeV. Although Λ is a fundamental GMSB parameter, the limit curve is displayed as a function of the neutralino mass, which is a physical observable. This facilitates comparison with other theoretical and experimental results.

For greater values of $m_{\tilde{\chi}^0}$, the cross section decreases roughly exponentially, and it increases quadratically with λ'_{111}, so that R-parity violating couplings of electroweak strength,

$$\lambda'_{111} = \sqrt{4\pi\alpha} \approx 0.3,$$

where α is the fine structure constant, can only be excluded at low neutralino and selectron masses.

Figure 10.3 shows limits in the $m_{\tilde{\chi}^0}$- $m_{\tilde{e}}$ plane. For $\lambda'_{111} = 1$ and realistic selectron masses (see Section 7.3), neutralino masses up to 190 GeV can be excluded. Selectron masses up to 300 GeV (at $m_{\tilde{\chi}^0} = 85\,\text{GeV}$) can be excluded.

At lower neutralino masses a slight excess of SUSY candidates over the background estimation (see Section 9.6) erodes the limits on the selectron mass.

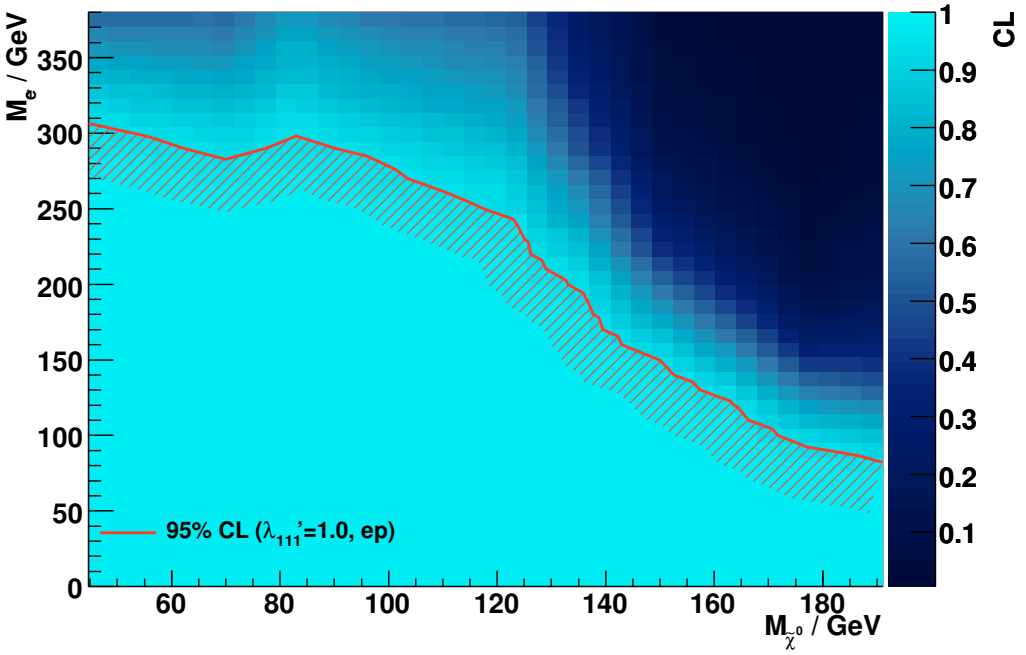

Figure 10.3: Combined limits for e^+p and e^-p in the plane of neutralino and selectron masses for $\lambda'_{111} = 1$. The region underneath the line is excluded at 95% confidence level.

Chapter 11

Conclusion and Outlook

11.1 Summary

On the technical, detector-related side, an optimisation of the clustering procedure for hits in the Micro Vertex Detector MVD at the ZEUS experiment was performed, which used information from the pattern recognition phase of the tracking chain. As summarised in Chapter 5, it led to an resolution improvement of up to 20%.

On the physics side, a search for events with a supersymmetry-signature of a gravitino, a photon and at least one jet in electron-proton collisions with a centre of mass energy of 318 GeV has been carried out with the ZEUS detector at HERA using a data set with an integrated luminosity of $325.7\,\mathrm{pb}^{-1}$. This signature is predicted by the Gauge Mediated Supersymmetry Breaking (GMSB) model with an R-parity violating coupling λ'_{11k} for some parts of the parameter space where a neutralino (produced via t-channel exchange of a selectron between electron and quark) decays into a gravitino and a photon inside the detector.

After the selection of events with a high-energetic isolated photon, large missing transverse momentum and a high-energetic jet, 1352 data events remained, while 1396 ± 37 were expected from the Standard Model prediction. The number of expected SUSY events depends on the chosen parameter point. For a neutralino mass of 96 GeV, a selectron mass of 140 GeV and a R-parity violating coupling $\lambda'_{111} = 1$, 39 events were expected. Because this number is of the order of the statistical uncertainty of the Standard Model expectation, the signal-to-background ratio was improved with additional cuts and the help of a multivariate data analysis technique. The resulting discriminant distribution still showed no significant evidence of signal events in the data. Thus, exclusion limits at 95% confidence level were derived for different neutralino masses, selectron masses and R-parity violating couplings. Selectron masses of up to 300 GeV could be excluded (for an R-parity violating coupling $\lambda'_{111} = 1$ and a neutralino mass $m_{\tilde{\chi}^0} = 85\,\mathrm{GeV}$).

The obtained limits are slightly weaker than those from a previous analysis [4] of a different and older subset of HERA data which was partially not used in this analysis. This difference is strongest in the region of neutralino masses less than 70 GeV and stems from the fact that the newer analysis found a slight overshoot of candidates with a high discriminant value. The nature of these events remains unclear.

11.2 Outlook

The presented limits could in principal be slightly improved by including the data from the HERA I running period (1994–2000). However, the integrated luminosity of this data taking period is much smaller and would not contribute much. These data have been analysed before [4] without finding a signal, so a discovery is not to be expected.

The analysis could be further improved by combining the ZEUS data with the H1 data, amounting to an integrated luminosity of almost $1\,\mathrm{fb}^{-1}$. Such a combination has been undertaken before, e.g. in the search for events with isolated leptons and missing transverse momentum [89]. In that search as well as in a model-independent search for new phenomena at HERA by the H1 collaboration [90], no significant evidence for physics beyond the standard model was observed. This suggests, that a combination with the H1 data can only set more exclusive limits. A SUSY discovery in seems unlikely.

Nevertheless, there is the hope that at the Large Hadron Collider LHC, which has started operation in the late autumn of 2009 and will increase its centre of mass energy to 7 TeV soon, finally clear evidence of SUSY will be found. Under the assumption that SUSY solves some of the problems of the Standard Model mentioned in Chapter 2.1.2, a SUSY discovery seems almost inevitable.

However, the LHC will not be sensitive enough to determine the exact SUSY breaking scenario that is realised in nature. For this a cleaner initial state, like e^+e^-, with appropriate detectors, is mandatory. The main competing projects for this task are the International Linear Collider (ILC) [91], for which a Reference Design Report [92] exits and for which a collision energy of at least 500 GeV are planned, and the Compact Linear Collider (CLIC) [93], which is still in the R&D phase and could achieve 3 TeV collisions.

Appendix A

MVD Clustering: Supplemental Information

A.1 Conventions

A local coordinate system is defined for each sensor A.1. x' is the measurement direction, y' the normal direction to the sensor and z' is defined to complete a right-handed coordinate system.

By projecting a track onto the $x'z'$ plane and taking the angle between the track projection and the z' axis, we get the incident angle θ.

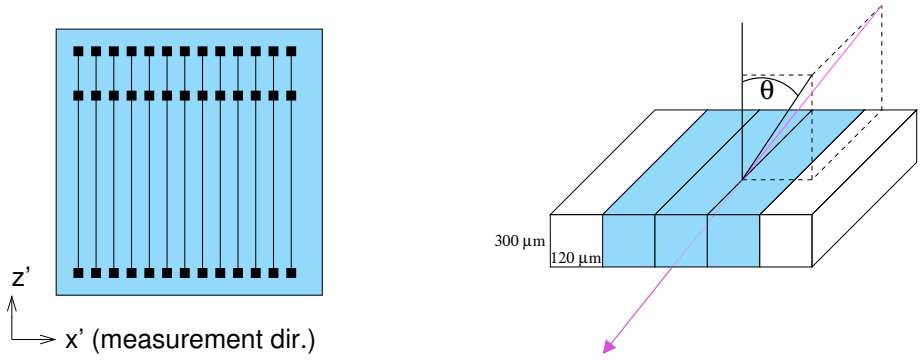

Figure A.1: Local sensor coordinate system for sensors.

A.2 Expected Width

With the impact angle θ as defined in Figure A.1 and the quotient of sensor thickness t and readout pitch p the expected width w of the cluster in number of readout strips can be calculated:

$$w = w_0 + t/p \tan\theta \tag{A.1}$$

w_0 is an offset that takes into account that due to the strip coupling even for perpendicular impact at least one strip fires.

The resulting dependence of the expected width in readout strips on the impact angle is shown in Figure A.2.

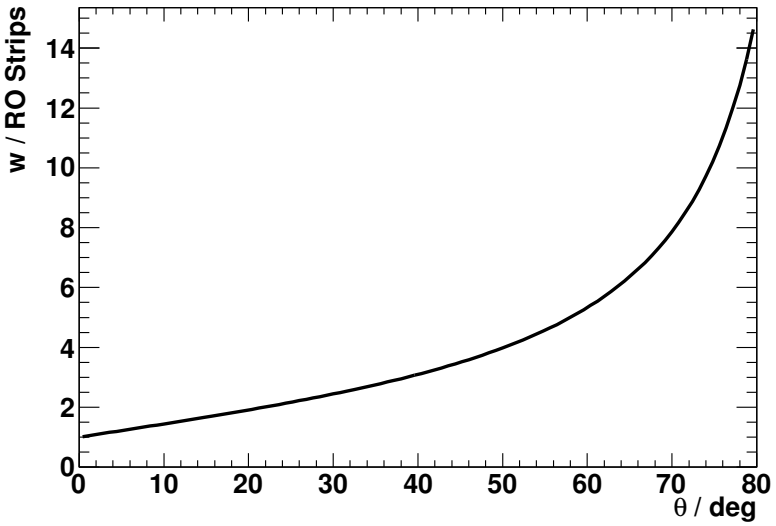

Figure A.2: Expected width (for $w_0 = 1$) as a function of the impact angle.

A.3 Eta Algorithm

Figure A.3 shows η distributions for different sensor positions.

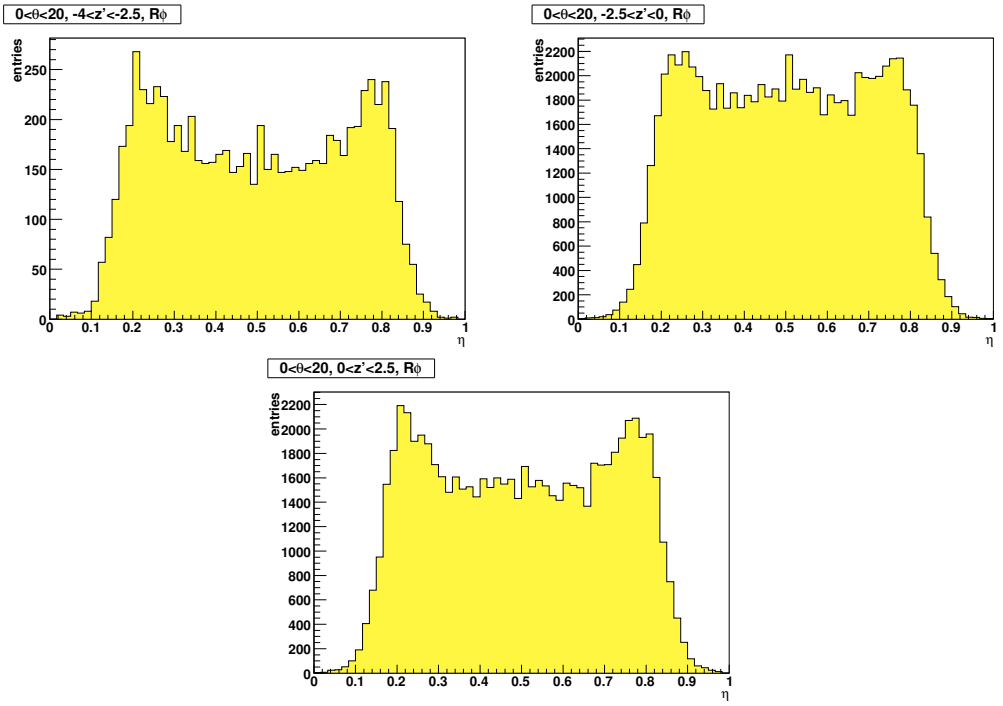

Figure A.3: η distributions for different hit positions z' on the sensor: $-4\,\mathrm{cm} < z' < -2.5\,\mathrm{cm}$ (top left), $-2.5\,\mathrm{cm} < z' < 0\,\mathrm{cm}$ (top right), $0\,\mathrm{cm} < z' < 2.5\,\mathrm{cm}$ (bottom).

A.4 Steering Cards

A.4.1 Initial Clustering

`MVRECO-POSALG A1 A2`

`A1` chooses clustering algorithm for clusters < 3 readout strips above threshold

`A2` for wider clusters.

Possible values for `A1` and `A2`:

1: Centre of Gravity algorithm (default if card not used)

2: 3-Strip algorithm

3: Head-Tail-Fusion algorithm

A.4.2 Post Pattern Recognition Reclustering

QX Algorithm

The QX reclustering is on by default. It can be switched of by setting
`VCRECO-VCMVTES 0`

Eta Algorithm

`MVRECO-DORECLUS B`
Possible values for `B`:

0: no reclustering

1: η algorithm for $|\theta| < 40°$, else Head-Tail-Fusion

2: η algorithm

3: 3-Strip algorithm

4: Sub-Threshold Centre of Gravity algorithm

5: Head-Tail-Fusion algorithm

6: η algorithm for $|\theta| < 40°$, else ZTRECC is not touched (which means that in the default case QX is used)

The last option (6) is the default is this control card is not used.

Appendix B

SUSY Search: Supplemental Information

B.1 Trigger Selection

The following trigger slots were required:

- FLT: 60 or 63 or 39 or 40 or 41 or 43 or 44,
- SLT: EXO4,
- TLT: EXO2 or EXO6,
- DST34.

B.2 Timing Cut

Because the timing is not properly simulated in the Monte Carlo, this cut is applied to data only.

Events that do not fulfil the following conditions are rejected:

$$|t_\mathrm{F}| < 6\,\mathrm{ns} \vee E_\mathrm{F} \leq 0.6\,\mathrm{GeV} \vee n_\mathrm{F} < 2 \vee t_\mathrm{F} = -100\,\mathrm{ns}, \tag{B.1a}$$

$$(t_\mathrm{F} > -5\,\mathrm{ns} \wedge t_\mathrm{F} < 4\,\mathrm{ns}) \vee E_\mathrm{F} \leq 3\,\mathrm{GeV} \vee n_\mathrm{F} < 2 \vee t_\mathrm{F} = -100\,\mathrm{ns}, \tag{B.1b}$$

$$|t_\mathrm{B}| < 6\,\mathrm{ns} \vee E_\mathrm{B} \leq 2\,\mathrm{GeV} \vee n_\mathrm{B} < 2 \vee t_\mathrm{B} = -100\,\mathrm{ns}, \tag{B.1c}$$

$$(t_\mathrm{B} > -4\,\mathrm{ns} \wedge t_\mathrm{B} < 5\,\mathrm{ns}) \vee E_\mathrm{B} \leq 4\,\mathrm{GeV} \vee n_\mathrm{B} < 2 \vee t_\mathrm{B} = -100\,\mathrm{ns}, \tag{B.1d}$$

$$|t_\mathrm{R}| < 6\,\mathrm{ns} \vee E_\mathrm{R} \leq 2\,\mathrm{GeV} \vee n_\mathrm{R} < 2 \vee t_\mathrm{R} = -100\,\mathrm{ns}, \tag{B.1e}$$

$$|t_\mathrm{R}| < 5\,\mathrm{ns} \vee E_\mathrm{R} \leq 4\,\mathrm{GeV} \vee n_\mathrm{R} < 2 \vee t_\mathrm{R} = -100\,\mathrm{ns}, \tag{B.1f}$$

$$(t_\mathrm{g} > -5\,\mathrm{ns} \wedge t_\mathrm{g} < 4\,\mathrm{ns}) \vee E_\mathrm{g} \leq 0.6\,\mathrm{GeV} \vee n_\mathrm{g} < 2 \vee t_\mathrm{g} = -100\,\mathrm{ns}, \tag{B.1g}$$

$$(t_\mathrm{u} > -5\,\mathrm{ns} \wedge t_\mathrm{u} < 5\,\mathrm{ns}) \vee E_\mathrm{u} \leq 3\,\mathrm{GeV} \vee n_\mathrm{u} < 2 \vee t_\mathrm{u} = -100\,\mathrm{ns}, \tag{B.1h}$$

$$(t_\mathrm{d} > -7\,\mathrm{ns} \wedge t_\mathrm{d} < 5\,\mathrm{ns}) \vee E_\mathrm{d} \leq 4\,\mathrm{GeV} \vee n_\mathrm{d} < 2 \vee t_\mathrm{d} = -100\,\mathrm{ns}, \tag{B.1i}$$

$$\begin{aligned}\big((t_\mathrm{F} - t_\mathrm{R}) > -8\,\mathrm{ns} \wedge (t_\mathrm{F} - t_\mathrm{R}) < 4\,\mathrm{ns}\big) \vee E_\mathrm{F} \leq 2\,\mathrm{GeV} \vee E_\mathrm{R} \leq 2\,\mathrm{GeV} \\ \vee n_\mathrm{F} < 2 \vee n_\mathrm{R} < 2 \vee t_\mathrm{F} = -100\,\mathrm{ns} \vee t_\mathrm{R} = -100\,\mathrm{ns},\end{aligned} \tag{B.1j}$$

$$\begin{aligned}\big((t_\mathrm{u} - t_\mathrm{d}) > -7\,\mathrm{ns} \wedge (t_\mathrm{u} - t_\mathrm{d}) < 6\,\mathrm{ns}\big) \vee E_\mathrm{u} \leq 3\,\mathrm{GeV} \vee E_\mathrm{d} \leq 3\,\mathrm{GeV} \\ \vee n_\mathrm{u} < 2 \vee n_\mathrm{d} < 2 \vee t_\mathrm{u} = -100\,\mathrm{ns} \vee t_\mathrm{d} = -100\,\mathrm{ns}.\end{aligned} \tag{B.1k}$$

Here $t_{F,B,R}$ are the FCAL, BCAL and RCAL times, $t_{g,u,d}$ the global time, the global upper time and the global lower time. All times are the relative times with respect

to the nominal ep interaction times. E_i is the energy used for the time average, and n_i is the number of photo-multiplier tubes uses for the time (the meaning of i is the same as in t_i).

Bibliography

[1] S. R. Coleman and J. Mandula, "ALL POSSIBLE SYMMETRIES OF THE S MATRIX," *Phys. Rev.* **159** (1967) 1251–1256.

[2] R. Haag, J. T. Lopuszanski, and M. Sohnius, "All Possible Generators of Supersymmetries of the s Matrix," *Nucl. Phys.* **B88** (1975) 257.

[3] H. P. Nilles, "Supersymmetry, Supergravity and Particle Physics," *Phys. Rept.* **110** (1984) 1–162.

[4] C. Horn, "Search for gravitinos in R-parity violating supersymmetry at HERA,". DESY-THESIS-2006-019.

[5] C. N. Nguyen, "Search for gaugino production in R-parity violating supersymmetry with the ZEUS detector at HERA,". DESY-THESIS-2005-043.

[6] I. Brock *et al.*, "The design and performance of the ZEUS Micro Vertex detector," *Nucl. Instrum. Meth.* **A581** (2007) 656–686, 0708.3011.

[7] E. Belau *et al.*, "THE CHARGE COLLECTION IN SILICON STRIP DETECTORS," *Nucl. Instr. Meth.* **214** (1983) 253.

R. Turchetta, "Spatial resolution of silicon microstrip detectors," *Nucl. Instrum. Meth.* **A335** (1993) 44–58.

U. Kotz *et al.*, "SILICON STRIP DETECTORS WITH CAPACITIVE CHARGE DIVISION," *Nucl. Instr. Meth.* **A235** (1985) 481.

[8] S. L. Glashow, "Partial Symmetries of Weak Interactions," *Nucl. Phys.* **22** (1961) 579–588.

A. Salam, "Renormalizability of gauge theories," *Phys. Rev.* **127** (1962) 331–334.

S. Weinberg, "A Model of Leptons," *Phys. Rev. Lett.* **19** (1967) 1264–1266.

[9] P. W. Higgs, "Spontaneous Symmetry Breakdown Without Massless Bosons," *Phys. Rev.* **145** (1966) 1156–1163.

P. W. Higgs, "BROKEN SYMMETRIES AND THE MASSES OF GAUGE BOSONS," *Phys. Rev. Lett.* **13** (1964) 508–509.

[10] U. Amaldi, W. de Boer, and H. Furstenau, "Comparison of grand unified theories with electroweak and strong coupling constants measured at LEP," *Phys. Lett.* **B260** (1991) 447–455.

[11] L. Susskind, "THE GAUGE HIERARCHY PROBLEM, TECHNICOLOR, SUPERSYMMETRY, AND ALL THAT. (TALK)," *Phys. Rept.* **104** (1984) 181–193.

[12] **WMAP** Collaboration, E. Komatsu *et al.*, "Five-Year Wilkinson Microwave Anisotropy Probe (WMAP) Observations: Cosmological Interpretation," *Astrophys. J. Suppl.* **180** (2009) 330–376, 0803.0547.

D. Clowe *et al.*, "A direct empirical proof of the existence of dark matter," *Astrophys. J.* **648** (2006) L109–L113, astro-ph/0608407.

F. Zwicky, "On the Masses of Nebulae and of Clusters of Nebulae," *Astrophys. J.* **86** (1937) 217–246.

[13] J. R. Primack, "Dark matter and structure formation," astro-ph/9707285.

[14] **Super-Kamiokande** Collaboration, S. Fukuda *et al.*, "Tau neutrinos favored over sterile neutrinos in atmospheric muon neutrino oscillations," *Phys. Rev. Lett.* **85** (2000) 3999–4003, hep-ex/0009001.

SNO Collaboration, Q. R. Ahmad *et al.*, "Measurement of the charged current interactions produced by B-8 solar neutrinos at the Sudbury Neutrino Observatory," *Phys. Rev. Lett.* **87** (2001) 071301, nucl-ex/0106015.

[15] S. Weinberg, "The cosmological constant problem," *Rev. Mod. Phys.* **61** (1989) 1–23.

[16] A. D. Sakharov, "Violation of CP Invariance, c Asymmetry, and Baryon Asymmetry of the Universe," *Pisma Zh. Eksp. Teor. Fiz.* **5** (1967) 32–35.

[17] M. Kobayashi and T. Maskawa, "CP Violation in the Renormalizable Theory of Weak Interaction," *Prog. Theor. Phys.* **49** (1973) 652–657.

[18] A. Riotto, "Theories of baryogenesis," hep-ph/9807454.

[19] R. P. Woodard, "How Far Are We from the Quantum Theory of Gravity?," 0907.4238.

[20] R. Devenish and A. Cooper-Sarkar, "Deep inelastic scattering,". Oxford, UK: Univ. Pr. (2004) 403 p.

[21] J. Wess and J. Bagger, "Supersymmetry and supergravity,". Princeton, USA: Univ. Pr. (1992) 259 p.

[22] S. Dimopoulos and D. W. Sutter, "The Supersymmetric flavor problem," *Nucl. Phys.* **B452** (1995) 496–512, hep-ph/9504415.

D. W. Sutter, "The Supersymmetric flavor problem and $\mu \to e^+\gamma$," hep-ph/9704390.

[23] M. B. Green, J. H. Schwarz, and E. Witten, "SUPERSTRING THEORY. VOL. 1: INTRODUCTION,". Cambridge, Uk: Univ. Pr. (1987) 469 P. (Cambridge Monographs On Mathematical Physics).

M. B. Green, J. H. Schwarz, and E. Witten, "SUPERSTRING THEORY. VOL. 2: LOOP AMPLITUDES, ANOMALIES AND PHENOMENOLOGY,". Cambridge, Uk: Univ. Pr. (1987) 596 P. (Cambridge Monographs On Mathematical Physics).

[24] P. Athron and . Miller, D. J., "A New Measure of Fine Tuning," *Phys. Rev.* **D76** (2007) 075010, 0705.2241.

[25] F. Takayama and M. Yamaguchi, "Gravitino dark matter without R-parity," *Phys. Lett.* **B485** (2000) 388–392, hep-ph/0005214.

W. Buchmuller, L. Covi, K. Hamaguchi, A. Ibarra, and T. Yanagida, "Gravitino dark matter in R-parity breaking vacua," *JHEP* **03** (2007) 037, hep-ph/0702184.

[26] D. Stockinger, "(g - 2)(mu) and physics beyond the Standard Model," *Nucl. Phys. Proc. Suppl.* **181-182** (2008) 32–36.

[27] M. Misiak *et al.*, "The first estimate of B(anti-B –> X/s gamma) at O(alpha(s)**2)," *Phys. Rev. Lett.* **98** (2007) 022002, hep-ph/0609232.

T. Becher and M. Neubert, "Analysis of Br(B –> X/s gamma) at NNLO with a cut on photon energy," *Phys. Rev. Lett.* **98** (2007) 022003, hep-ph/0610067.

[28] M. Ciuchini, E. Franco, A. Masiero, and L. Silvestrini, "b –> s transitions: A new frontier for indirect SUSY searches," *Phys. Rev.* **D67** (2003) 075016, hep-ph/0212397.

T. Hurth, "Present status of inclusive rare B decays," *Rev. Mod. Phys.* **75** (2003) 1159–1199, hep-ph/0212304.

[29] G. F. Giudice and R. Rattazzi, "Theories with gauge-mediated supersymmetry breaking," *Phys. Rept.* **322** (1999) 419–499, hep-ph/9801271.

[30] V. D. Barger, M. S. Berger, and P. Ohmann, "Supersymmetric grand unified theories: Two loop evolution of gauge and Yukawa couplings," *Phys. Rev.* **D47** (1993) 1093–1113, hep-ph/9209232.

[31] V. D. Barger, G. F. Giudice, and T. Han, "Some New Aspects of Supersymmetry R-Parity Violating Interactions," *Phys. Rev.* **D40** (1989) 2987.

R. Barbier *et al.*, "R-parity violating supersymmetry," *Phys. Rept.* **420** (2005) 1–202, hep-ph/0406039.

[32] M. Hirsch, H. V. Klapdor-Kleingrothaus, and S. G. Kovalenko, "New constraints on R-parity broken supersymmetry from neutrinoless double beta decay," *Phys. Rev. Lett.* **75** (1995) 17–20.

M. Chemtob, "Phenomenological constraints on broken R parity symmetry in supersymmetry models," *Prog. Part. Nucl. Phys.* **54** (2005) 71–191, hep-ph/0406029.

[33] G. A. Voss and B. H. Wiik, "The Electron proton collider HERA," *Ann. Rev. Nucl. Part. Sci.* **44** (1994) 413–452.

[34] M. Seidel, "The upgraded interaction regions of HERA,". DESY-HERA-00-01.

e. . Schneekloth, U., "The HERA luminosity upgrade,". DESY-HERA-98-05.

[35] A. A. Sokolov and I. M. Ternov, "On Polarization and spin effects in the theory of synchrotron radiation," *Sov. Phys. Dokl.* **8** (1964) 1203–1205.

[36] U. H. e. ZEUS Coll., "The ZEUS Detector,". Status Report (unpublished), DESY (1993), available on `http://www-zeus.desy.de/bluebook/bluebook.html`.

[37] D. G. Cussans *et al.*, "The Design, status and performance of the ZEUS central tracking detector electronics," *Nucl. Instrum. Meth.* **A315** (1992) 397–403.

B. Foster *et al.*, "The Performance of the Zeus central tracking detector z-by-timing electronics in a transputer based data acquisition system," *Nucl. Phys. Proc. Suppl.* **32** (1993) 181–188.

ZEUS Collaboration, B. Foster *et al.*, "The Design and construction of the ZEUS central tracking detector," *Nucl. Instrum. Meth.* **A338** (1994) 254–283.

[38] M. Derrick *et al.*, "Design and construction of the ZEUS barrel calorimeter," *Nucl. Instrum. Meth.* **A309** (1991) 77–100.

ZEUS Calorimeter Group Collaboration, A. Andresen *et al.*, "Construction and beam test of the ZEUS forward and rear calorimeter," *Nucl. Instrum. Meth.* **A309** (1991) 101–142.

A. Caldwell *et al.*, "Design and implementation of a high precision readout system for the ZEUS calorimeter," *Nucl. Instrum. Meth.* **A321** (1992) 356–364.

ZEUS Barrel Calorimeter Group Collaboration, A. Bernstein *et al.*, "Beam tests of the ZEUS barrel calorimeter," *Nucl. Instrum. Meth.* **A336** (1993) 23–52.

[39] **ZEUS** Collaboration, R. Carlin, W. H. Smith, K. Tokushuku, and L. W. Wiggers, "The trigger of ZEUS, a flexible system for a high bunch crossing rate collider," *Nucl. Instrum. Meth.* **A379** (1996) 542–544.

G. P. Heath *et al.*, "The ZEUS first level tracking trigger," *Nucl. Instrum. Meth.* **A315** (1992) 431–435.

[40] S. M. Fisher and P. Palazzi, "ADAMO Reference Manual for Version 3.3,". CERN-ECP, available on `http://adamo.web.cern.ch/Adamo/refmanual/Document.html`.

[41] D. Kisielewska *et al.*, "FAST LUMINOSITY MONITORING AT HERA," *Nukleonika* **31** (1986) 205–238.

ZEUS Luminosity Group Collaboration, J. Andruszkow *et al.*, "Luminosity measurement in the ZEUS experiment," *Acta Phys. Polon.* **B32** (2001) 2025–2058.

ZEUS Luminosity Monitor Group Collaboration, J. Andruszkow *et al.*, "First measurement of HERA luminosity by ZEUS lumi monitor,". DESY-92-066.

[42] M. Helbich *et al.*, "The spectrometer system for measuring ZEUS luminosity at HERA," *Nucl. Instrum. Meth.* **A565** (2006) 572–588, `physics/0512153`.

[43] **ZEUS** Collaboration, S. Chekanov *et al.*, "Measurement of charged current deep inelastic scattering cross sections with a longitudinally polarised electron beam at HERA," `0812.4620`.

[44] V. Roberfroid, "Improvement of the Kalman filter fit of the ZEUS experiment," `physics/0701271`. ZEUS Note 06-010.

[45] R. E. Kalman, "A New Approach to Linear Filtering and Prediction Problems," *Trans. ASME, J. Basic Engineering* **82** (1960) 35–45.

[46] A. Spiridonov, "Mathematical Framework for Fast and Rigorous Track Fit for the ZEUS Detector," `0812.1245`. ZEUS Note 08-003.

[47] S. Catani, Y. L. Dokshitzer, and B. R. Webber, "The K-perpendicular clustering algorithm for jets in deep inelastic scattering and hadron collisions," *Phys. Lett.* **B285** (1992) 291–299.

S. Catani, Y. L. Dokshitzer, M. H. Seymour, and B. R. Webber, "Longitudinally invariant K(t) clustering algorithms for hadron hadron collisions," *Nucl. Phys.* **B406** (1993) 187–224.

[48] B. Straub, "The EM Electron Finder,". available on `http://www-zeus.desy.de/~straub/ZEUS_ONLY/doc/em.ps`.

[49] A. Lopez-Duran Viani and S. Schlenstedt, "Electron finder efficiencies and impurities. A comparison between SINISTRA95, EM and EMNET." ZEUS-99-077, internal ZEUS note, 1999.

[50] U. Amaldi *et al.*, "REPORT FROM THE STUDY GROUP ON DETECTORS FOR CHARGED CURRENT EVENTS,". In *Hamburg 1979, Proceedings, Study Of An E P Facility For Europe*, Hamburg 1979, 377-414.

S. Bentvelsen, J. Engelen, and P. Kooijman, "Reconstruction of (x, Q**2) and extraction of structure functions in neutral current scattering at HERA,". NIKHEF-H-92-02.

[51] M. Milite, "The internal structure of charmed jets in photoproduction at HERA and tests of the ZEUS microvertex silicon sensors,". DESY-THESIS-2001-050.

[52] **ZEUS MVD Group** Collaboration, V. Chiochia, "The ZEUS micro vertex detector," *Nucl. Instrum. Meth.* **A501** (2003) 60–64, `hep-ex/0111061`.

V. Chiochia, "Measurement of beauty quark production in deep inelastic scattering at HERA,". DESY-THESIS-2003-031.

[53] S. Shimizu, *Performance study of the ZEUS silicon microvertex detector.* PhD thesis, Master Thesis, KEK, 2006.

[54] G. Hartner internal ZEUS note, in preparation.

[55] G. Bashindzhagyan and N. Korotkova, "Simulation of silicon microstrip detector resolution for ZEUS vertex upgrade." ZEUS-99-023, internal ZEUS note, 1999.

[56] R. Brun and F. Rademakers, "ROOT: An object oriented data analysis framework," *Nucl. Instrum. Meth.* **A389** (1997) 81–86.

[57] L. Lonnblad, "ARIADNE version 4: A Program for simulation of QCD cascades implementing the color dipole model," *Comput. Phys. Commun.* **71** (1992) 15–31.

[58] G. Ingelman, A. Edin, and J. Rathsman, "LEPTO 6.5 - A Monte Carlo Generator for Deep Inelastic Lepton-Nucleon Scattering," *Comput. Phys. Commun.* **101** (1997) 108–134, hep-ph/9605286.

[59] G. Altarelli and G. Parisi, "Asymptotic Freedom in Parton Language," *Nucl. Phys.* **B126** (1977) 298.

[60] V. N. Gribov and L. N. Lipatov, "Deep inelastic e p scattering in perturbation theory," *Sov. J. Nucl. Phys.* **15** (1972) 438–450.

Y. L. Dokshitzer, "Calculation of the Structure Functions for Deep Inelastic Scattering and e+ e- Annihilation by Perturbation Theory in Quantum Chromodynamics. (In Russian)," *Sov. Phys. JETP* **46** (1977) 641–653.

[61] T. Sjostrand, "The Lund Monte Carlo for Jet Fragmentation and e+ e- Physics: Jetset Version 6.2," *Comput. Phys. Commun.* **39** (1986) 347–407.

T. Sjostrand and M. Bengtsson, "The Lund Monte Carlo for Jet Fragmentation and e+ e- Physics. Jetset Version 6.3: An Update," *Comput. Phys. Commun.* **43** (1987) 367.

[62] H.-U. Bengtsson and T. Sjostrand, "The Lund Monte Carlo for Hadronic Processes: Pythia Version 4.8," *Comput. Phys. Commun.* **46** (1987) 43.

[63] G. Marchesini *et al.*, "HERWIG: A Monte Carlo event generator for simulating hadron emission reactions with interfering gluons. Version 5.1 - April 1991," *Comput. Phys. Commun.* **67** (1992) 465–508.

G. Corcella *et al.*, "HERWIG 6.5: an event generator for Hadron Emission Reactions With Interfering Gluons (including supersymmetric processes)," *JHEP* **01** (2001) 010, hep-ph/0011363.

[64] D. Amati and G. Veneziano, "Preconfinement as a Property of Perturbative QCD," *Phys. Lett.* **B83** (1979) 87.

[65] K. Charchula, G. A. Schuler, and H. Spiesberger, "Combined QED and QCD radiative effects in deep inelastic lepton - proton scattering: The Monte Carlo generator DJANGO6," *Comput. Phys. Commun.* **81** (1994) 381–402.

[66] A. Kwiatkowski, H. Spiesberger, and H. J. Mohring, "HERACLES: AN EVENT GENERATOR FOR e p INTERACTIONS AT HERA ENERGIES INCLUDING RADIATIVE PROCESSES: VERSION 1.0," *Comp. Phys. Commun.* **69** (1992) 155–172.

[67] **CTEQ** Collaboration, H. L. Lai *et al.*, "Global QCD analysis of parton structure of the nucleon: CTEQ5 parton distributions," *Eur. Phys. J.* **C12** (2000) 375–392, hep-ph/9903282.

[68] S. Katsanevas and P. Morawitz, "SUSYGEN-2.2: A Monte Carlo event generator for MSSM sparticle production at e+ e- colliders," *Comput. Phys. Commun.* **112** (1998) 227–269, hep-ph/9711417.

E. Perez, "Extension of the SUSYGEN package to supersymmetry at e p colliders,". Prepared for Workshop on Monte Carlo Generators for HERA Physics (Plenary Starting Meeting), Hamburg, Germany, 27-30 Apr 1998.

N. Ghodbane, "SUSYGEN3: An event generator for linear colliders," hep-ph/9909499.

[69] A. Djouadi, J.-L. Kneur, and G. Moultaka, "SuSpect: A Fortran code for the supersymmetric and Higgs particle spectrum in the MSSM," *Comput. Phys. Commun.* **176** (2007) 426–455, hep-ph/0211331.

[70] C. Berger and W. Wagner, "Photon-Photon Reactions," *Phys. Rept.* **146** (1987) 1.

[71] A. Pukhov, "CalcHEP 3.2: MSSM, structure functions, event generation, batchs, and generation of matrix elements for other packages," hep-ph/0412191.

[72] R. Brun, F. Bruyant, M. Maire, A. C. McPherson, and P. Zanarini, "GEANT3,". CERN-DD/EE/84-1.

[73] K. Kaschube, "Search for Gravitino Production in R-Parity Violating Supersymmetry at HERA,". Diplomarbeit 2007 (unpublished).

[74] J. F. Grivaz, "Supersymmetry, Part II (Experiment)," *Phys. Lett.* **B667** (2008) 1228–1237.

J. L. Feng, J.-F. Grivaz, and J. Nachtman, "Searches for Supersymmetry at High-Energy Colliders," 0903.0046.

[75] **L3** Collaboration, P. Achard *et al.*, "Search for scalar leptons and scalar quarks at LEP," *Phys. Lett.* **B580** (2004) 37–49, hep-ex/0310007.

[76] LEPSUSYWG, ALEPH, DELPHI, L3 and OPAL experiments, note LEPSUSYWG/04-07.1, http://lepsusy.web.cern.ch/lepsusy/Welcome.html.

[77] **ALEPH** Collaboration, A. Heister *et al.*, "Search for gauge mediated SUSY breaking topologies in e^+e^- collisions at center-of-mass energies up to 209-GeV," *Eur. Phys. J.* **C25** (2002) 339–351, hep-ex/0203024.

OPAL Collaboration, G. Abbiendi *et al.*, "Searches for gauge-mediated supersymmetry breaking topologies in e+ e- collisions at LEP2," *Eur. Phys. J.* **C46** (2006) 307–341, hep-ex/0507048.

[78] LEPSUSYWG, ALEPH, DELPHI, L3 and OPAL experiments, note LEPSUSYWG/04-09.1, http://lepsusy.web.cern.ch/lepsusy/Welcome.html.

[79] **CDF** Collaboration, D. E. Acosta *et al.*, "Limits on extra dimensions and new particle production in the exclusive photon and missing energy signature in $p\bar{p}$ collisions at $\sqrt{s} = 1.8$ TeV," *Phys. Rev. Lett.* **89** (2002) 281801, hep-ex/0205057.

[80] **D0** Collaboration, V. M. Abazov *et al.*, "Search for supersymmetry in di-photon final states at $\sqrt{s} = 1.96$-TeV," *Phys. Lett.* **B659** (2008) 856–863, 0710.3946.

[81] B. C. Allanach *et al.*, "The Snowmass points and slopes: Benchmarks for SUSY searches," *Eur. Phys. J.* **C25** (2002) 113–123, hep-ph/0202233.

[82] **H1** Collaboration, A. Aktas *et al.*, "Search for light gravitinos in events with photons and missing transverse momentum at HERA," *Phys. Lett.* **B616** (2005) 31–42, hep-ex/0501030.

[83] A. Hocker *et al.*, "TMVA: Toolkit for multivariate data analysis," *PoS* **ACAT** (2007) 040, physics/0703039.

[84] T. Carli and B. Koblitz, "A multi-variate discrimination technique based on range- searching," *Nucl. Instrum. Meth.* **A501** (2003) 576–588, hep-ex/0211019.

[85] R. Sedgewick, *Algorithms in C++*, ch. 26. Addison-Wesley, 1992.

[86] T. Junk, "Confidence Level Computation for Combining Searches with Small Statistics," *Nucl. Instrum. Meth.* **A434** (1999) 435–443, hep-ex/9902006.

[87] A. L. Read, "Presentation of search results: The CL(s) technique," *J. Phys.* **G28** (2002) 2693–2704.

[88] **ZEUS** Collaboration, S. Chekanov *et al.*, "Measurement of high-Q**2 charged current cross sections in e- p deep inelastic scattering at HERA," *Phys. Lett.* **B539** (2002) 197–217, hep-ex/0205091.

[89] **H1 and ZEUS** Collaboration, D. M. South, "Isolated leptons and missing P(T) at HERA," *J. Phys. Conf. Ser.* **110** (2008) 072041, 0709.4433.

ZEUS Collaboration, J. Ferrando, "HERA signature-based searches I: events with isolated leptons and missing transverse momentum at HERA," 0807.4048.

[90] **H1** Collaboration, F. D. Aaron *et al.*, "A General Search for New Phenomena at HERA," *Phys. Lett.* **B674** (2009) 257–268, 0901.0507.

[91] see http://www.linearcollider.org/cms/.

[92] J. Brau, Y. Okada, and N. Walker, "Ilc reference design report volume 1 - executive summary," 2007.

[93] I. Wilson, "The compact linear collider CLIC," *Phys. Rept.* **403-404** (2004) 365–378.

see http://clic-study.web.cern.ch/CLIC-Study/.

Acknowledgement

I would like to thank

- Prof. Peter Schleper for the opportunity to work on this topic, for his advice and his inspiring enthusiasm,
- Prof. Robert Klanner for helpful insights, nasty questions, general support and the kind-hearted atmosphere in his group,
- Prof. Johannes Haller for being a referee for this dissertation,
- Jolanta Sztuk-Dambietz for advice and help on many technical and physical aspects of the analysis, as well as for sharing both the fun and frustration in teaching exercises for physics students,
- Claus Horn for daily guidance at the start of my PhD and for having written such a thorough and pedagogical thesis,
- Kolja Kaschube for successful team work and helpful discussions,
- Antje Hüttmann for sharing knowledge, code, and the bright and the bitter moments of our PhD time,
- the other (ex-)members of the Hamburg University ZEUS group, especially Alessio Bonato, Friederike Januschek, Hanno Perrey, Jörg Behr, Monica Turcato, Thomas Schörner-Sadenius and Thorben Theedt,
- the coordinators and members of the High-Q^2 group, most notably Amita Raval, Iris Abt, James Ferrando, Junpei Maeda and Robert Ciesielski,
- Rainer Mankel and Tobias Haas for suggesting the interesting technical topic, and for many discussions and hints,
- Shima Shimizu for providing code as a starting point for my clustering studies,
- Vincenzo Chiochia for helpful explanations of the η algorithm,
- Hartmut Stadie for his big help creating an efficient framework for the clustering studies and implementing the result, for teaching me a lot about programming and problem solving, and for proofreading part of this thesis,
- the other members of the ZEUS tracking developers group, especially Alexander Spiridonov, Gerd Hartner, Monica Turcato and Silvia Miglioranzi,
- Christian Autermann for proofreading my thesis and making valuable comments,

- Jens Koesling for providing a view from the theoretical side of physics, and for being a supportive and constantly inspiring friend,
- Matthias Merk for being always there (also when he is far away), and for his deep, unconditional friendship,
- Cornelia and Heino Cordes for backing my little family when I was not around,
- my parents, my brother and my sister for support and enduring my lack of time,
- and most of all my wonderful wife Jasmyn and our marvellous little boy Jonathan for love and patience. I know how much you both had to tolerate in the last years. Yet another reason to love you even more.

Index